

INVESTIGATION OF THE SINTERING FUNDAMENTALS OF MAGNESIUM  
POWDERS

by

Paul Burke

Submitted in partial fulfilment of the requirements  
for the degree of Doctor of Philosophy

at

Dalhousie University

Halifax, Nova Scotia

January 2011

© Copyright by Paul Burke, 2011

DALHOUSIE UNIVERSITY

DEPARTMENT OF PROCESS ENGINEERING AND APPLIED SCIENCE

The undersigned hereby certify that they have read and recommend to the Faculty of Graduate Studies for acceptance a thesis entitled “Investigation of the Sintering Fundamentals of Magnesium Powders” by Paul Burke in partial fulfillment of the requirements for the degree of Doctor of Philosophy.

Dated: January 28, 2011

External Examiner: \_\_\_\_\_

Research Supervisor: \_\_\_\_\_

Examining Committee: \_\_\_\_\_

\_\_\_\_\_

Departmental Representative: \_\_\_\_\_

DALHOUSIE UNIVERSITY

DATE: January 28, 2011

AUTHOR: Paul Burke

TITLE: Investigation of the Sintering Fundamentals of Magnesium Powders

DEPARTMENT OR SCHOOL: Department of Process Engineering and Applied  
Science

DEGREE: PhD CONVOCATION: October YEAR: 2011

Permission is herewith granted to Dalhousie University to circulate and to have copied for non-commercial purposes, at its discretion, the above title upon the request of individuals or institutions. I understand that my thesis will be electronically available to the public.

The author reserves other publication rights, and neither the thesis nor extensive extracts from it may be printed or otherwise reproduced without the author's written permission.

The author attests that permission has been obtained for the use of any copyrighted material appearing in the thesis (other than the brief excerpts requiring only proper acknowledgement in scholarly writing), and that all such use is clearly acknowledged.

---

Signature of Author

# TABLE OF CONTENTS

<b>LIST OF FIGURES</b>	<b>ix</b>
<b>LIST OF TABLES</b>	<b>xv</b>
<b>ABSTRACT</b>	<b>xvii</b>
<b>LIST OF ABBREVIATIONS AND SYMBOLS</b>	<b>xviii</b>
<b>ACKNOWLEDGEMENTS</b>	<b>xx</b>
<b>CHAPTER 1 INTRODUCTION</b>	<b>1</b>
<b>1.1 Magnesium and Magnesium Alloys</b>	<b>1</b>
1.1.1 History	1
1.1.2 Properties and Advantages	1
1.1.3 Ores and Occurrence	2
1.1.4 Production	3
1.1.4.1 Electrolytic	3
1.1.4.1.1 Dow Chemical Process	3
1.1.4.1.2 Norsk Hydro Process	4
1.1.4.1.3 IG Faben Process	5
1.1.4.2 Metallothermic	5
1.1.4.2.1 Pidgeon Process	6
1.1.4.2.2 Magnetherm Process	6
1.1.5 Wrought and Cast Alloys	7
<b>1.2 Alloying</b>	<b>8</b>
1.2.1 Phase Diagrams	8

1.2.1.1	Powder Production	9
1.2.1.2	Sintering	9
1.2.2	Phase Diagrams of Interest for Mg P/M	10
1.2.3	Alloying Theory	18
1.2.3.1	P/M Alloying Theory	19
<b>1.3</b>	<b>Sintering</b>	<b>21</b>
1.3.1	Solid State Sintering	21
1.3.2	Liquid Phase Sintering	26
1.3.3	Sintering Atmosphere	30
1.3.4	Surface Layer	31
1.3.5	Vacancy Generating Processes	35
1.3.6	Super-Solidus Liquid Phase Sintering	38
<b>1.4</b>	<b>Analytic Techniques for Surface Layer Characterization</b>	<b>40</b>
1.4.1	Surface Spectroscopy	40
1.4.1.1	Transmission Electron Microscope (TEM)	40
1.4.1.1.1	TEM Sample Preparation	41
1.4.1.2	X-ray Photoelectron Spectroscopy (XPS)	42
1.4.1.3	Auger Electron Spectroscopy (AES)	44
1.4.1.4	Secondary Ion Mass Spectroscopy (SIMS)	46
1.4.2	Thermal Analysis	47
1.4.2.1	Dilatometry	47
1.4.2.2	Differential Scanning Calorimetry (DSC)	48
1.4.2.3	Differential Thermal Analysis (DTA)	48
1.4.2.4	Thermogravimetric Analysis (TGA)	48
<b>1.5</b>	<b>Forming and Shaping</b>	<b>49</b>
1.5.1	Hot Work of Magnesium	51
1.5.1.1	Deformation Mechanisms	51

1.5.1.2	Grain Size Effects	52
1.5.2	Industrial Practices for Wrought Alloys	53
<b>1.6</b>	<b>Thermodynamic Calculations</b>	<b>55</b>
1.6.1	Reactions Between Magnesium and the Atmosphere	55
1.6.2	Decomposition of Components of the Surface Layer Formed on Magnesium	56
<b>1.7</b>	<b>Previous Research of Magnesium P/M</b>	<b>56</b>
<b>1.8</b>	<b>Research Objectives</b>	<b>61</b>
<b>CHAPTER 2</b>	<b>EXPERIMENTAL PROCEDURES</b>	<b>62</b>
<b>2.1</b>	<b>Materials</b>	<b>62</b>
<b>2.2</b>	<b>Powder Characterization</b>	<b>62</b>
<b>2.3</b>	<b>Powder Blending</b>	<b>63</b>
<b>2.4</b>	<b>Uni-Axial Die Compaction (UDC)</b>	<b>63</b>
<b>2.5</b>	<b>Cold Isostatic Pressing (CIP)</b>	<b>65</b>
<b>2.6</b>	<b>Sintering</b>	<b>65</b>
<b>2.7</b>	<b>Cold and Hot Working</b>	<b>67</b>
<b>2.8</b>	<b>Dimensional Change</b>	<b>67</b>
<b>2.9</b>	<b>Density Testing</b>	<b>68</b>
<b>2.10</b>	<b>Hardness Testing</b>	<b>69</b>
<b>2.11</b>	<b>Tensile Testing</b>	<b>69</b>
<b>2.12</b>	<b>Microstructure Evaluation and Surface Layer Characterization</b>	<b>70</b>
2.12.1	Optical Microscopy (OM)	70
2.12.2	Scanning Electron Microscopy (SEM)	70
2.12.3	Energy Dispersive Spectroscopy (EDS)	70

2.12.4	Transmission Electron Microscopy (TEM)	71
2.12.5	Focused Ion Beam (FIB) System	71
2.12.6	X-ray Photoelectron Spectroscopy (XPS)	71
2.12.7	Differential Scanning Calorimetry (DSC)	73
<b>CHAPTER 3 RESULTS AND DISCUSSION</b>		<b>74</b>
<b>3.1</b>	<b>Fundamental Sintering Studies</b>	<b>74</b>
3.1.1	FACTSage Calculations	74
3.1.2	Metallothermic Reduction of Magnesium Oxide	75
3.1.3	Differential Scanning Calorimetry (DSC)	76
3.1.3.1	Pure Magnesium	77
3.1.3.2	Magnesium + 1wt% Calcium	79
3.1.3.3	Magnesium + 2wt% Yttrium	82
3.1.4	Surface Layer Characterization	84
3.1.4.1	X-ray Photoelectron Spectroscopy (XPS)	84
3.1.4.1.1	Green (Unsintered) Magnesium	84
3.1.4.1.2	Sintered Magnesium	87
3.1.4.1.3	Comparison of Green and Sintered Samples	91
3.1.4.2	Scanning Electron Microscopy (SEM)	96
3.1.4.3	Focused Ion Beam (FIB)	99
3.1.4.4	Transmission Electron Microscopy (TEM)	101
<b>3.2</b>	<b>Practical Sintering Strategies</b>	<b>104</b>
3.2.1	Ground vs. Atomized Magnesium Powder	104
3.2.1.1	Uniaxially Pressed Ground Magnesium Powder	104
3.2.1.2	Cold Isostatically Pressed (CIP) Ground Magnesium Powder	112
3.2.1.3	Cold Isostatically Pressed (CIP) Atomized Magnesium Powder	116
3.2.1.4	Uniaxially Pressed Atomized Magnesium Powder	119

3.2.2	Extended Sintering Time	119
3.2.3	Alloying Additions	122
3.2.3.1	Strengthening	122
3.2.3.1.1	Aluminum and Zinc	122
3.2.3.2	Liquid Forming	123
3.2.3.2.1	Tin	123
3.2.3.3	Surface Layer Disrupting	125
3.2.3.3.1	Calcium	125
3.2.3.3.2	Yttrium	133
3.2.4	Sintering Atmosphere	135
3.2.5	Cold and Hot Working	137
<b>CHAPTER 4 CONCLUSIONS</b>		<b>140</b>
4.1	<b>Contribution to Original Thought</b>	<b>143</b>
4.2	<b>Recommendations for Future Work</b>	<b>144</b>
<b>REFERENCES</b>		<b>146</b>
<b>APPENDIX 1</b>		<b>150</b>

## LIST OF FIGURES

Figure 1.1 - The electrolytic cell used by Dow Chemical. [2]	4
Figure 1.2 - The electrolytic cell used by Norsk Hydro. [2]	5
Figure 1.3 - Electrolytic cell used in the IG Faben process. [2]	5
Figure 1.4 - The reactor used in the Magnetherm process. [2]	7
Figure 1.5 - Aluminum - magnesium binary phase diagram. [1]	11
Figure 1.6 – Calcium - magnesium binary phase diagram. [1]	13
Figure 1.7 - Lithium - magnesium binary phase diagram. [1]	14
Figure 1.8 - Tin - magnesium binary phase diagram. [1]	15
Figure 1.9 - Yttrium - magnesium binary phase diagram. [1]	16
Figure 1.10 - Zinc - magnesium binary phase diagram. [1]	17
Figure 1.11 - Aluminum - zinc - magnesium ternary phase diagram. [1]	18
Figure 1.12 - Computer model of solid state sintering. [4]	22
Figure 1.13 - Evaporation and condensation surface transport.	23
Figure 1.14 - Surface transport by surface diffusion.	23
Figure 1.15 - Atom transport by volume diffusion.	24
Figure 1.16 - Bulk transport through grain boundary diffusion.	24
Figure 1.17 - Bulk transport by means of plastic flow.	25
Figure 1.18 - Four stages of sintering. [3]	25
Figure 1.19 - Densification through Ostwald ripening.	26
Figure 1.20 - Computer model of liquid phase sintering. [5]	27
Figure 1.21 - Liquid wetting a solid surface.	29
Figure 1.22 - Force of compaction creates cracks in surface layer.	34

Figure 1.23 - Schematic representation of a pore filling as vacancies are generated. [9]	38
Figure 1.24 - TEM micrograph showing the oxide layer on niobium. [11]	41
Figure 1.25 - Diagram of FIB system.	42
Figure 1.26 - Diagram outlining the principles of XPS [10].	43
Figure 1.27 - A typical XPS result, showing the intensity response to varying thicknesses of Si wafers. [10]	44
Figure 1.28 - Diagram outlining the principles of AES [10].	45
Figure 1.29 - AES depth profiling of an oxide layer on Al. [10]	45
Figure 1.30 - Principles of SIMS operation, where 1. Cesium ion source, 2. Duoplasmatron, 3. Electrostatic lens, 4. Sample, 5. Ion energy analyzer, 6. Mass analyzer, 7. Electron multiplier, 8. Ion image detector [10].	46
Figure 1.31 - SIMS result of a depth profile on an oxide layer. [10]	47
Figure 1.32 - Schematic diagram of hot rolling, showing the effect on grain structure. [13]	50
Figure 1.33 - Schematic diagram of hot extrusion, showing effect on grain structure. [13]	50
Figure 1.34 - Atomic locations in hexagonal closed packed crystal structure. [1]	51
Figure 1.35 - Yield stress as a function of grain size, AZ91 Mg alloy and H321 Al alloy. [13]	53
Figure 1.36 - Deep drawing behaviour of Mg alloys. [13]	54
Figure 2.1 - Satec Systems Instron uni-axial press.	64
Figure 2.2 - Lindberg tube furnace.	66
Figure 2.3 - Typical temperature profile of sintering experiment.	67
Figure 2.4 - Dimensions of compacted bars.	68

Fig. 2.5 - Geometry of samples during etching. Grey represents the pure magnesium at the particles core, and black represents the surface layer. The un-etched sample is shown in a), an intermediate stage of etching in b), and the final stage in c). Proportions are exaggerated for clarity.	73
Figure 3.1 - Free energy - temperature diagram showing metals that may reduce MgO.	76
Figure 3.2 - DSC trace of two empty gold plated crucibles. Area (A) represents reactions between crucible and Au.	77
Figure 3.3 - DSC trace of pure magnesium powder heated from ambient to 600°C at 10°C/min. Area (A) represents hydroxide decomposition, area (B) hydrated carbonate decomposition. Area (C) is carbonate decomposition and (D) is formation of Mg <sub>3</sub> N <sub>2</sub> .	78
Figure 3.4 - Mass change of pure magnesium sample while heating to 600°C. Maximum mass was 223 mg at 600°C.	79
Figure 3.5 - DSC trace of magnesium with 1wt% calcium heated from ambient to 600 °C at 10 °C/min. Area (A) represents hydroxide decomposition, area (B) hydrated carbonate decomposition. Area (C) is the carbonate decomposition and area (D) is formation of of Mg <sub>3</sub> N <sub>2</sub> .	81
Figure 3.6 - Mass change of Mg-1Ca sample while heating to 600°C. Maximum mass was 217 mg at 600°C.	81
Figure 3.7 - DSC trace of magnesium with 2wt% yttrium heated from ambient to 600°C at 10°C/min. Area (A) represents hydroxide decomposition, area (B) hydrated carbonate decomposition. Area (C) is the formation of YN.	83
Figure 3.8 - Mass change of Mg-2Y sample while heating to 600°C. Maximum mass was 226 mg at 600°C.	83
Figure 3.9 - The XPS spectra of O 1s peak of Mg green sample : (a) etching, (b) high resolution	84
Figure 3.10 - The XPS spectra of Mg 2p peak of Mg green sample : (a) etching, (b) high resolution	86
Figure 3.11 - The high resolution spectra of C 1s peak of sample Mg green after etching.	87
Figure 3.12 - The XPS spectra of O 1s peak of the Mg-sintered sample as a function of etching: (a) both peaks are getting bigger (b)subsequent continuation of etching showing decrease on higher binding energy peak.	88

Figure 3.13 - The high resolution spectra of O 1s peak of sample Mg sintered.	89
Figure 3.14 - (a) The XPS spectra of Mg 2p peak of the Mg-sintered sample as a function of etching, (b) subsequent continuation of the etching.	90
Figure 3.15 - The high resolution spectrum of Mg 2p peak of sintered Mg.	91
Figure 3.16 - O 1s peak comparison of Mg green and Mg sintered samples after etching.	92
Figure 3.17 - Comparison of Mg 2p peaks of Mg green and Mg-sintered samples after etching.	93
Figure 3.18 - Comparison of survey spectra of Mg green and Mg sintered samples after etching.	95
Figure 3.19 - SEM image and EDS spectra taken from Mg-1%Ca sample.	97
Figure 3.20 - Secondary electron SEM image and corresponding EDS maps showing distribution of Mg, O and Ca.	98
Fig. 3.21 - Focused ion beam image of the cross section of a single Mg powder particle. Note the surface layer (thin white layer) enveloping the Mg core.	99
Figure 3.22 – Mg with 1 wt% Ca. Surface layer has been protected with deposited tungsten. Light areas at grain boundaries are Ca rich.	100
Figure 3.23 - TEM micrograph of the as received Mg powder showing the surface layer formed on a single particle. The bulk of the powder particle is right of the layer, and the protective coatings to the left.	102
Figure 3.24 - Optical micrograph of as received ground pure magnesium powder, where the grey phase is magnesium and the black phase is the mounting material.	104
Figure 3.25 - Particle size distribution for ground magnesium powder categories 38-45 $\mu\text{m}$ and 45-53 $\mu\text{m}$ .	105
Figure 3.26 - Compaction curve of Uniaxially Die Compacted ground magnesium powder. Symbol size represents approximate error.	107
Figure 3.27 - Percent theoretical density of Uniaxially Die Compacted ground magnesium for green samples and samples sintered at 500 $^{\circ}\text{C}$ for 30 minutes.	107

Figure 3.28 - Hardness of sintered Uniaxially Die Compacted ground magnesium samples sintered at 500 °C for 30 minutes.	108
Figure 3.29 - Micrograph of Uniaxially Die Compacted green ground magnesium.	110
Figure 3.30 - Micrograph of Uniaxially Die Compacted ground magnesium sintered at 500°C for 30 minutes, with pore and area of interparticle bonding highlighted.	110
Figure 3.31 - Micrograph of Uniaxially Die Compacted ground magnesium sintered at 600 °C for 30 minutes, with pore and area of interparticle bonding (IPB) highlighted.	111
Figure 3.32 - Effect of sintering time at 600 °C on density of Uniaxially Die Compacted ground magnesium samples compacted at 500 MPa. Symbol size represents approximate error for hardness.	112
Figure 3.33 - Percent theoretical density of CIP ground magnesium samples as a function of powder size. Sintering was performed at 600 °C for 30 minutes.	113
Figure 3.34 - Hardness of sintered CIP ground magnesium samples as a function of powder size. Sintering was performed at 600 °C for 30 minutes.	114
Figure 3.35 - Effect of sintering time on Cold Isostatically Pressed ground magnesium samples on density and hardness. Sintering was performed at 600 °C. Symbol size represents approximate error for hardness.	115
Figure 3.36 - Effect of sintering temperature of Cold Isostatically Pressed ground magnesium samples on density and hardness. Sintering time was 30 minutes.	116
Figure 3.37 - SEM micrograph of as received atomized pure magnesium powder.	117
Figure 3.38 - Effect of sintering time on Cold Isostatically Pressed atomized magnesium samples on density and hardness. Sintering was performed at 600 °C.	118
Figure 3.39 - Optical microstructure of atomized UDC sample sintered at 600 °C for 40 minutes.	121
Figure 3.40 - Optical microstructure of atomized UDC sample sintered at 600 °C for 360 minutes.	121
Figure 3.41 - Pure Mg alloyed with 5% Sn. Compacted 500MPa, sintered 600°C for 40min.	124

- Figure 3.42 – An optical microscopy macrograph showing the eutectic liquid, equi-axed and rounded grain section of the sample. Calcium rich area at left. 126
- Figure 3.43 - An optical microscopy micrograph showing the eutectic liquid region. Dark areas are eutectic liquid, and light areas are Mg. 128
- Figure 3.44 - An optical microscopy micrograph of the boundary between the eutectic liquid and the equi-axed regions. Calcium rich area at left. 128
- Figure 3.45 - An optical microscopy micrograph of the transition area between equi-axed and rounded grain regions. Calcium rich area at left. 129
- Figure 3.46 – Comparison of the microstructure of (a) Mg-8Al and (b) Mg-8Al-2Y sintered in argon. Note the porosity present in (a) and (b), and the unreacted yttrium in (b). 135
- Figure 3.47 - Comparison of the microstructure of (a) Mg-8Al and (b) Mg-8Al-2Y sintered in nitrogen. Note the porosity present in both (a) and (b), and the frozen eutectic liquid in (b). 137

## LIST OF TABLES

Table 1.1 - Chemical composition of dolomite ores (wt%). [1]	2
Table 1.2 - Chemical composition of Mg bearing brines (wt%). [1]	3
Table 1.3 - Commercial magnesium alloy systems.	7
Table 1.4 - Diffusion rates of a metal through itself, and through its oxide. [8]	33
Table 1.5 - Comparison of surface spectroscopy techniques [10].	40
Table 3.1 - The binding energies of fitting peaks for O 1s peaks of sample Mg green and Mg sintered.	92
Table 3.2 - The binding energies for Mg 2p peaks of fitting peaks of sample Mg green and Mg sintered.	93
Table 3.3 - Thickness of surface layer formed on pure Mg particle due to exposure to atmosphere for various times.	101
Table 3.4 - Composition of the Mg surface layer on the as received powder shown in Figure 3.23. Spectrum 1 begins beyond the layer and 8 ends in the bulk of the particle.	103
Table 3.6 - Comparison of the properties of Uniaxially Die Compacted ground magnesium powders at various sintering temperatures.	109
Table 3.8 - Comparison of the properties of Uniaxially Die Compacted atomized magnesium powders compacted at 500 MPa and sintered at 600 °C for various sintering times.	120
Table 3.9 - Properties of Mg samples alloyed with Al and Zn. Compacted 500MPa, sintered 600°C for 40min.	123
Table 3.10 - Properties of Mg alloyed with 5% Sn. Compacted 500MPa, sintered 600°C for 40min.	124
Table 3.11 - Composition of regions of interest, determined by EDS. Reported as weight percent.	130
Table 3.12 – Apparent Hardness of regions of interest measured with Rockwell H scale. Negative values indicate a lower scale should be chosen, but results are included only to show reduced hardness in the rounded grain region.	132

Table 3.13 - Effect of 2 wt% Y addition on Mg-8Al alloy. Densities reported as % of theoretical.	134
Table 3.14 - Effect of sintering atmosphere on Mg-8Al alloy, and Mg-8Al-2Y alloy. Densities reported as % of theoretical.	136
Table 3.15 - Effect of hot work on Mg-8Al alloy sintered in Ar and N <sub>2</sub> , and with addition of 2 wt% Y. Sample Mg-8Al (N <sub>2</sub> ) proved too friable to roll, and cracked after a small amount of reduction. Densities reported as % of theoretical.	139
Table A.1 - Chemical composition of base powders, as reported by the manufacturer.	150
Table A.2 – Chemical composition of atomized pure magnesium powder.	151

## ABSTRACT

Magnesium and its alloys are attractive for use in automotive and aerospace applications because of their low density and good mechanical properties. However, difficulty in forming magnesium and the limited number of available commercial alloys limit their use. The present work describes the efforts to improve the attractiveness of magnesium through non-traditional processing, and presents results of current work on producing magnesium alloys via powder metallurgy (P/M). P/M can be used to alleviate the formability problem through near-net-shape processing, and also allows unique chemical compositions that can lead to new alloys with novel properties.

The surface layer formed on Mg powders during processing acts as a barrier to diffusion and sintering is problematic. X-ray photoelectron spectroscopy (XPS) was used to identify the composition of the layer, and it was found to contain oxides, hydroxides and carbonates of magnesium. A novel focused ion beam (FIB) process for obtaining thin films of Mg powder and sintered compacts was utilized to prepare samples for analysis with transmission electron microscopy (TEM). TEM observations and energy dispersive spectroscopy (EDS) measurements confirmed the presence of the compounds found in the surface layer by XPS, and allowed visual measurements of the thickness of the layer.

There are several means to possibly overcome the barrier formed by the surface layer. Sintering of pure magnesium compacts has been studied by differential scanning calorimetry (DSC), which identified several decomposition reactions during heating. The hydroxide and carbonate components of the layer decompose to MgO and gases below the sintering temperature. These reactions disrupt the layer and expose pure magnesium which allows for improved interparticle diffusion. It was found that alloying additions of calcium and yttrium promote surface layer disruption during sintering by DSC measurements and testing indicates improved mechanical properties. The use of a semi-inert sintering atmosphere allows the formation of compounds that promote densification, wetting and mobility of liquid phases. Experiments show that a semi-inert nitrogen atmosphere leads to improved properties over an inert argon atmosphere. Post-sintering processes such as hot working disrupt the layer and promote interparticle diffusion during recrystallization that improves density and mechanical properties.

## LIST OF ABBREVIATIONS AND SYMBOLS

BCC	Body centered cubic
CIP	Cold isostatic press
d	Diameter
DOE	Design of experiments
E	Modulus of elasticity
EDS	Energy dispersive spectrometer
FESEM	Field emission scanning electron microscope
FCC	Face centered cubic
H	Activation energy
HCP	Hexagonal close packed
HRH	Hardness Rockwell H
m	Mass
MIM	Metal injection molding
MMC	Metal matrix composite
OAL	Overall length
P	Pressure
P/M	Powder metallurgy
R	Radius
SEM	Scanning electron microscope
t	Time
TEM	Transmission electron microscope

W	Weight
W <sub>a</sub>	Work of adhesion
wt%	Weight percent
XRD	X-ray diffraction
$\varepsilon$	Strain
$\gamma$	Surface energy
$\eta$	Fractional porosity
$\mu$	Coefficient of friction
$\theta$	Dihedral angle
$\rho$	Density
$\sigma$	Stress

## **ACKNOWLEDGEMENTS**

I would like to acknowledge the financial support of the Natural Sciences and Engineering Research Council of Canada, as well as the Minerals Engineering Center and MATNET of Dalhousie University for the use of characterization equipment. Many thanks are due to my supervisory committee, Dr. Toru Okabe, Dr. Paul Bishop, Dr. William Caley and especially my supervisor Dr. Georges Kipouros for their helpful ideas and suggestions, and their continued guidance and support. I would like to thank Dr. Jian Li and Dr. Zeynel Bayindir, as some of this work could not have been completed if it had not been for their essential collaborations. I would also like to thank Dr. Kevin Plucknett for the use of equipment, and Patricia Scallion and Dean Grijm for assistance with equipment.

Thanks also goes to Mark Dellapinna, Adam Doyle, Eric Moreau, Yiannis Kipouros, Joel McCully, Damien Fancelli, Vianne Laverdiere, Guillaume Lamy, Chloe Petite, Vincent Vuaroqueaux, Mathew Leto, Sonia Yakoubi, Julien Roy and Florian Saint-Lebes for their helpful ideas and much appreciated assistance with lab work.

Finally, I would like to thank my wife Suzanne, and my boys Timothy and Jacob. Without their love and support I could not have made it this far.

# CHAPTER 1 INTRODUCTION

## 1.1 Magnesium and Magnesium Alloys

### 1.1.1 History

The elemental name is derived from city of Magnesia, Greece, where large deposits of magnesite were found. Magnesium was first discovered as an oxide in 1808 by Sir Humphrey Davy in England. The French scientist Antoine-Alexander Bussy was the first to isolate the pure metal in 1828. Electrolytic production of magnesium was first carried out by Michael Faraday in 1833. By the mid-nineteenth century commercial production in France, England and Germany was underway, although at a very small scale. The first metallothermic production of magnesium was accomplished by the Canadian researcher Dr. L.M. Pidgeon in 1941. [1]

### 1.1.2 Properties and Advantages

Magnesium is silvery white in colour, has an atomic number and a valiancy of 12 and 2, respectively. At all temperatures the crystal structure of magnesium is hexagonal close packed, and has a low density of  $1.738 \text{ g/cm}^3$ . The melting point of pure magnesium is  $650^\circ\text{C}$  and the boiling point is  $1090^\circ\text{C}$ . In the unalloyed form, magnesium has a tensile strength of 160 MPa and hardness 40 on the Brinnel scale [1].

Magnesium has the lowest density of all the structural metals, and also exhibits high damping capacity and high stiffness to weight ratio. Magnesium has a high

dimensional stability, and an extremely low heat content. Magnesium requires very little power for machining and can be easily joined by common methods. Parts consolidation and design simplification are possible because of these properties. Magnesium is also easily recycled.

### **1.1.3 Ores and Occurrence**

Magnesium is the 8th most common metal in nature, and composes 2.7% of the earth's crust. In nature, magnesium does not occur in metallic form, but as dolomite minerals and in low concentrations in some lake and seawater brines.

Table 1.1 and

Table 1.2 show the composition of dolomite ores and of brines containing magnesium.

The largest source of magnesium is seawater, from which ~6 million tons of magnesium can be produced from one cubic mile of seawater.

**Table 1.1 - Chemical composition of dolomite ores (wt%). [1]**

Deposit	MgO	CaO	Fe <sub>2</sub> O <sub>3</sub> +Al <sub>2</sub> O <sub>3</sub>	SiO <sub>2</sub>
Sorford, Norway	21.2	30.4	0.1	1.3
Tochigi, Japan	17.4	35.1	0.5	0.15
Addy, Washington	20-21.8	30-31.5		1.5
Marignac, France	19-20	32-34	0.3-0.5	0.2-0.4
Haley, Canada	21.3	30.7	0.1	0.15

**Table 1.2 - Chemical composition of Mg bearing brines (wt%). [1]**

Brine	Mg <sup>2+</sup>	Na <sup>+</sup>	Ca <sup>2+</sup>	Cl <sup>-</sup>	SO <sub>4</sub> <sup>2-</sup>
Great Salt Lake	1.1	7.6	0.02	14.1	2.0
Dead Sea	3.4	3.3	1.4	17.5	0.7
Seawater	0.13	1.08	0.04	1.94	0.27
Kali und Salz AG	8.5	0.2		25	0.24

### **1.1.4 Production**

#### **1.1.4.1 Electrolytic**

Electrolytic production of magnesium is based on the electrolysis of fused anhydrous MgCl<sub>2</sub>. MgCl<sub>2</sub> is recovered from magnesite, brine or seawater. The same basic principle is used in several different production methods.

##### *1.1.4.1.1 Dow Chemical Process*

In this process a feed of hydrous magnesium chloride (MgCl<sub>2</sub> • 6H<sub>2</sub>O) is evaporated and dried, and the feed is then added to the cell shown in Figure 1.1. The cell is a steel pot contained in a heating chamber, where mild steel cathode plates are placed close to the graphite anodes. The crucible is covered so the chlorine gas that is produced can be captured. The output is molten magnesium product, which floats to the top of the cell.

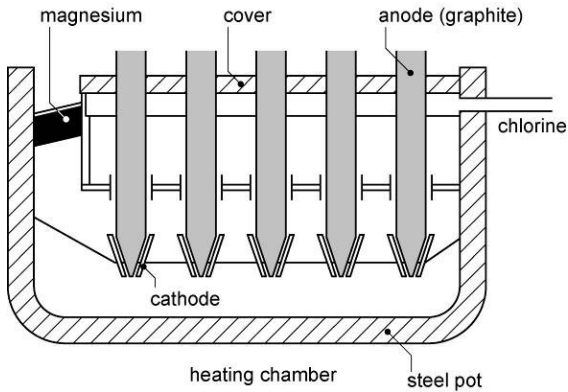


**Figure 1.1 - The electrolytic cell used by Dow Chemical. [2]**

#### 1.1.4.1.2 *Norsk Hydro Process*

The  $MgCl_2$  brine used in the Norsk Hydro process is produced from Potash (Europe) or magnesite (Quebec). The brine is completely dehydrated by heating in dry hydrochloric acid atmosphere. The feed then enters the cell shown in Figure 1.2. The cell is made of a refractory material, and the steel cathode surrounds the graphite anode. The crucible is covered to trap chlorine gas and the magnesium product floats to the top in a separate compartment.

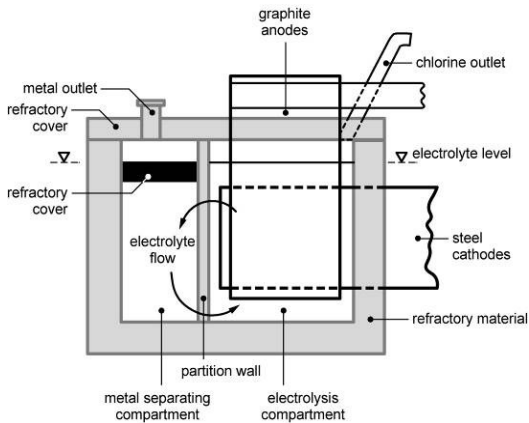


**Figure 1.2 - The electrolytic cell used by Norsk Hydro. [2]**

#### *1.1.4.1.3 IG Faben Process*

The magnesium produced in the Russian Federation and Israel starts from a carnallite ( $\text{MgCl}_2 \cdot \text{KCl} \cdot 6\text{H}_2\text{O}$ ) raw material, which is dehydrated and chlorinated to produce molten carnallite. The feed is then introduced into the cell shown in Figure 1.3. In the cell, the graphite anodes are adjacent to the steel cathodes, and the magnesium product floats to the surface of the cell.

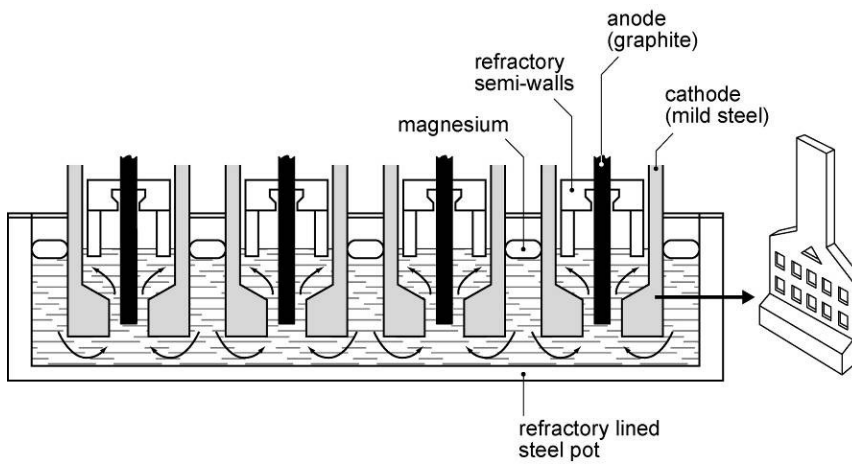


**Figure 1.3 - Electrolytic cell used in the IG Faben process. [2]**

#### *1.1.4.2 Metallothermic*

In metallothermic production of magnesium,  $\text{MgO}$  undergoes a thermal reduction by ferrosilicon. The  $\text{MgO}$  is derived from carbonate ores, usually dolomite. There are two main processes using this principle.

### 1.1.4.2.1 Pidgeon Process

In the Pidgeon process, a feed of dolomite ore is reduced with ferrosilicon in a batch operation under vacuum. The stainless steel reactor vessels are small externally heated retorts in which magnesium is produced as vapour, which condenses into crystals.

### 1.1.4.2.2 Magnetherm Process

In the Magnetherm process, dolomite, bauxite, magnesite and ferrosilicon are fed into an internally heated reactor. The feed can be added and slag removed without breaking vacuum. The reactor used is shown in Figure 1.4. The reactor is heated electrically as the starting ores and ferrosilicon are feed. Slag is tapped off at the bottom of the reactor and magnesium product condenses in a separate chamber.

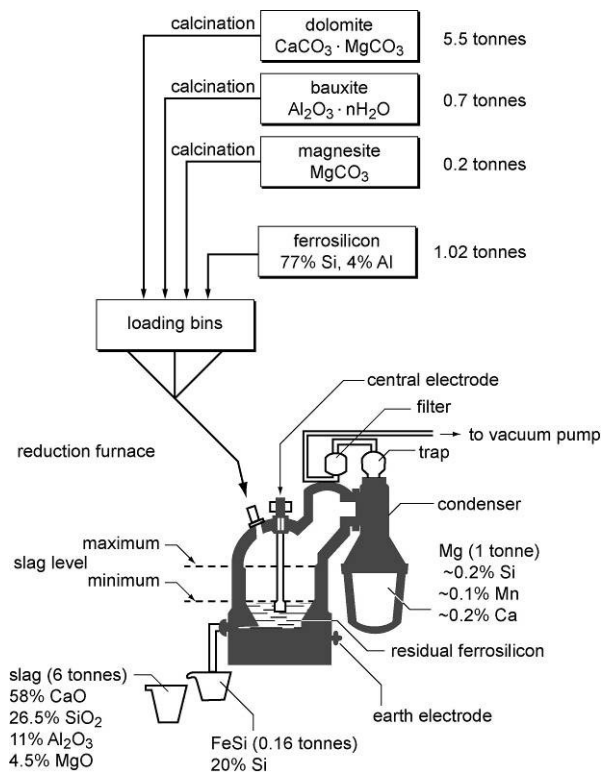


**Figure 1.4 - The reactor used in the Magnetherm process. [2]**

### ***1.1.5 Wrought and Cast Alloys***

Magnesium is rarely used unalloyed in engineering applications. Several alloying additions can be used to improve its properties. Table 1.3 shows the alloy systems which are commercially available. Currently, there is no international naming system for magnesium alloys. However, there is a trend toward the ASTM method of naming. An example of this naming system is given below.

ZM61-T5

Zirconium (6%)

Manganese (0.8%)

Cooled from an elevated temperature shaping process then artificially aged

**Table 1.3 - Commercial magnesium alloy systems.**

Magnesium-manganese
Magnesium-aluminum-manganese
Magnesium-aluminum-zinc-manganese
Magnesium-zirconium
Magnesium-zinc-zirconium
Magnesium-rare earth metal-zirconium
Magnesium-silver-rare earth metal-zirconium

## 1.2 Alloying

### 1.2.1 Phase Diagrams

An equilibrium phase diagram is a visual tool that shows the effect of temperature, composition, and pressure on two or more components at an equilibrium state. Typically, phase diagrams consist of temperature on the y axis and composition on the x axis at the pressure of 1 atm. Phase diagrams show the melting points of each pure component, and are used to identify the number of phases in a system and their solidus and liquidus temperatures, as well as the solubility of each component. Any intermetallic compounds that form are shown as either congruently or incongruently melting, and invariant points such as eutectics, eutectoids, peritectics are also shown.

Equilibrium phase diagrams of fixed pressure follow Gibbs phase rule, 1.1, where  $F$  is the degrees of freedom,  $C$  is the number of components and  $P$  is the number of phases present. At an invariant point in a phase diagram, the temperature and composition are fixed. Therefore the degree of freedom is zero. On any solidus or liquidus line, the degree of freedom is one, so either the temperature or composition may change. Inside a phase field, the degree of freedom is two, so both the temperature and composition may change.

$$F = C + 1 - P$$

1.1

### 1.2.1.1 Powder Production

In the field of powder metallurgy, phase diagrams may be used to design pre-alloyed powders. A pre-alloyed powder or master alloy is typically made by atomization of a liquid alloy, which is used to eliminate the use of a number of separate elemental powders that must be homogeneously blended. However, atomization may lead to a condition where the liquid alloy is solidified fast enough that non-equilibrium phases may be present. The high cooling rate of rapidly solidified powders allows extended solubilities than those which are shown on the equilibrium phase diagram of the system. This phenomenon has been exploited to produce powders that have an increased amount of a solid solution hardening alloying element, or to dissolve a larger amount of a precipitation hardening element, compared to the equilibrium prediction. Rapid solidification leads to alloys with novel properties that are unique to powder metallurgy processing.

### 1.2.1.2 Sintering

In ingot metallurgy, where the elements that make up the alloy begin in the liquid state and are considered well mixed, a cooling or heating path can be plotted on the phase diagram at the final composition of the alloy. This can be used to determine the phase transformations and microstructure as the alloy is cooled or heated. However, during sintering of a powder metallurgy compact, the temperature is lower than the melting temperature of the alloy, and it cannot be considered well mixed. The phase diagram can only be used to predict the composition if sintered for an infinitely long period and if

equilibrium is achieved. In practice, the mixture of two or more powders will have areas where the local composition may be of any composition on the phase diagram.

The local composition effect can be used to form eutectic liquids to aid sintering, even at total compositions far from the eutectic. The liquid may be transient however, and will eventually be absorbed into solid solution, if the sintering time is long enough. The reverse is also true, as alloying elements added for solid solution or precipitation hardening may form eutectic liquids that solidify at the grain boundaries if sintering time is not sufficiently long. The formation of intermetallic compounds is also highly probable. If the individual elements of the compound were added to serve another purpose, such as liquid formation, they will be trapped as an intermetallic and unable to perform their intended function.

### ***1.2.2 Phase Diagrams of Interest for Mg P/M***

The following alloy systems are of interest to research in magnesium powder metallurgy either as traditional additions to improve mechanical properties or corrosion resistance, or as powder metallurgy specific additions to form liquid phases or to disrupt surface layers on the magnesium base powder.

Figure 1.5 shows the binary phase diagram of aluminum and magnesium. Aluminum is a traditional alloying addition for wrought and cast magnesium alloys as it strengthens through solid solution with magnesium and also improves the corrosion

resistance. The phase diagram suggests that precipitation hardening is possible, but the precipitates are bulky and incoherent to the matrix, and little strengthening is realized. [1]

The Al – Mg phase diagram has two low melting temperature eutectics that will form transient liquid phases during sintering. However, the solubility of aluminum in magnesium is high, and the liquid is quickly absorbed into the matrix at high sintering temperatures or long sintering times. It is also possible that one of the bulky, incoherent intermetallics may form to the detriment of physical properties.

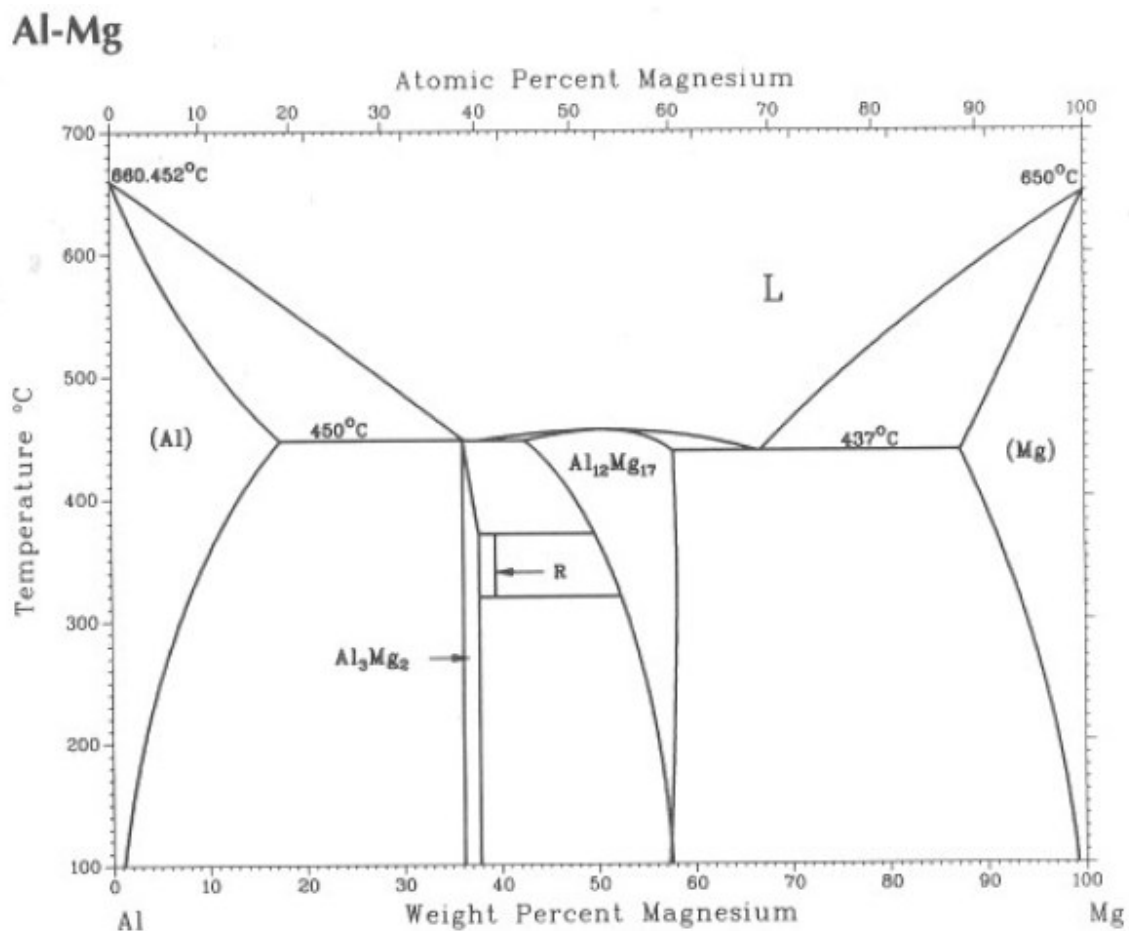
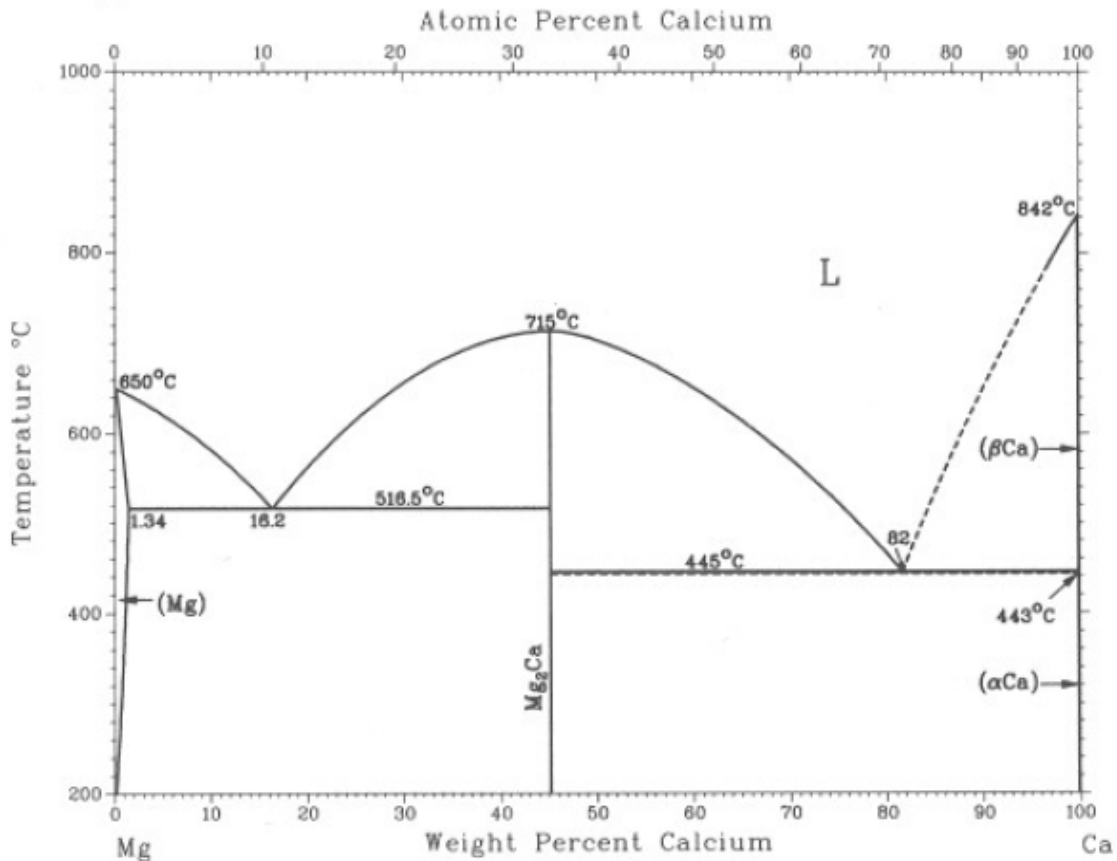


Figure 1.5 - Aluminum - magnesium binary phase diagram. [1]

Figure 1.6 shows the calcium and magnesium binary phase diagram. Calcium has been used in some wrought alloys to improve strength, and the intermetallic,  $Mg_2Ca$ , has a higher melting point than magnesium, which if precipitated, may increase high temperature strength. Calcium is of interest to magnesium P/M primarily because it is one of the few elements that has a higher affinity for oxygen, and has the ability to disrupt the surface layer on magnesium particles that interfere with sintering.

The low melting temperature eutectics allow liquid formation during sintering, which may help quickly draw calcium through the compact by capillary action to disrupt a larger area of magnesium surface layer. The low solubility of calcium in magnesium will impede the diffusion of calcium through magnesium particles however.

## Ca-Mg



**Figure 1.6 – Calcium - magnesium binary phase diagram. [1]**

Figure 1.7 is the binary phase diagram for lithium and magnesium. Lithium has been used in wrought alloys to transform the hexagonal crystal structure of magnesium to a cubic structure. An addition of 12 wt% or more lithium is required, and improved formability is realized without severely affecting the advantageous properties of magnesium.

In the case of powder metallurgy, lithium is of interest because it is the closest of all the elements to forming an ideal liquid phase with magnesium. Lithium has a low

melting point, magnesium is highly soluble in lithium for fast diffusion, and no intermetallic compounds are formed. However, the solubility of lithium in magnesium is relatively high, and will form a transient liquid phase in low concentrations.

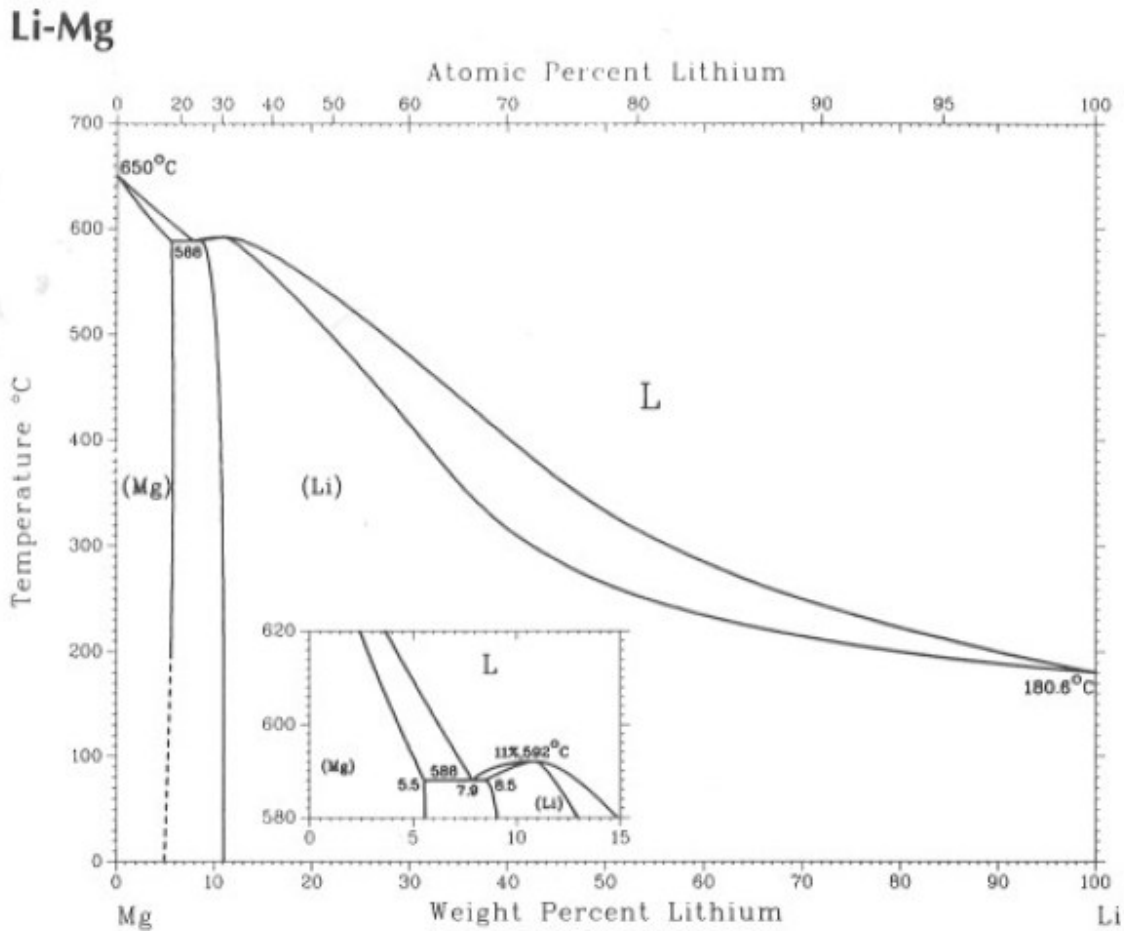


**Figure 1.7 - Lithium - magnesium binary phase diagram. [1]**

Figure 1.8 shows the binary phase diagram of magnesium and tin. Tin has been used as an alloying addition to wrought magnesium with the purpose of strengthening through solid solution and precipitation hardening. The intermetallic,  $Mg_2Sn$ , has the unique property of a higher melting point than either magnesium or tin, and high

temperature properties are improved. Tin is a possible liquid phase forming addition to magnesium P/M, but the only feature it shares with an ideal liquid phase is a low melting temperature.

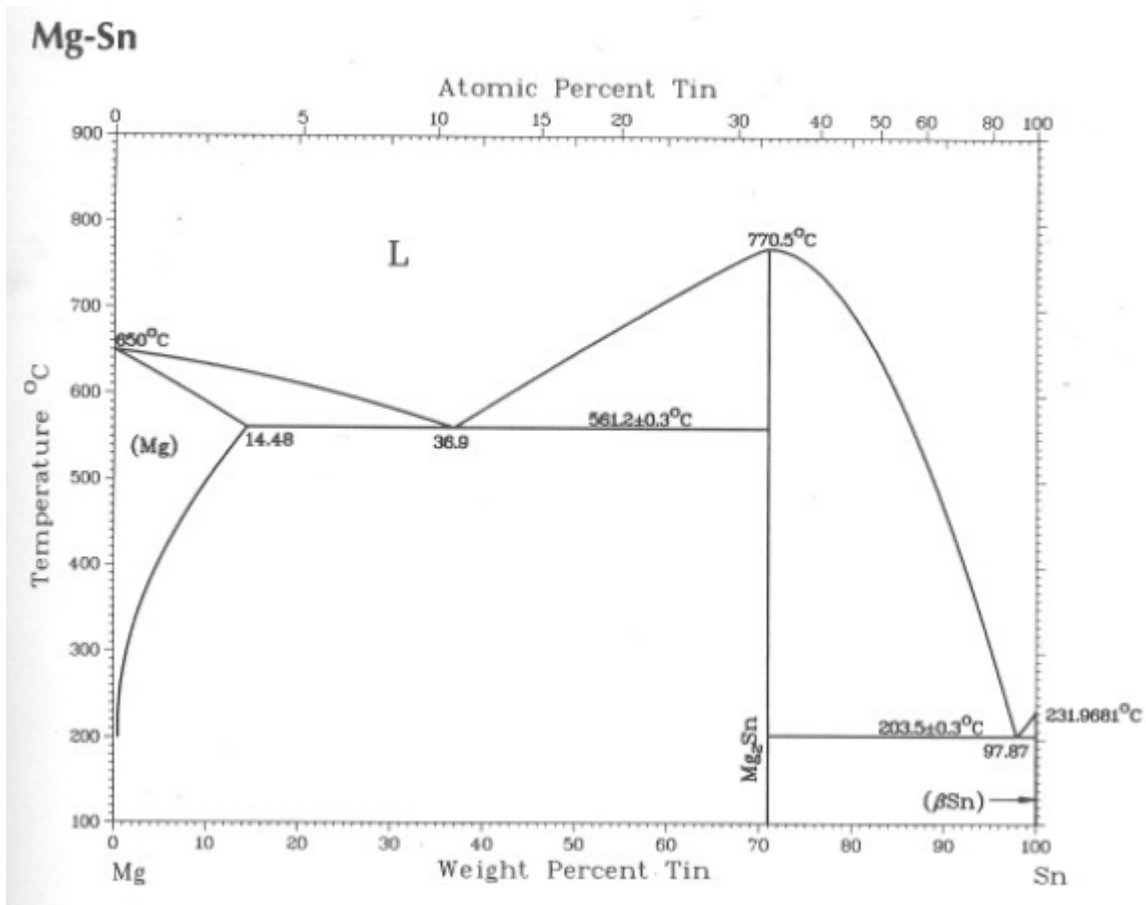
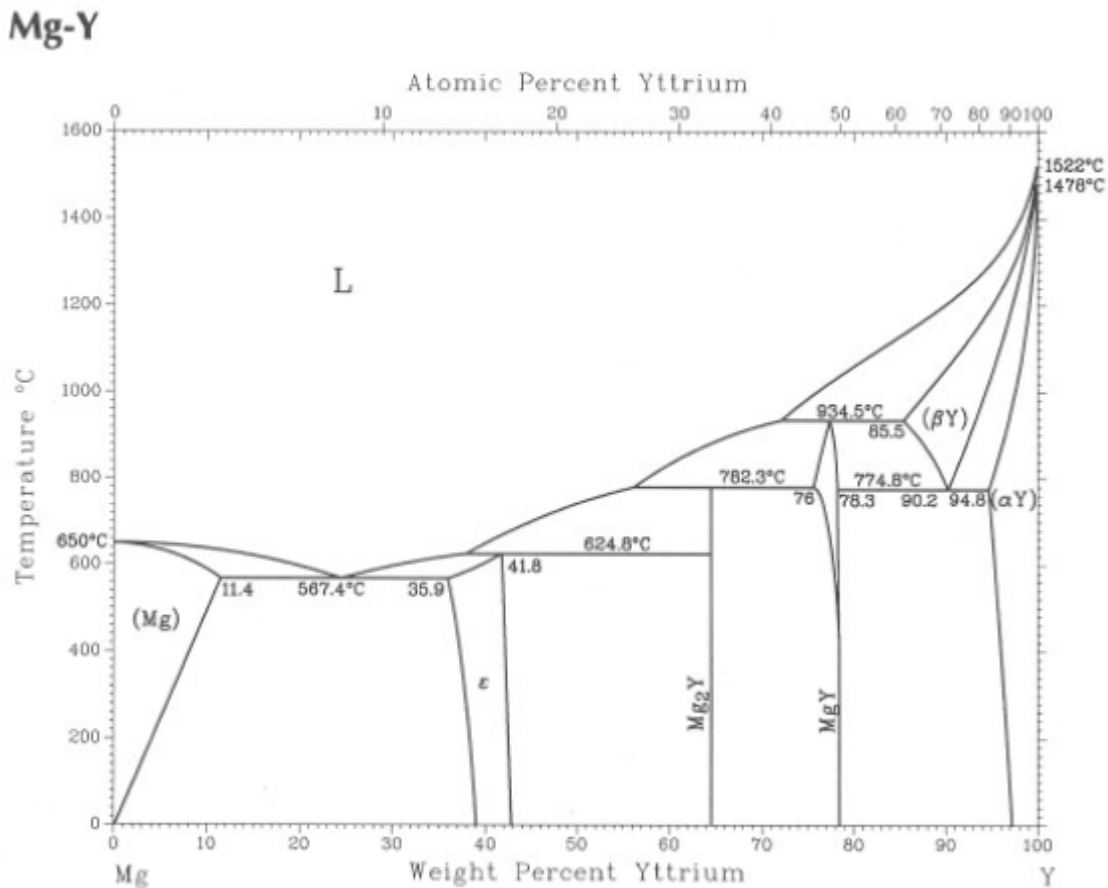


Figure 1.8 - Tin - magnesium binary phase diagram. [1]

Figure 1.9 shows the binary phase diagram of yttrium and magnesium. Yttrium is used in some high temperature wrought alloys, where mechanical properties are secondary to creep resistance. Yttrium is of use to magnesium P/M because like, calcium, it will disrupt the oxide of magnesium to improve sintering response. At higher sintering

temperatures, a eutectic liquid forms which may help distribute the Y to have a greater layer disruption effect. However, the large number of phases and intermetallics that are possible make it difficult to predict the behaviour of Y during sintering. Also, yttrium has such a strong affinity for oxygen that it may form its own surface layer, hindering any beneficial reactions with magnesium.



**Figure 1.9 - Yttrium - magnesium binary phase diagram. [1]**

The zinc - magnesium binary phase diagram is shown in Figure 1.10. Zinc is commonly used in cast and wrought alloys as a solid solution strengthener. Zinc is almost

always used along with aluminum additions because it has the ability to refine the bulky Al - Mg precipitates and increases their hardening effect. In the case of P/M, the low melting point of zinc allows for liquid phase formation, but it is highly transient. There are also a number of intermetallics that may form and reduce the amount of pure zinc available to contribute to the liquid phase.

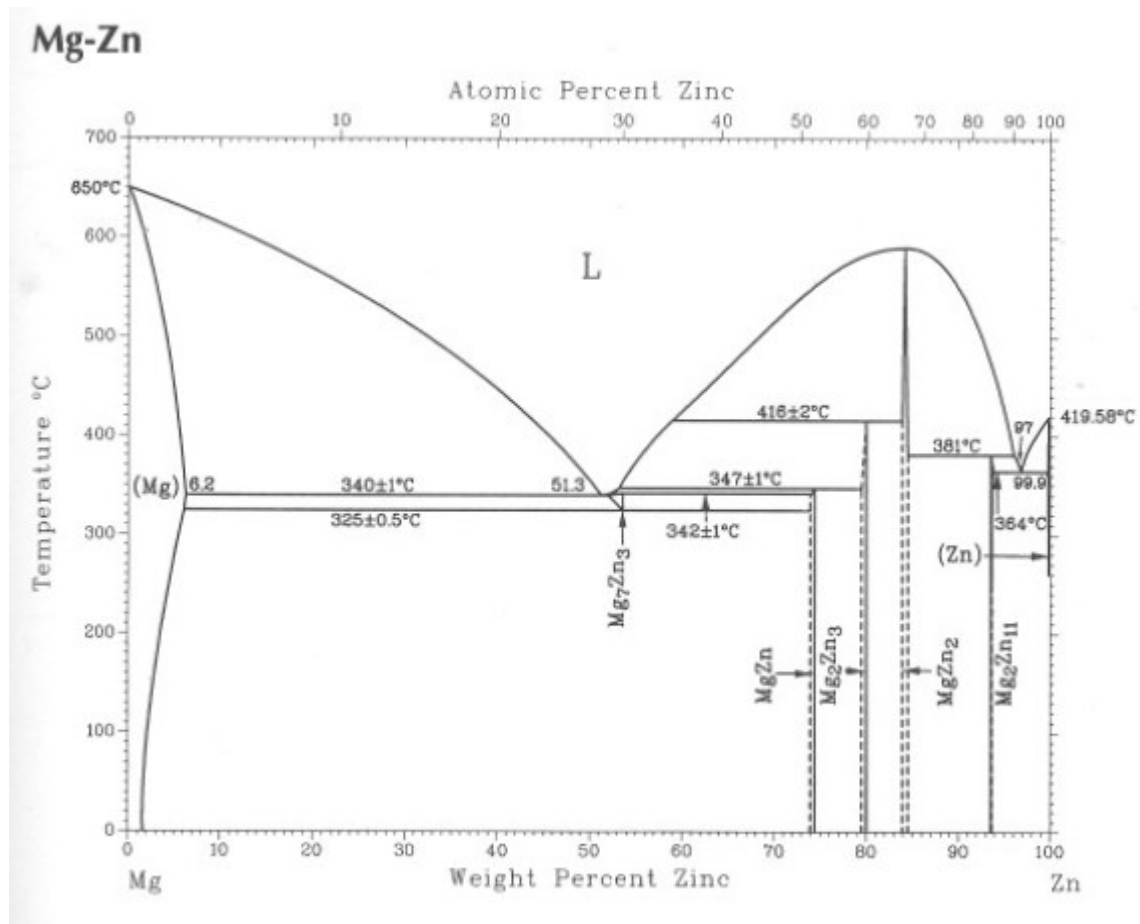


**Figure 1.10 - Zinc - magnesium binary phase diagram. [1]**

Figure 1.11 is the ternary phase diagram of magnesium, aluminum and zinc at room temperature. There are a large number of phases and compounds that may form

even at room temperature. The complete three-dimensional ternary diagram would reveal a complex heating and cooling path for a given alloy. Therefore, understanding the sintering behaviour of ternary, quaternary and multicomponent alloy systems requires specialized computational software.

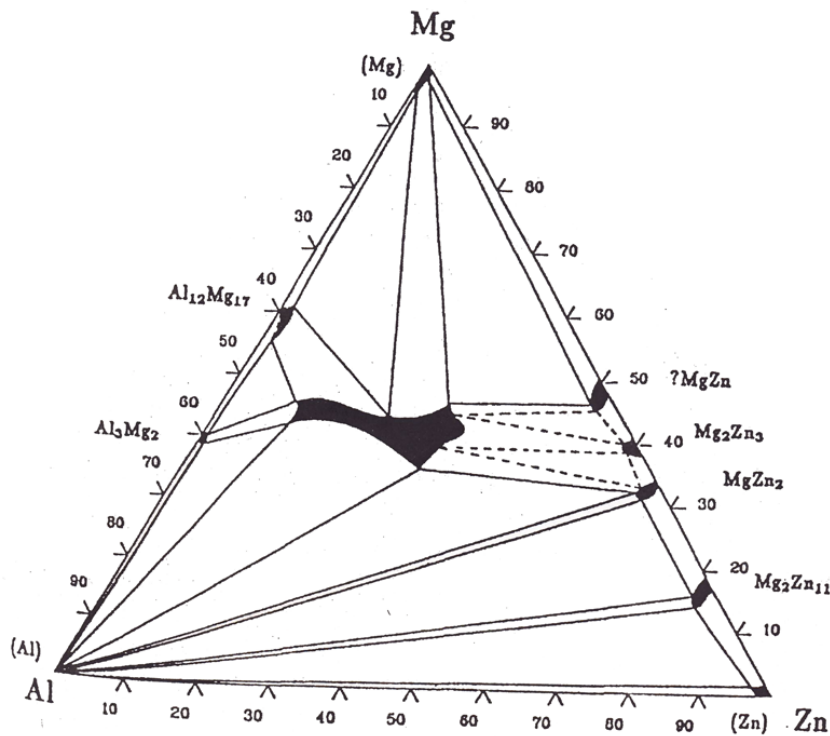


**Figure 1.11 - Aluminum - zinc - magnesium ternary phase diagram. [1]**

### **1.2.3 Alloying Theory**

The properties of pure magnesium are insufficient for structural uses, and pure magnesium is rarely used in the unalloyed form. Magnesium is alloyed with other metals to increase strength, corrosion resistance and formability. Alloying additions are categorized by their effect on the base magnesium. Elements such as aluminum and zinc

are solid solution strengtheners, allow for precipitation hardening, and also widen the freezing range to improve castability. Additions of lithium and neodymium can be used to change the hexagonal crystal structure to a more formable cubic. Because of the limited slip systems in HCP magnesium, increased strength is realized with decreasing grain size, according to the Hall-Petch effect. Another common alloying addition is zirconium, which is a strong grain refiner in magnesium.

### 1.2.3.1 P/M Alloying Theory

In a powder metallurgy product, where the starting material is fine powder and is never subjected to temperatures above melting, grain refinement is not possible or necessary. The minimum grain size is largely established by the original size of the powder, and sintering kinetics determine final grain size. Therefore, traditional alloying additions used for grain refinement are redundant for P/M alloys. However, grain refinement of wrought and cast alloys takes place through surface modification of the base magnesium. In P/M alloys where grain refinement is not possible, this surface modification may still be beneficial to sintering.

The group of alloying additions that are used to change crystal structure are also not necessary for a P/M product. One of the key advantages of powder metallurgy is the net and near-net shape processing, where no secondary forming is required to produce the final product. Because of this feature, the difficulty in forming that is inherent with HCP crystal is circumvented, and changing to a cubic structure is unnecessary.

The design of alloys for powder metallurgy is mainly concerned with improving strength, ductility and corrosion resistance. The common approach for new P/M alloys is to mimic wrought and cast alloys. While this is useful in comparing the properties of P/M to cast and wrought, it makes use of alloying additions that may not be useful for P/M processing, and does not address challenges that are P/M specific. New P/M specific alloying additions and alloys will need to be designed to take advantage of the benefits, and avoid the problems associated with powder metallurgy.

To increase the sintering response of a P/M alloy, a low melting point metal is often added to provide more area for diffusion to occur. Additions of tin or lithium, which are not traditional magnesium alloying elements, will form a liquid phase at low temperature. Also, traditional strengthening element Zn forms a similar liquid phase. Another consideration is low melting point eutectics that form between magnesium and the alloying addition, or between two alloying additions. Because of the local composition effect in P/M, even very small additions that would form solid solutions in wrought and cast alloys may briefly form a liquid phase. The traditional alloying addition of aluminum has two possible eutectic liquids with magnesium, and alloying elements added for surface layer disruption, such as calcium and yttrium, also may form liquids.

Because the alloy is never molten during processing, the surface layer on the original powder is of great concern. Any impurities on the surface may become a barrier to diffusion and densification. Also, while the bulk of the part does not melt, there may be certain constituents of the alloy that form a liquid during sintering. The fraction of

liquid must be controlled to prevent excessive dimensional change during sintering, and the behaviour of the liquid, either transient or persistent, will affect sintering performance. If a metal with a more stable oxide to disrupt the surface layer, or a liquid phase forming metal is added, there is the possibility that some of the addition will remain unreacted and go into solid solution or form an intermetallic compound. Therefore it is important to consider the effect on other properties when adding alloying elements for P/M specific purposes.

## **1.3 Sintering**

### ***1.3.1 Solid State Sintering***

The basis of solid state sintering is the development of interparticle bonds between adjacent particles. A neck is formed between particles by means of mass transport, and as sintering progresses the neck grows and the particles coalesce. Figure 1.12 shows a computer model of solid state sintering, starting with two evenly distributed powders. As time advances the small particles grow, small pores collapse and large pores form. From start to finish, there is a small dimensional change [3].

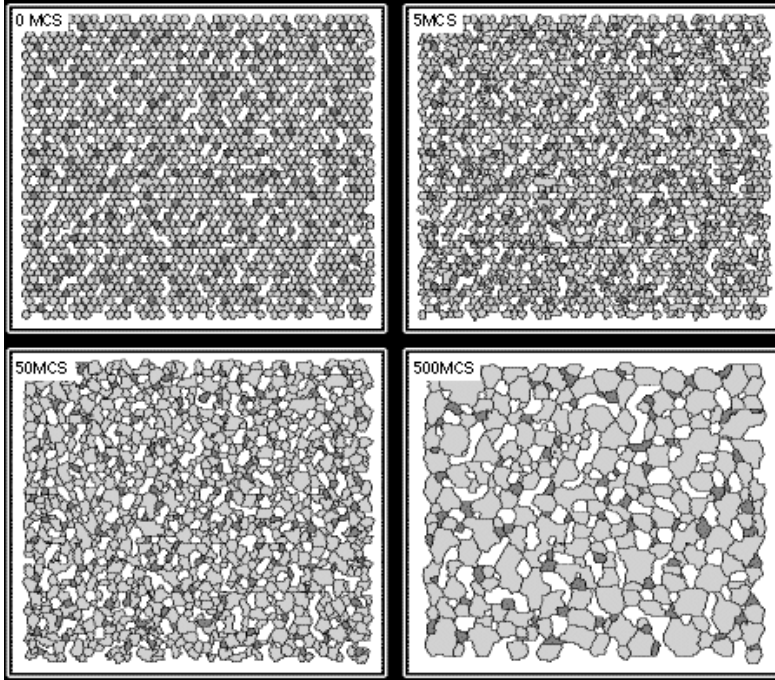


**Figure 1.12 - Computer model of solid state sintering. [4]**

During solid-state sintering there are several proposed mechanisms that explain densification of the movement of atoms or vacancies to the boundary between two powder particles that form the neck. These mechanisms are grouped into two categories, surface transport mechanisms and bulk transport mechanisms. In surface transport, movement can be explained by evaporation and condensation, surface diffusion and volume diffusion. Bulk transport mechanics include volume diffusion, grain boundary diffusion and plastic flow. [3]

The first surface transport mechanism is graphically represented in Figure 1.13. During evaporation and condensation, an atom at  $P1$  evaporates from the surface of one

of the powder particles and then condenses at the boundary between the two particles at  $P_2$ .

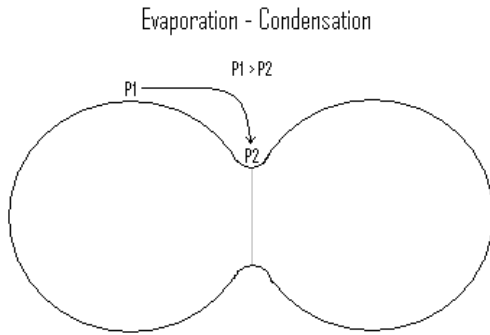


**Figure 1.13 - Evaporation and condensation surface transport.**

The next surface transport mechanism is surface diffusion, shown in Figure 1.14. In this type, atoms from the surface of the powder particles at 1 travel along the surface of the particles toward the low energy boundary at 2.

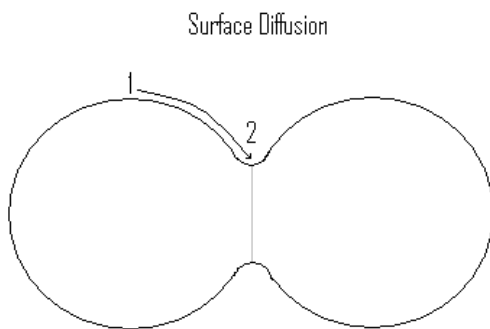


**Figure 1.14 - Surface transport by surface diffusion.**

Volume diffusion can be either a surface or bulk transport mechanism. As shown in Figure 1.15, atoms from the surface, *1a*, or from the bulk of the powder, *1b*, diffuse through the particle to the neck at *2*.

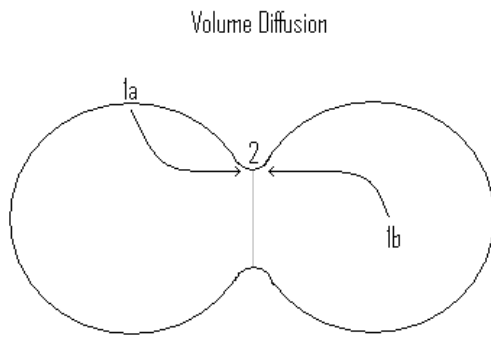


**Figure 1.15 - Atom transport by volume diffusion.**

In the bulk transport category, the first is grain boundary diffusion, as shown in Figure 1.16. Atoms from site *1* diffuse through the grain boundary from the bulk of the neck to the surface at *2*.

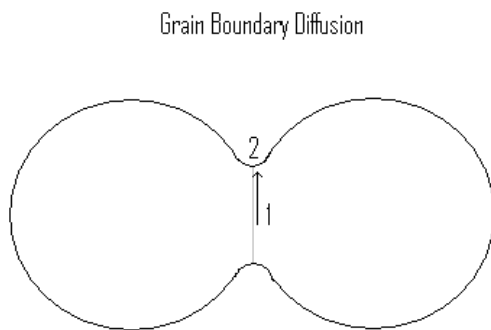


**Figure 1.16 - Bulk transport through grain boundary diffusion.**

The other type of bulk transport is plastic flow, as shown in Figure 1.17. A dislocation from the bulk of the powder particle, 1, flows plastically through the particle to the neck at 2.

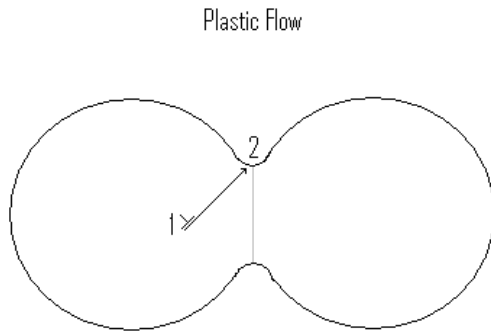


**Figure 1.17 - Bulk transport by means of plastic flow.**

In solid state sintering, there are four discrete stages of sintering. The first stage, graphically represented at the far left of Figure 1.18, is the point contact between adjacent powder particles. The next stage is termed the initial stage, where necks are beginning to form between particles and pores are collapsing. In the intermediate stage, the necks continue to grow and pores shrink further, but there is still a definite grain boundary between the original powder particles. In the final stage, these boundaries disappear and the particles become a homogenous body.

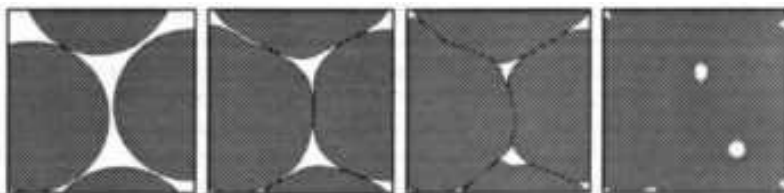


**Figure 1.18 - Four stages of sintering. [3]**

During the intermediate stage of sintering, densification and therefore strength can be improved through mass transport and a phenomenon known as Ostwald ripening [3]. In Ostwald ripening, vacancies from small pores flow to large pores, and mass from large pores flows to small pores. This effectively eliminates small pores at the expense of growing other larger pores, as shown in Figure 1.19.

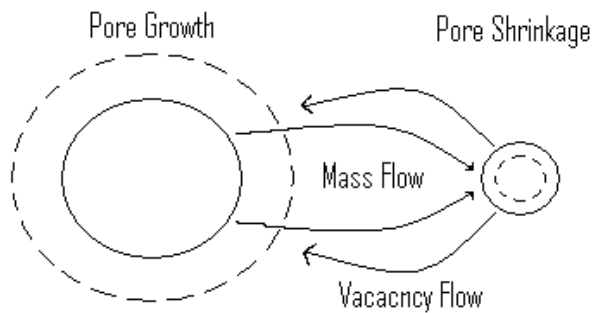


**Figure 1.19 - Densification through Ostwald ripening.**

### ***1.3.2 Liquid Phase Sintering***

Liquid phase sintering requires that one or more of the powders or compositions in the compact have a melting temperature lower than the sintering temperature. This powder will melt and flow through the solid particles. In Figure 1.20, the black powder liquefies and flows through the solid grey powder, which undergoes solid state sintering, and fills pores. The result is a solid with very high density but that has lost some dimensional stability. It is the lack of dimensional stability that makes thermodynamic predictions in sintering insufficient.

Aside from the additive having a lower melting point than the base powder, the key features of an ideal liquid phase sintering system are that the solubility of the additive in the base should be low, as this ensures that the additive remains segregated to particle boundaries and maximizes the liquid volume. The base powder should also have a high diffusivity in the liquid. This ensures high rates of mass transport and therefore rapid sintering. Completely miscible liquids are desirable because they ensure that mass transport is not constrained.

Instead of producing sintered alloys which simply mimic existing wrought alloys, it is preferable to develop alloys that are designed to be sintered. P/M specific alloys can be designed to take advantage of liquid phase with non-traditional alloying elements.

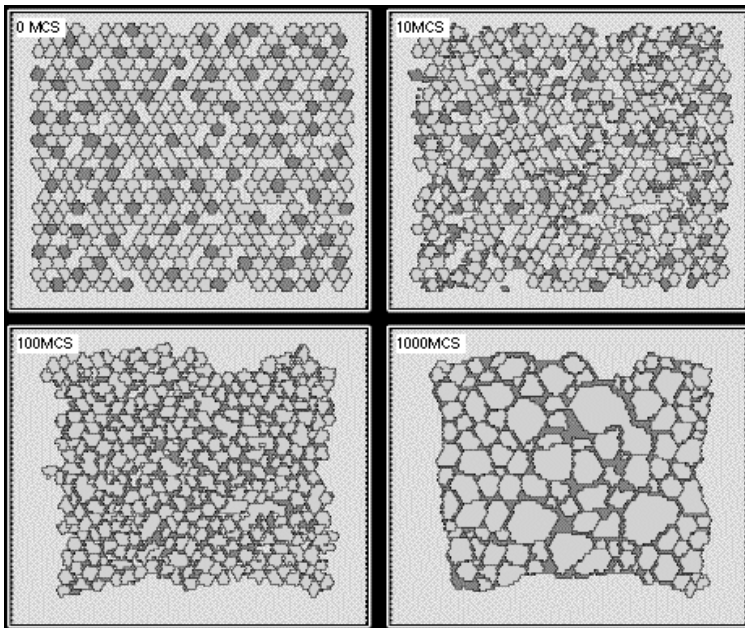


**Figure 1.20 - Computer model of liquid phase sintering. [5]**

In liquid phase sintering, there are two possible behaviours that may take place, transient liquid phase or persistent liquid phase. The transient liquid phase has a liquid that disappears during the sintering cycle due to the dissolution into the solid or formation of a new phase, typically a compound. This phenomenon is usually undesirable because the liquid will not help densify the compact and pores will remain.

In persistent liquid phase sintering, the liquid phase exists throughout the high temperature portion of the sintering cycle and can be formed by use of pre-alloyed powder or by inducing melting in a mixture of powders. The requirements for a persistent liquid phase are that the solid must be soluble in the liquid to ensure the liquid will wet the solid, and the diffusion kinetics for the dissolved solid must be fast enough to ensure rapid sintering.

As with solid state sintering, surface energy provides the driving force for densification in liquid-phase sintering. Final elimination of porosity and its associated surface energy requires grain shape accommodation, which is dependent on the relative energy of the solid-liquid interface. During liquid state sintering, several steps have been recognized. The first step is particle rearrangement when the liquid forms and wets the solid structure, followed by the second step when solution-re-precipitation becomes active, leading to pore elimination by grain shape adjustment. The third step, microstructural coarsening, is characterized by Equation 1.2 [3], where  $P$  is the capillary pressure,  $\gamma_{LV}$  is the surface energy and  $R_i, R_j$  are the radii of two adjacent particles.

$$\Delta P = \gamma_{LV} \left( \frac{1}{R_i} + \frac{1}{R_j} \right)$$

1.2

During the initial stages of sintering, the liquid segregates to surfaces to reduce the total surface energy. Examination of the phase diagram makes it possible to determine the temperature of liquid-phase formation and the composition of the liquid at this point. The greater the separation of the solidus and liquidus curves, the greater the solute segregation. The liquid will penetrate grain boundaries, leading to thin segregate layers responsible for rapid sintering.

Spreading is the kinetic process associated with wetting and it is important in the early portion of liquid-phase sintering, since often liquid forms at a local region where the concentration of the liquid forming powder is high. The liquid must travel from these areas to the remainder of the compact. For this to take place, the liquid must wet the solid powders. For a liquid to wet a solid, the total free energy must decrease along with the contact angle, as shown in Figure 1.21.

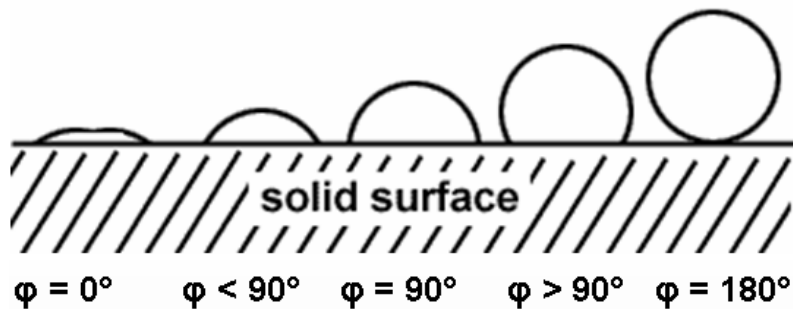


**Figure 1.21 - Liquid wetting a solid surface.**

If the liquid has a high solubility in the solid, this leads to a transient liquid phase. The liquid will be absorbed by the solid during the sintering cycle. If the solid solubility in the liquid is high a persistent liquid phase is formed, which favors densification. Small grains have a higher solubility than large grains and this sets up the condition for grain coarsening by solution re-precipitation.

Because of capillarity behaviour during liquid-phase sintering the wetting liquid preferentially flows into the smallest pores of the compact. If liquid formation is from large powder particles, then on melting the liquid will flow into neighboring small pores and leave behind a large pore. Therefore it is beneficial to use a small particle size for the liquid forming powder.

### ***1.3.3 Sintering Atmosphere***

The atmosphere in which the sintering is done will affect the final properties of the compact. The atmosphere can reduce or minimize the extent of oxidation on the surface of powder particles and is also responsible for transporting all lubricant vapours and residues from the sintering section of the furnace. The choice of atmosphere will depend on the metal being sintered and the goals for the final product, and can include inert gases, reducing gases or a complete vacuum.

In the case of aluminum P/M, research has been completed on the effect of different sintering atmospheres on densification [6]. It was found that any hydrogen

impurities in the sintering gas would severely affect the final properties regardless of the gas being used. Argon and nitrogen were tested, and it was found that during sintering, the pores in the compact would fill with gas, and as sintering progressed and interparticle bonding took place, the gas became trapped in the pores.

In the case of argon, the pressure of the gas inside the pores does not allow pore elimination and densification to take place. When sintered in nitrogen, the N gas trapped in the pores reacted with the surrounding aluminum and reduced the pressure inside the pore and densification can proceed. The reaction produced a surface layer of AlN on the powder, which was also found to have superior wetting properties and enhanced liquid phase sintering as well. It is possible a similar reaction with nitrogen, or another reactive gas, may be possible to increase the sintering response of magnesium [7].

#### ***1.3.4 Surface Layer***

Most metal powders exposed to air are covered by a surface layer. The layer is typically composed of oxides, but may also contain hydroxides, carbonates or other compounds formed by reactions with the atmosphere. This layer prevents solid-state sintering in low melting point metals. Most commercial magnesium powders are produced by mechanical grinding. The low cost and less restrictive requirements for its main intended use as a reactant make grinding attractive. For P/M applications the angular morphology of the powder gives good green strength because of mechanical interlocking, but the powder particles are typically covered by a thick surface layer due to long exposure to air during the grinding process. Recently, magnesium powder was also

produced commercially by centrifugal atomization by Tangshan Weihao Magnesium Powder Co. The product has very little surface oxidation due to the inert production conditions, and vacuum for transportation, but the spherical morphology gives poor green strength.

The oxide layer needs to be reduced or otherwise removed to enable effective sintering. This can be accomplished with a thermodynamically unstable oxide, where some combination of temperature, pressure, atmosphere or the addition of a more reactive metal will cause the oxide layer to become unstable [8]. The oxide is then reduced and the sintering kinetics are similar to the pure metal. In the case of magnesium, the oxide is especially stable and the only option to disrupt the surface layer is the addition of a metal with a more stable oxide.

If the oxide layer is unstable with respect to dissolution in the parent metal at high temperature, this can be utilized for sintering. The sintering process is preceded by an incubation period dictated by the kinetics of dissolution and diffusion of oxygen and the parent metal. At sintering temperature, the oxide layer then dissolves into the parent metal. The incubation period for Fe is very short at approximately 10 seconds [8]. Therefore, iron can be readily sintered even when covered by an oxide layer. However, the incubation period for low melting temperature metals such as magnesium have incubation periods upwards of one hundred days [8]. This explains why ferrous alloys dominate the P/M industry.

Another mechanism to remove an oxide layer can be used with metals that have a low oxygen solubility and high oxide stability. In this case metal atoms will diffuse through the oxide layer and the neck will form on the surface. If the rate of diffusion through the metal oxide is similar to the metal diffusing through itself, then sintering is not retarded by this process. As shown in Table 1.4 [8], the rate of diffusion of copper through its oxide is actually faster than through itself, so sintering is not hindered by the presence of a surface layer. This leads to copper P/M being second only to ferrous P/M. In the case of aluminum and magnesium, the diffusion rate through its oxide is orders of magnitude slower than through itself. However, sintering is still possible, but at an increased duration.

**Table 1.4 - Diffusion rates of a metal through itself, and through its oxide. [8]**

	$D_M$ $m^2 \text{ sec}^{-1}$	$D_{Ox}$ $m^2 \text{ sec}^{-1}$
<b>Cu</b>	$5.65 \times 10^{-13}$	$6.65 \times 10^{-12}$
<b>Al</b>	$1.84 \times 10^{-12}$	$5.51 \times 10^{-30}$
<b>Mg</b>	$3.01 \times 10^{-12}$	$5.25 \times 10^{-24}$

A way to bypass the oxide layer is by creating cracks and pores through it. During compaction, the force exerted on the powder is enough to break the oxide layer, as shown in Figure 1.22, creating short circuit pathways for unimpeded sintering. Also, during heating of the powder, any hydroxide or carbonate that is part of the layer may decompose, which will create pores in the layer as gas is released. If there are adjacent

cracks or pores in two particles, rapid sintering will take place at that local area. However, if a point contact between particles does not have a break in the layer, diffusion is still impeded.

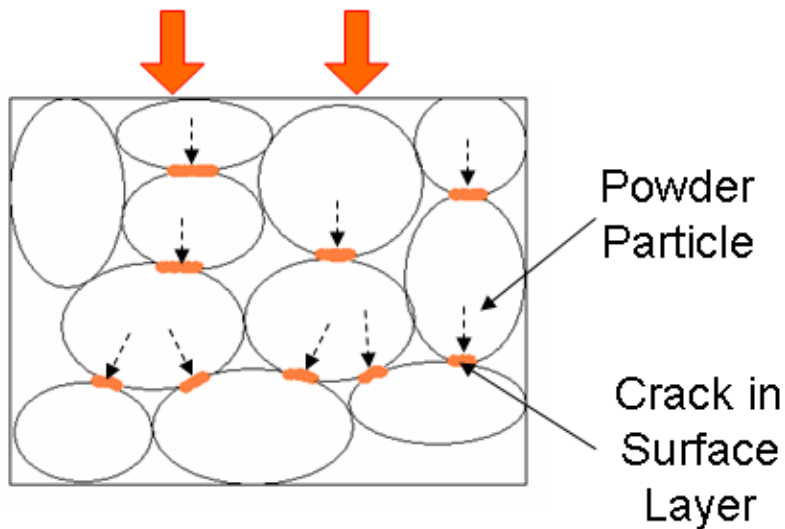


**Figure 1.22 - Force of compaction creates cracks in surface layer.**

The use of a liquid phase is an alternative to solid-state sintering, and may reduce the problem of an oxide layer on powder particles by further exploiting breaks in the surface layer. As the liquid spreads between the particles, any cracks or pores become short circuit pathways, regardless of whether they are directly adjacent to another crack in a neighbouring particle. This allows for reduced sintering duration.

### 1.3.5 Vacancy Generating Processes

A vacancy generating process occurs in a system that has excess free volume, such as pores or voids in a powder metallurgy compact. During sintering, the pores are accommodated by the crystal bulk and released as atomic vacancies [9]. Equation 1.3 shows the total free energy in the system, which is the sum of the contribution of the vacancies ( $G_{vac}$ ) and the bulk ( $G_{non-vac}$ ).

$$\mathbf{G} = \mathbf{G}_{non-vac} + \mathbf{G}_{vac} \quad 1.3$$

The ideal solution of vacancies is shown in Equation 1.4, where  $n$  and  $N$  are the number of vacancies and the number of atomic sites per unit volume, respectively,  $H_v^f$  is the vacancy formation enthalpy,  $k$  is the Boltzmann constant and  $T$  the absolute temperature.

$$G_{vac} = nH_v^f - kT \ln \frac{N!}{(N-n)!n!}. \quad 1.4$$

Then, the concentration of vacancies ( $c$ ) and the concentration at equilibrium ( $c^{eq}$ ) are substituted into the previous equations, resulting in Equation 1.5.

$$G = G_{\text{non-vac}} + G_{\text{vac}}(c^{\text{eq}}) + \frac{1}{2} \frac{NkT}{c^{\text{eq}}} (c - c^{\text{eq}})^2. \quad 1.5$$

If the concentration of vacancies with time is considered, the process is permitted thermodynamically if the derivative of  $G$  with respect to time,  $t$ , (denoted by a dot) is negative, as in Equation 1.6.

$$\dot{G} = \dot{G}_{\text{non-vac}} + \frac{NkT}{c^{\text{eq}}} (c - c^{\text{eq}}) \dot{c} < 0. \quad 1.6$$

Where Equation 1.7 represents the time derivative of the vacancy concentration, and the competition between the vacancy production ( $\dot{c}^+$ ) and the vacancy removal ( $\dot{c}^-$ ) rates.

$$\dot{c} = \dot{c}^+ - \dot{c}^- \quad 1.7$$

The dissolution of voids can be considered as an ensemble of identical voids of radius  $R_{\text{void}}$  in an otherwise uniform solid. The number of voids per unit volume,  $n_{\text{void}}$ , cannot change during the process if densification is to occur. The void sizes  $R_{\text{void}}$  and  $n_{\text{void}}$  are related to the volume fraction,  $f$ , of voids (porosity) by Equation 1.8.

$$f = \frac{4\pi R_{\text{void}}^3}{3} n_{\text{void}}. \quad 1.8$$

Substituting into Equation 1.5.

$$G = 4\pi R_{\text{void}}^2 \sigma^s n_{\text{void}} + G(c^{\text{eq}}) + \frac{1}{2} \frac{NkT}{c^{\text{eq}}} (c - c^{\text{eq}})^2. \quad 1.9$$

Considering the dissolution of voids with time, Equation 1.10 is generated.

$$\dot{G} = 8\pi R_{\text{void}} \sigma^s n_{\text{void}} \dot{R}_{\text{void}} + \frac{NkT}{c^{\text{eq}}} (c - c^{\text{eq}}) \dot{c}. \quad 1.10$$

Vacancy flux is shown in Equation 1.11, where  $D_v$  is the vacancy diffusivity and  $c_s$  and  $\bar{c}$  are the vacancy concentrations in close proximity of the void surface and in the bulk far away from it.

$$j = -D_v N \frac{c_s - \bar{c}}{R_{\text{void}}}. \quad 1.11$$

As a result, a pore in the center of a grain will gradually dissolve into vacancies and migrate to high energy areas such as grain boundaries, as shown in Figure 1.23.

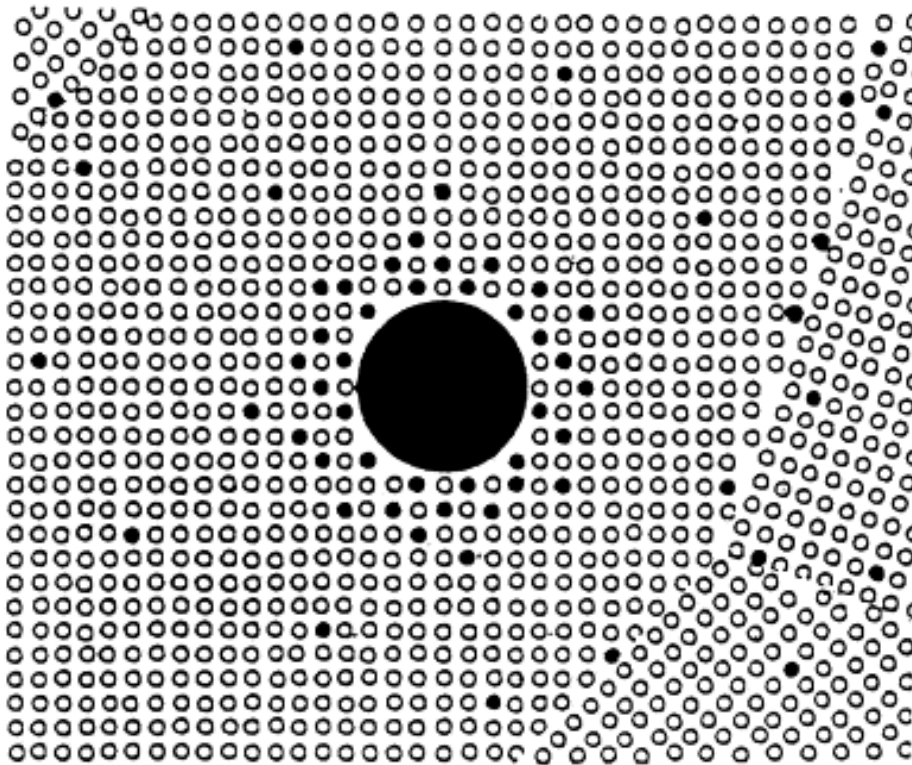


**Figure 1.23 - Schematic representation of a pore filling as vacancies are generated.**

[9]

### ***1.3.6 Super-Solidus Liquid Phase Sintering***

Traditional liquid phase sintering is accomplished by adding a small amount of a low melting temperature ‘binder’ phase. The liquid phase forming addition should follow the rules for solubility, diffusivity and wetting required for an ideal liquid phase. In addition, the low melting metal powder is required to have a very small particle size, to decrease the residual porosity after it has melted and spread.

Super-solidus liquid phase sintering (SLPS) starts with a pre-alloyed powder of the exact composition of the final alloy. A sintering temperature is chosen between the solidus and liquidus temperature for the composition of the alloy, and the liquid fraction can be controlled by the sintering temperature. The result are ‘mushy’ particles where liquid is found at grain boundaries as well as inside particles. The pre-alloyed powder removes the need for small grain size, and there is no residual porosity from a low melting addition. This results in much simpler, single powder, single step processing.

The higher the sintering temperature and therefore liquid fraction, results in a higher densification. However, higher dimensional change results with increased liquid fraction. It is crucial to identify the optimum sintering temperature in which densification is maximized but dimensional change is not an issue. Also, some additions, such as surface layer disrupters, may need to be in the elemental form for the greatest effect, and the pre-alloyed powder advantage is lost.

SLPS powder metallurgy magnesium may be advantageous, primarily because the elements added to form liquid phases typically form eutectics with magnesium, and therefore the residual porosity is not only the size of the original powder, but also the area of magnesium surrounding it that reacted with the powder to form the liquid. But the primary barrier to magnesium P/M is the surface layer on the powder, and additions to disrupt the layer may still be required. However, a pre-alloyed magnesium powder may have a less stable and more easily disrupted surface layer than pure magnesium powder.

## 1.4 Analytic Techniques for Surface Layer Characterization

### 1.4.1 Surface Spectroscopy

Surface spectroscopy techniques can be used to investigate the composition and thickness of the surface layer covering powder particles. Transmission electron microscopy (TEM), x-ray photoelectron spectroscopy (XPS), auger electrons spectroscopy (AES) and secondary ion mass spectroscopy (SIMS) are standard techniques, and are compared in Table 1.5 [10].

**Table 1.5 - Comparison of surface spectroscopy techniques [10].**

<u>Technique</u>	<u>Advantages</u>	<u>Disadvantages</u>
TEM	accurate without standards	expensive; very small area analyzed
XPS	precise to $\pm 0.1$ nm for films $< 3$ nm	less precise for thicker films; calibration required
AES	inexpensive, readily available	not accurate, further calibration necessary
SIMS	qualitative film thickness	further calibration required

<u>Technique</u>	<u>Optimum range</u>	<u>Useful range</u>
TEM	$> 1$ nm	$> 1$ nm
XPS	$< 3$ nm	$\leq 20$ nm
AES	-	$< 4$ nm
SIMS	-	$\geq 20$ nm

#### 1.4.1.1 Transmission Electron Microscope (TEM)

The transmission electron microscope (TEM) is a visual technique, and offers the only true measurement of a surface layer. All other spectroscopy techniques calculate the thickness of the layer based on density assumptions. Figure 1.24 [11] shows a micrograph

of a niobium grain and its surrounding surface layer. There is a visible contrast difference in the layer, and the thickness can be directly measured.

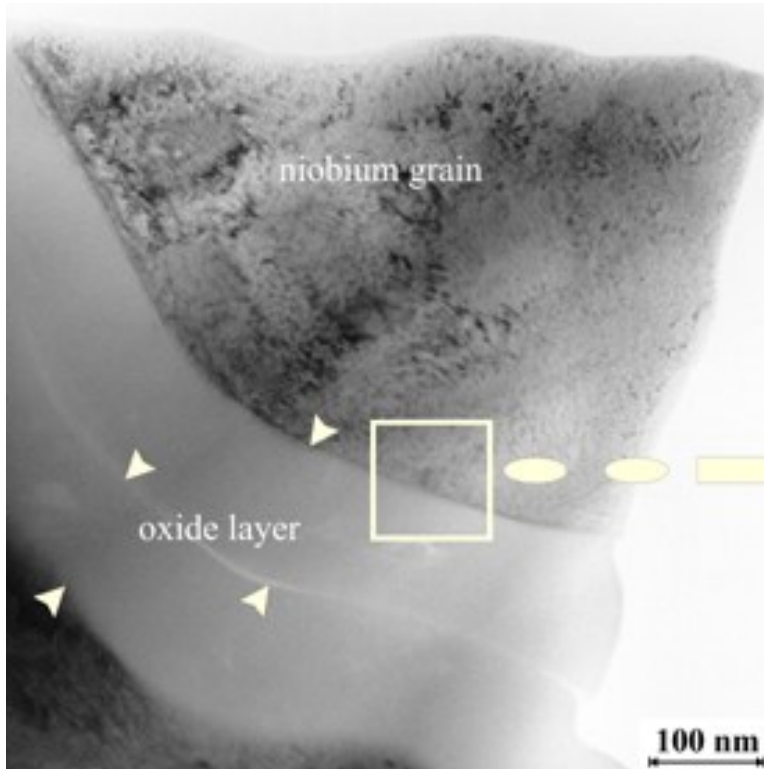


**Figure 1.24 - TEM micrograph showing the oxide layer on niobium. [11]**

#### *1.4.1.1.1 TEM Sample Preparation*

The transmission electron microscope requires that the sample to be examined is electron transparent. Traditionally a microtome is used to make very thin slices for analysis, but the blade used in these devices is quite fragile and cutting metallic samples is troublesome. Recently the micromachining capabilities of focused ion beam (FIB) systems have been utilized to prepare electron transparent samples. A diagram of a typical FIB system is shown in Figure 1.25. A source of gallium ions at the top of the

column can create an ion beam that can etch sections of the sample. Metals can be vapourized and deposited on the sample as well. An ion or electron detector are used for imaging.

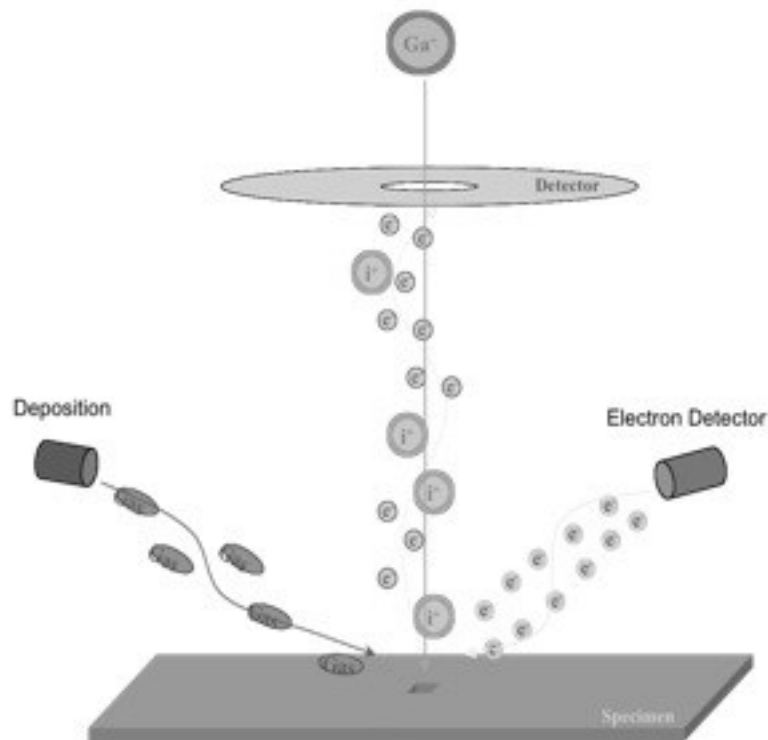


**Figure 1.25 - Diagram of FIB system.**

#### 1.4.1.2 X-ray Photoelectron Spectroscopy (XPS)

X-ray photoelectron spectroscopy (XPS) uses high energy X-rays to bombard the sample, and then measures the energy and number of electrons that escape the surface, as shown in Figure 1.26. The energy of the escaping electrons are characteristic to the elements, and the composition of the surface can be determined. Ion beam etching allows depth profiling by repeating the measurement after etching a known thickness off the

surface. Figure 1.27 shows an XPS experiment conducted on different thicknesses of silicon wafers [10].

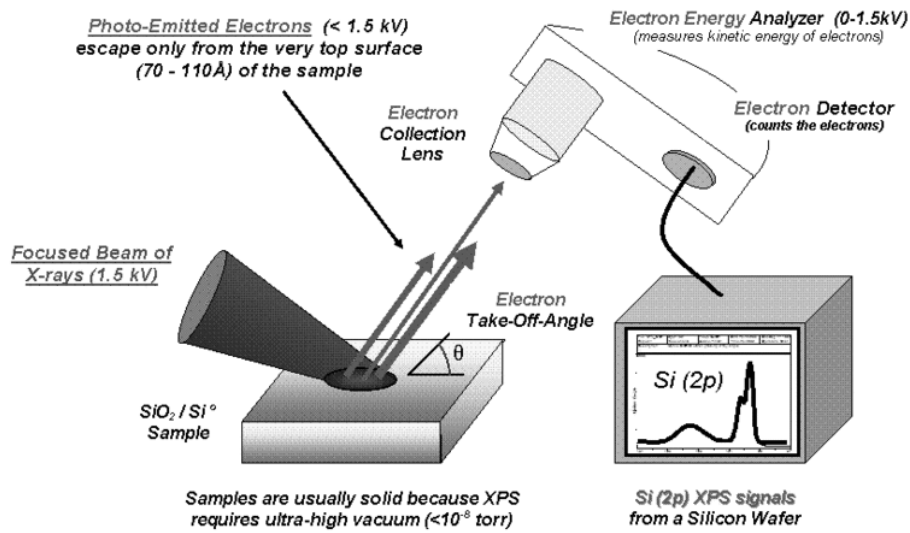


**Figure 1.26 - Diagram outlining the principles of XPS [10].**

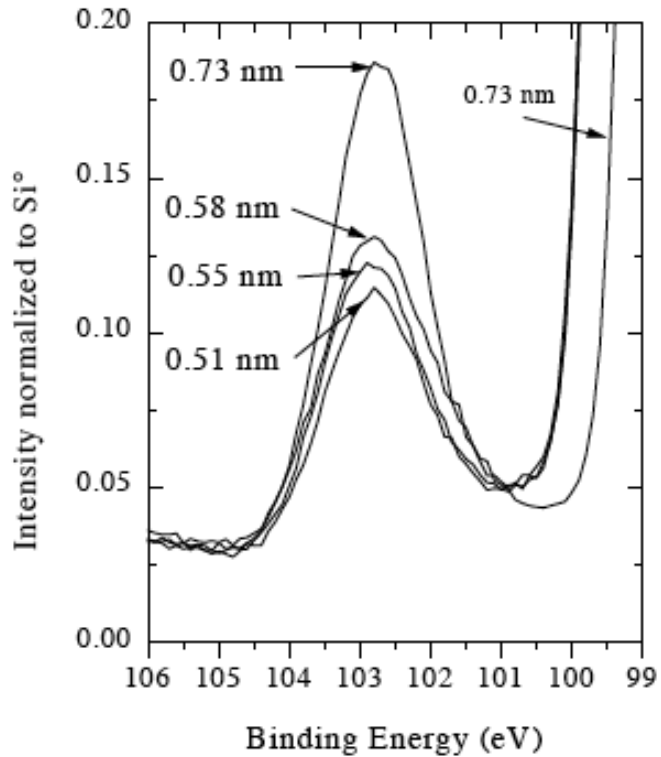


**Figure 1.27 - A typical XPS result, showing the intensity response to varying thicknesses of Si wafers. [10]**

#### 1.4.1.3 Auger Electron Spectroscopy (AES)

Auger electron spectroscopy (AES) utilizes an electron gun to produce a photon or electron that displaces a core state electron. As a result, a characteristic outer shell electron is emitted and its energy measured. A schematic of the apparatus is shown in Figure 1.28. Ion sputtering leads to depth profiling, similar to XPS. Figure 1.29 shows the result of a depth profiling experiment of the oxide layer on aluminum [10].

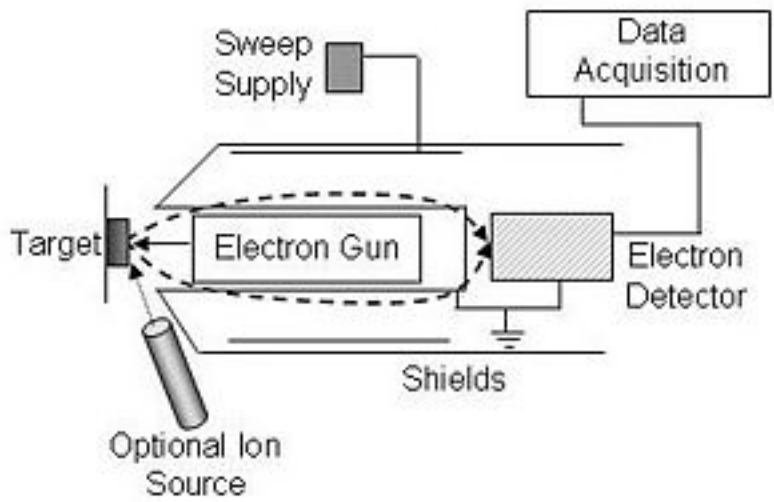


Figure 1.28 - Diagram outlining the principles of AES [10].

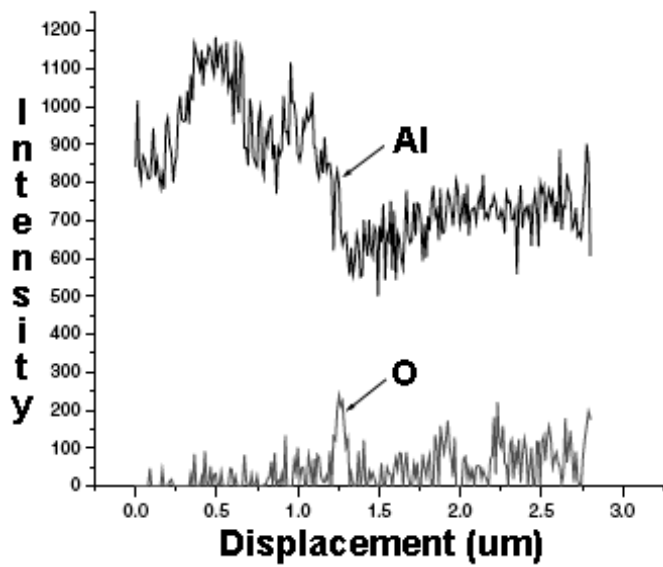
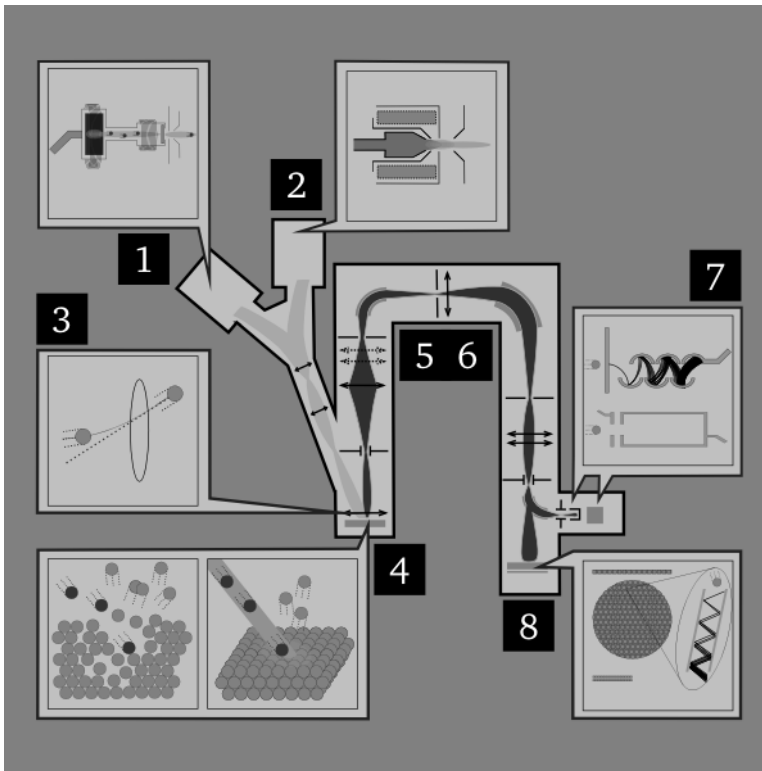


Figure 1.29 - AES depth profiling of an oxide layer on Al. [10]

#### 1.4.1.4 Secondary Ion Mass Spectroscopy (SIMS)

Secondary ion mass spectroscopy (SIMS) operates by sputtering cesium primary ions on the sample. The emitted secondary electrons are then analyzed by a mass spectrometer, as shown in Figure 1.30. Depth profiling is accomplished by measuring the drop in intensity vs the sputter rate. Figure 1.31 shows the result of an oxide thickness measurement by depth profiling the oxygen ion [10].



**Figure 1.30 - Principles of SIMS operation, where 1. Cesium ion source, 2. Duoplasmatron, 3. Electrostatic lens, 4. Sample, 5. Ion energy analyzer, 6. Mass analyzer, 7. Electron multiplier, 8. Ion image detector [10].**

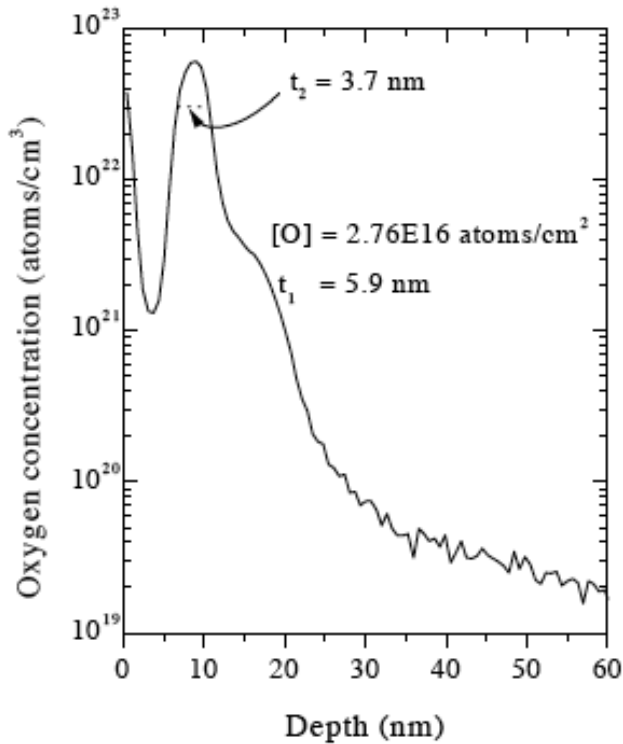


**Figure 1.31 - SIMS result of a depth profile on an oxide layer. [10]**

## **1.4.2 Thermal Analysis**

### **1.4.2.1 Dilatometry**

Dilatometry is a thermo-analytical technique for the measurement of expansion or shrinkage of a material when subjected to a controlled temperature/time program [12]. Dimensional change is recorded over a temperature range and can be used to find the coefficient of thermal expansion, sintering response (shrinkage), density change (constant mass), phase transformations (BCC - FCC Shrinkage) and glass transition temperatures.

#### 1.4.2.2 Differential Scanning Calorimetry (DSC)

Differential scanning calorimetry (DSC) is a technique where a difference in the amount of heat required to increase the temperature of a sample and a reference are measured as a function of temperature [12]. The sample and reference are maintained at nearly the same temperature during experiment and the difference in heat flow between the sample and reference relates to the amount of heat absorbed or released during phase transitions.

#### 1.4.2.3 Differential Thermal Analysis (DTA)

A differential thermal analysis (DTA) apparatus consists of a sample holder comprising thermocouples, sample containers, and a furnace [12]. Two thermocouples are connected to a voltmeter with one placed in an inert material such as  $\text{Al}_2\text{O}_3$ , the other placed in the sample. As the temperature is increased, there is a brief deflection of the voltmeter if the sample is undergoing a phase transition.

#### 1.4.2.4 Thermogravimetric Analysis (TGA)

Thermo gravimetric analysis (TGA) measures the change in weight with a change in temperature [12]. The analyzer consists of a high precision balance with a pan containing the sample. The sample is placed in a small electrically heated oven with a thermocouple to accurately measure temperature. The atmosphere may be purged with an inert gas to prevent oxidation or other undesirable reactions.

## 1.5 Forming and Shaping

Forming operations such as forging, rolling, swaging, extrusion and drawing induce large amounts of plastic deformation into a material. If the temperature at which the material is worked is below 60% of its melting temperature, it is termed cold working [13]. During cold working, strain hardening occurs as grains are deformed and the dislocation density increases. Strain hardening increases strength and hardness, but decreases toughness by increasing brittleness. Materials can be annealed after cold working to restore ductility through the nucleation of strain free grains at the boundaries of the previous grains.

If the forming operation takes place at a temperature above 60% of the melting temperature, associated with the recrystallization temperature, it is termed hot working [13]. Strain hardening of the material is reduced or eliminated as the nucleation of new strain free grains occurs directly following deformation. Because strain hardening does not occur, the formability of the material increases and the induced stress required for plastic flow is reduced. Hot working can therefore be completed using higher strain rates than cold working. Grain refinement is possible through hot working, due to the high number of nucleation sites available to form the new strain free grains.

A schematic representation of a hot rolling operation is shown in Figure 1.32. The large equi-axed grains of the starting material are elongated after a 50% reduction in area, but new grains begin forming quickly and replace the elongated grains with an

increased number of small equi-axed grains. Figure 1.33 shows similar behaviour in the case of hot extrusion, with the exception of a much greater reduction in area. The grains become highly elongated after the 99% reduction, which leads to greatly reduced grain size after recrystallization.

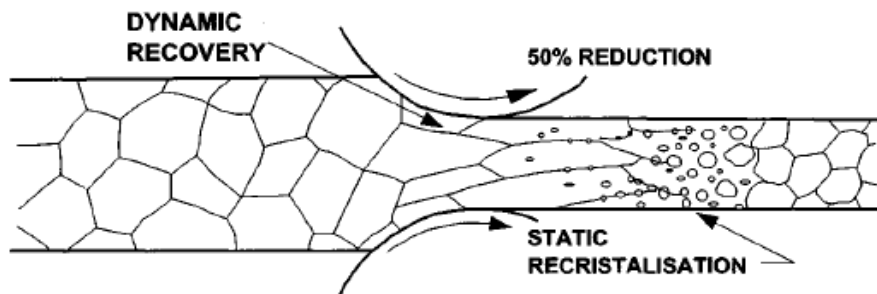


Figure 1.32 - Schematic diagram of hot rolling, showing the effect on grain structure. [13]

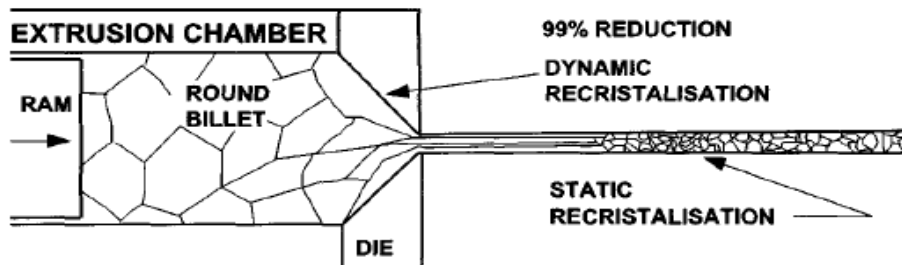


Figure 1.33 - Schematic diagram of hot extrusion, showing effect on grain structure. [13]

## 1.5.1 Hot Work of Magnesium

### 1.5.1.1 Deformation Mechanisms

Magnesium forms a hexagonal closed packed crystal structure at all temperatures [1]. Figure 1.34 shows the atomic locations in the HCP structure [1]. Unlike the other common metallic crystal structures of body centered cubic (BCC) and face centered cubic (FCC), HCP has a limited number of slip systems in which deformation can occur. It is the limited slip systems that leads to the poor formability of magnesium. The main deformation mechanism associated with HCP structures is twinning, where the crystal deforms under c axis compression and folds over itself. In magnesium, there is also a small amount of slip possible on the basal planes, and at higher temperatures the pyramidal plane becomes active to allow slip.

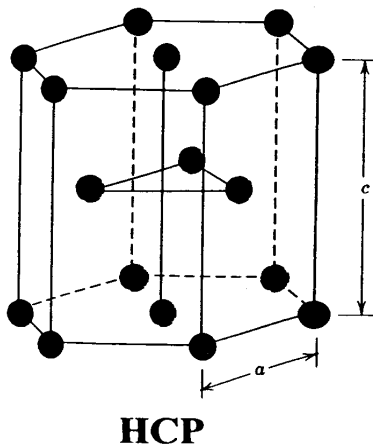


Figure 1.34 - Atomic locations in hexagonal closed packed crystal structure. [1]

### 1.5.1.2 Grain Size Effects

Using the Hall-Petch relation shown in Equation 1.12, the yield stress of a material can be estimated based on its grain size [13].

$$\sigma = \sigma_0 + Kd^{-1/2} \quad \mathbf{1.12}$$

Where  $\sigma$  is the yield stress,  $\sigma_0$  is the yield stress of a single crystal,  $d$  is the grain size and  $K$  is a constant. The constant  $K$  increases with increasing Taylor factor, which is mainly dependant on the number of slip planes available for deformation. In HCP metals such as magnesium, the slip systems are more limited than for BCC and FCC materials which increases the Taylor factor. The high Taylor factor and therefore  $K$  value for HCP metals results in a strong relation between grain size and strength [13].

To maximize the strength of magnesium and its alloys, a very small grain size is required. As can be seen in Figure 1.35, the slope of the HCP magnesium alloy is steeper than that of the FCC aluminum alloy. Also, the strength of the magnesium alloy is lower than the aluminum alloy at grain sizes larger than 2.2  $\mu\text{m}$ , but increases sharply as grain size is reduced.

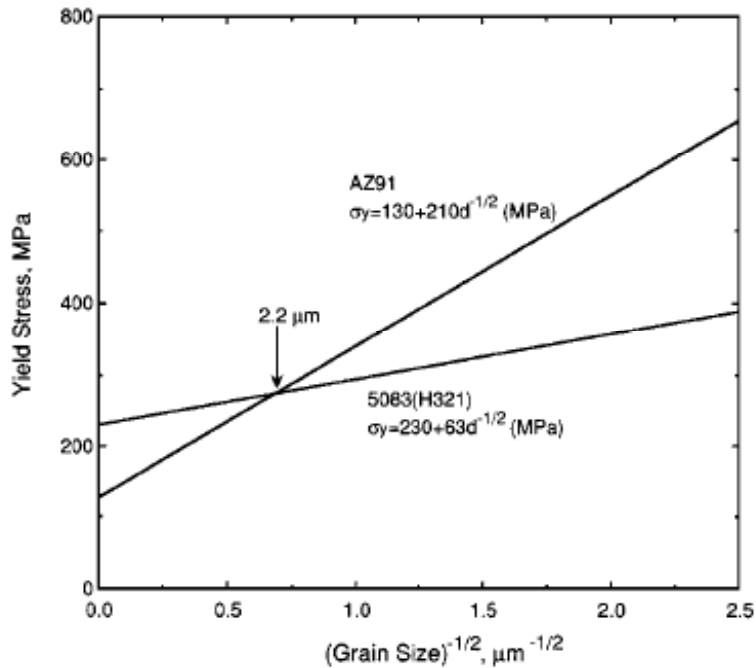


**Figure 1.35 - Yield stress as a function of grain size, AZ91 Mg alloy and H321 Al alloy. [13]**

Aside from the increase in strength, small grain sizes in magnesium alloys allows superplastic forming at high temperatures [13]. Very high elongations of 300% can be attained in superplastic metals, which can lead to production of near-net-shape parts. Ti and aluminum superplastic alloys see commercial use in aerospace applications, but few applications for superplastic magnesium are known at present. However, because of the difficulty in forming, superplastic magnesium alloys may be utilized in the near future in practical processing applications.

### **1.5.2 Industrial Practices for Wrought Alloys**

Industrially, magnesium products are produced in the wrought form by a number of forming processes, but chiefly include rolling and extrusion. Since low temperature

formability is poor, most processes use elevated temperatures. Figure 1.36 shows the effect of temperature on the deep drawing behaviour of magnesium sheet. It can be seen that a sharp increase in formability begins to occur at approximately 100°C. In comparison, the aluminum alloy shows fairly consistent drawability with temperature.

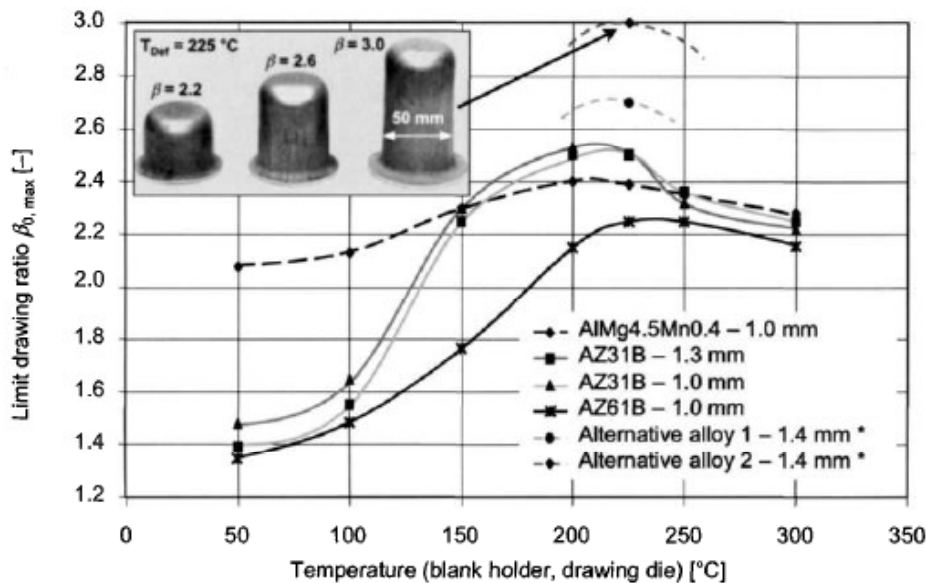


**Figure 1.36 - Deep drawing behaviour of Mg alloys. [13]**

Extrusion is used to produce many shapes of wrought products of magnesium. The extrudability of a material is measured by the speed in which it can be forced through the die. In the case of magnesium, the speed is lower and the pressure required is higher than that for aluminum [13]. This is mainly due to reduced mechanical properties found when extruding magnesium at high speeds, and also because of hot shortness. Hot shortness occurs if the alloy contains low melting point alloying additions or forms low melting temperature intermetallic phases, which may liquefy during extrusion. The liquid

between magnesium grains causes a loss of bonding, which reduces strength and allows the formation of cracks.

In general, magnesium alloys will undergo work hardening through twinning at forming temperatures up to 180°C, which limits strain rates because of low ductility [13]. At 240°C, basal slip planes become increasingly active and allow increased plastic flow. The activation of the pyramidal slip systems at 300°C reduces the amount of strain hardening and allows for additional plastic flow. At temperatures above 360°C, the recrystallization temperature of magnesium, no strain hardening can occur because of the formation of strain free grains. This drastically improves plastic flow and increases ductility.

## **1.6 Thermodynamic Calculations**

### ***1.6.1 Reactions Between Magnesium and the Atmosphere***

It is inevitable that at some point during the production of the powder or during processing that magnesium powder will be exposed to atmospheric gases. Oxygen is the most obvious reaction, forming MgO, which is believed to be the major component of the surface layer and in the literature it is generally considered to be the only component [13]. However, because magnesium is a highly reactive metal, several components of the atmosphere may react to form the compounds that make up the actual surface layer. Carbon dioxide and water vapour are two common components of atmospheric gases that may form compounds with magnesium.

### ***1.6.2 Decomposition of Components of the Surface Layer Formed on Magnesium***

The compounds in surface layer of magnesium may not be stable up to the sintering temperature, and may decompose to magnesium and a gas. Magnesium oxide will be stable up to temperatures beyond the vaporization of magnesium metal, so there is no possibility of its decomposition. Other components once they are identified may indeed decompose, most likely to the very stable MgO and a gas. The decomposition of these compounds could create stresses in the surface layer causing cracks to form. These cracks may then become pathways for unimpeded diffusion and assist sintering.

## **1.7 Previous Research of Magnesium P/M**

Limited research has been done on the use of powder metallurgy routes for the production of magnesium products. The research that has involved magnesium powder mainly uses P/M as a means to produce difficult to form alloys. These include metal matrix composites (MMC) [13-15], where P/M can alleviate some of the matrix/reinforcement interface issues when the matrix metal is in the molten state. The P/M method also allows a highly homogenous mixture of the reinforcement particles within the matrix, resulting in consistent mechanical properties in all directions. Difficulty to achieve successful sintering has brought into question the possibility of P/M to produce magnesium matrix composites [13]. The state in which the surface of the magnesium powder is before the P/M processing controls the sintering process. Obviously the methods of production of magnesium powder are critical in achieving the

properties required for a successful sintering. It appears that no attention has been paid into the characterization of the surface properties of the magnesium powders.

The other major research focus is the use of nano-sized base powders to produce a very fine grain structure in the final sintered product. With the greatly reduced grain size as compared to parts produced through ingot metallurgy, the strength and superplastic properties of the metal are proportionally increased [16]. Powders of alloys that contain rare earth elements and other additions are produced by atomization, where rapid solidification allows extended solubility not possible with ingot metallurgy. Alloying additions are chosen to improve strength, creep resistance and superplasticity [17].

Canned powder hot extrusion [16, 17] is the P/M method utilized to produce the majority of samples in both the MMC and grain refinement research primarily due to safety considerations. In this process, the base powders are blended and loaded into a thin-walled cylindrical vessel made from a highly formable metal such as aluminum or copper. The powders are vacuum de-gassed at an elevated temperature to remove air trapped between particles. Following de-gassing, the can is sealed. Extrusion takes place at sintering temperature and the reduction is typically between 10:1 and 20:1, allowing the powders to be compacted and sintered in one step. This process produces parts with very high densities, in the range of 98%+, but it is mainly a laboratory batch type procedure. To implement such a process on an industrial scale would be both costly and time consuming. It also forfeits near-net-shape processing, one of P/Ms key advantages.

However, these types of experiments indicate that if surface conditions are good sintering of magnesium can be successful.

Recently, new sintering and compacting strategies have been identified that may better address issues unique to magnesium. Equal Channel Angular Pressing (ECAP) [18] is a method to provide extremely high strain rates, equivalent to extruding at a 30:1 ratio, without a change in cross sectional dimensions. The high strain breaks any surface layer on the particles and plastically deforms the powders to ensure good interparticle bonding, and provides adequate pathways for diffusion. While cross sectional dimensions are retained, it is still only possible to produce rods of material, and not near-net-shape parts. Spray forming has been used to produce magnesium alloy billets [19]. Spray forming allows the direct rapid solidification and deposition of high density from a liquid alloy. The process has the benefit that contamination is minimized because powder production, compaction and consolidation are completed in one step. The process is somewhat net-shaped, as the spray can be manipulated as the layers are deposited, so simple two dimensional parts are possible. However, to realize full strength and density, the parts were first extruded.

Spark plasma sintering (SPS) has been used to produce alloys [20] and MMCs [21]. SPS enjoys very short sintering times, and the high energy pulse has been attributed to cleaning contaminants from powder surfaces in-situ. This can allow sintering of pure metals or alloy with no addition of sintering aids. Dies for the process are either graphite or metal and allow for near-net-shape production. However, the process is completed

under vacuum and under pressure, so the equipment is complicated and batch in operation.

The only known study to use the traditional press and sinter P/M route produced pure magnesium as well as Mg-Ca alloys [22] was published after the original submission of the present thesis. The process presented required a complex sintering apparatus to protect the samples from further oxidation during the long 64 hour time at temperature. Samples were placed in a covered holder, with the area around the sample holder filled with loose magnesium powder acting as an oxygen getter. Residual porosity of pure magnesium samples was 15% with sufficient oxygen getter in the sintering apparatus. Once alloyed with 1% calcium, porosity was reduced to 2% resulting in an increase in mechanical properties. The study concludes that the oxygen getter is essential for sintering magnesium and its alloys, and that calcium additions enhance sinterability through the formation of a transient liquid phase. However, there was no characterization completed on the powder and the surface layer was presumed to be entirely oxide. The role of calcium was also concluded to benefit sintering primarily by forming a liquid phase.

While the results of the press and sinter study [22] were promising, for magnesium P/M to compete on a level with aluminum P/M, simple, industrially relevant processing using existing P/M equipment is necessary. Because the economics of P/M require high volume, a robust process utilizing open to air uni-axial compaction and fast

sintering by mesh belt furnaces is needed to compete with established magnesium production methods like die casting.

The major issue in the development of the magnesium P/M is the availability of commercial magnesium powders. Unlike aluminum most commercial magnesium powders are produced by mechanical grinding. The low cost and less restrictive requirements for the main intended use of magnesium as a granular reactant make grinding attractive. For P/M applications the angular morphology of the powder gives good green strength because of mechanical interlocking, but the powder particles are typically covered by a thick surface layer. The layer is hypothesized to contain primarily oxides, but hydroxides, carbonates and hydrates are possible due to long exposure to atmospheric conditions during the grinding process. Recently magnesium powder was also produced commercially by centrifugal inert gas atomization by Tangshan Weihao Magnesium Powder Co. The product has very little surface oxidation due to the inert conditions maintained during production and vacuum during transportation, but the spherical morphology gives poor green strength [23]. No fundamental studies of the sintering behaviour of magnesium powders have been completed to date, but preliminary studies have been reported [23-28].

Another method for disrupting the surface layer is to add a small amount of a more reactive metal. During sintering, the additive reacts with the surface of the surrounding base powder, reducing the oxides of the base to pure metal and forming its own oxide. While the total amount of oxide is still the same, the cohesive layer that was

the barrier to diffusion has been disrupted, providing pathways for unimpeded diffusion. This technique is used successfully in aluminum P/M [29], where a small amount of magnesium results in an increase in density and mechanical properties.

## **1.8 Research Objectives**

The objective of this research is to improve the attractiveness of magnesium through non-traditional processing, by producing magnesium alloys via powder metallurgy utilizing the industrially dominant process of cold die compaction and controlled atmosphere sintering.

The primary goal of this study is to determine if the surface layer is in fact the main obstacle to producing magnesium P/M parts by looking at solid state sintering of pure magnesium powders. The surface layer will be characterized by utilizing surface analysis techniques and microscopy, and the knowledge gained will be utilized to develop methods to disrupt, reduce or remove the layer.

## **CHAPTER 2      EXPERIMENTAL PROCEDURES**

### **2.1      Materials**

The commercially available base magnesium, aluminum, tin and zinc powders were obtained from Ecka Granules. The chemical compositions of the powders are shown in Appendix 1. Elemental magnesium powder of a rounded morphology with an average size of  $\sim 75 \mu\text{m}$  was produced by mechanical grinding, while spherical elemental aluminum powder of an average  $\sim 120 \mu\text{m}$  size, spherical elemental tin powder of an average  $\sim 75 \mu\text{m}$  and irregularly shaped elemental zinc powder of an average  $\sim 36 \mu\text{m}$  size were produced by air atomization. Atomized magnesium was supplied by Tangshan Weihao Magnesium Powder Co, which has an average size of  $38 \mu\text{m}$ , and a composition as shown in Appendix 1. Arcos Organics supplied the calcium granules of approximately 2mm average size and yttrium powder of average size  $44 \mu\text{m}$ , with compositions as shown in Appendix 1. The major impurity in all powders was oxygen. Powders are stored, weighed and mixed in a glove box under an argon atmosphere. Wax lubricant of composition as shown in Appendix 1 was added to reduce die wall friction in some samples compacted by uniaxial compaction.

### **2.2      Powder Characterization**

A Malvern series 2600 droplet and particle laser sizing analyser, with a measurement range of 1 to 1800 microns, was used to determine the particle size distribution of the

powders. A small sample (~ 2g) of the powder to be characterized is mixed with distilled water and added to the input pan of the machine where an impeller insures the powder is suspended. Some of the solution is drawn into the machine and passed by a helium neon laser. The particle size is calculated by diffraction and reported to the computer, which tabulates the result. The machine was factory calibrated and the accuracy was checked by measuring the particle size of a known powder.

Morphology of each powder was checked by mounting a small amount of powder in transoptic mounting media and examining the image under an Olympus model BH-2 optical microscope equipped with a Nikon digital camera.

### **2.3 Powder Blending**

The proper ratio of each elemental powder was measured and combined in a plastic container, along with the appropriate amount of wax lubricant if it is to be used. The powders were blended for 10 minutes in a GlenMills Turbula T2F shaker-blender to ensure a homogenous mixture.

### **2.4 Uni-Axial Die Compaction (UDC)**

The homogenous product of mixing was cold compacted using an Instron Satec Systems Series 5590-HVL uni-axial frame press shown in Figure 2.1 equipped with a floating tool steel die manufactured by Quala-Die to produce rectangular samples

measuring 12.7 mm width by 31.7 mm length having between 8 and 10 mm height. Each sample required 6 g of blended powder.

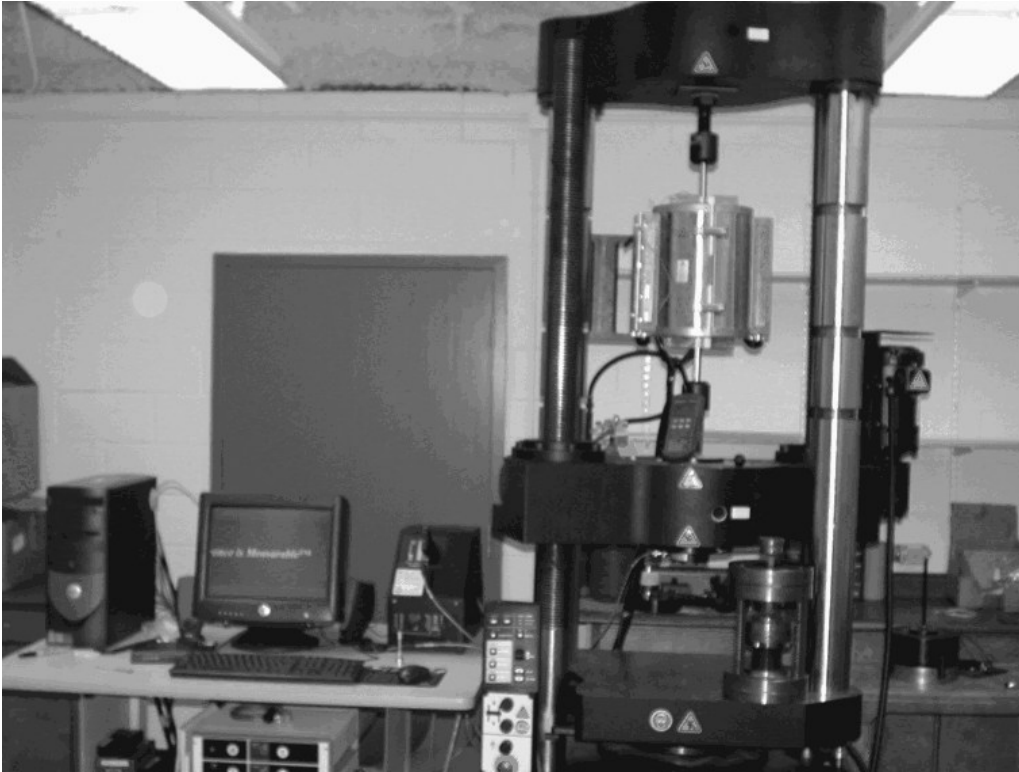


Figure 2.1 - Satec Systems Instron uni-axial press.

The blended powder was loaded into the die once the height was set on the lower punch. The powder bed was leveled and the upper punch inserted into the die. To determine the optimum compaction pressure the samples were pressed at either 300, 400 or 500 MPa.

## **2.5 Cold Isostatic Pressing (CIP)**

For comparison reasons compaction of elemental magnesium powders was also performed for some samples using a Loomis cold isostatic press (CIP). Samples measured approximately 14 mm in diameter and 30 mm length when compacted at 25 ksi (173MPa), which is the maximum capacity of the CIP equipment. Samples produced by either the uni-axial equipment or by CIP are called green samples.

## **2.6 Sintering**

Sintering took place in a Lindberg tube furnace shown in Figure 2.2 which houses a stainless steel tube initially vacuum purged by filling the tube with industrial grade argon and sealing the inlet and outlet. An Edwards mechanical vacuum pump was used to evacuate the tube to a pressure of approximately  $3 \times 10^{-2}$  Torr. The vacuum purging gas refilling process was repeated several times, then the remainder of the sintering process continued under a flowing argon atmosphere of 600 cc/min. The pressed samples were first heated to 360°C and held at this temperature for 30 minutes to vapourize any remaining wax lubricant which was then transported by the flowing argon and condensed at the cold part of the tube furnace. Temperature was measured by an Omega K type thermocouple and controlled by an Omega CN9600 autotune temperature controller. The thermocouple was factory calibrated and its accuracy was checked by measuring the melting point of pure aluminum and sodium chloride.

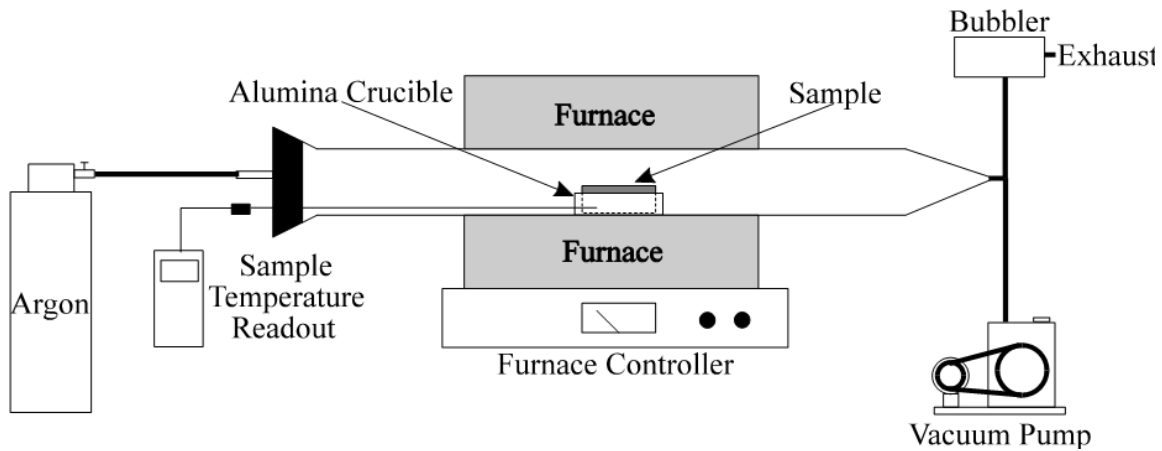


Figure 2.2 - Lindberg tube furnace.

Following de-lubrication, the samples were heated to the required sintering temperature and soaked at the sintering temperature for the required time. After sintering, the furnace elements were turned off and the samples allowed to furnace cool until the desired quench temperature was reached, at which time they were quenched by moving the samples into a water cooled jacket section of the reactor and allowed to cool to room temperature. Some sample were quenched immediately following sintering. An example of a temperature profile showing the heating, pre-sintering, sintering, quenching and cooling cycle is depicted in Figure 2.3.

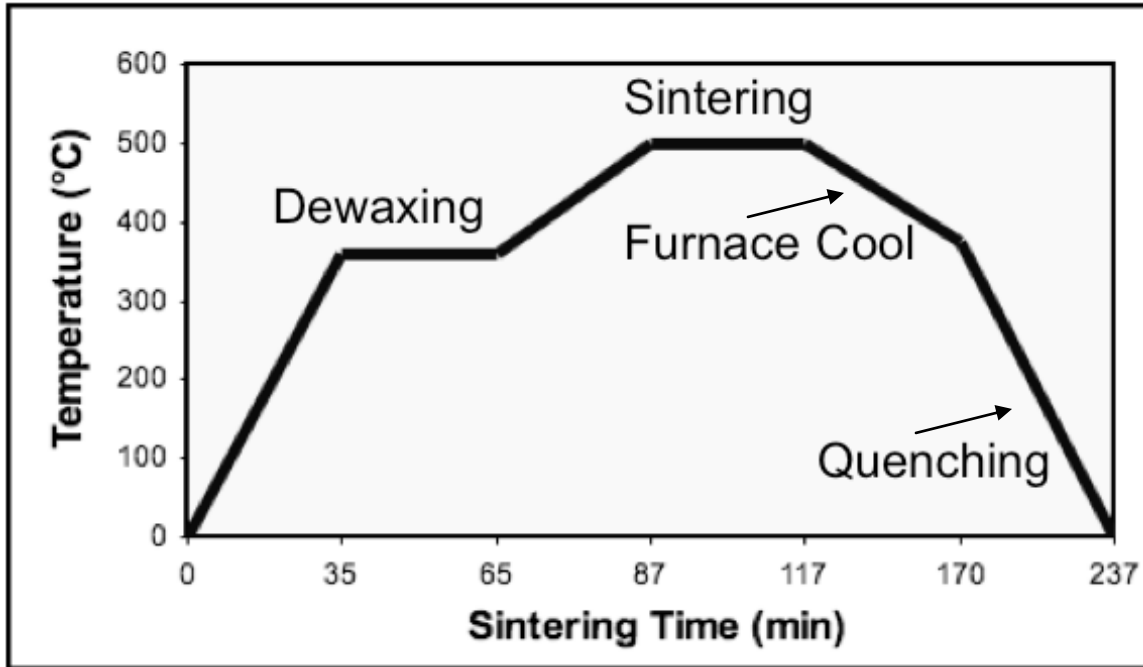


Figure 2.3 - Typical temperature profile of sintering experiment.

## 2.7 Cold and Hot Working

Samples were heated to and maintained at 320°C in a furnace for hot rolling. A four high rolling mill was used to reduce the height of the compacts in increments of 0.127 mm until signs of cracking were apparent. Reduction was calculated as a percentage of the initial to the final height.

## 2.8 Dimensional Change

Each sample was measured based on the width, length and overall area length (OAL) as shown in Figure 2.4. The OAL was measured twice, once at each end, as some

deformation occurs when the samples are compacted. The measurements are recorded after compaction and compared to the measurements after the samples were sintered. The difference between the two results in the dimensional change of the compact. Measurements were completed with a Mastercraft digital slide caliper with a resolution of 0.01mm and accuracy of 0.02mm.

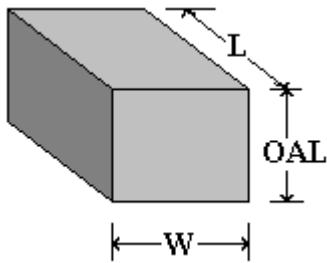


Figure 2.4 - Dimensions of compacted bars.

## 2.9 Density Testing

The density of the material was measured on both the green as well as the sintered products and was determined using the MPIF standard 42 “Density of Compacted or Sintered Powder Metallurgy Products” [30].

This Archimedean method involved weighing the sample in air, then impregnating the sample with a suitable oil (Nuto H 46) by vacuum impregnation. To vacuum impregnate the samples with oil, a vacuum chamber containing a beaker of Nuto H46 was setup. The samples were placed in the oil bath and a vacuum was drawn on the chamber. After the

impregnation process, the samples were re-weighed in a water bath containing the appropriate amount of Kodak PhotoFlo as a wetting agent. The weights of the dried, oil impregnated and suspended in water samples were recorded. The green and sintered densities were measured in g/cc and are reported as percent of the expected theoretical densities. The latter are calculated on the basis of the arithmetic average of the relevant concentrations of the constituents of the alloy [31].

## **2.10 Hardness Testing**

Apparent Rockwell hardness values were obtained to evaluate the success of the powder metallurgy process using a LECO R600. A 1/8" steel ball indenter was forced into the surface using an applied load of 60 kgf. To produce a single data point and in order to assess the error, the overall process was repeated 6 times and the results were averaged.

## **2.11 Tensile Testing**

Tensile samples were pressed using a specially shaped floating tool steel die manufactured by Quala-Die to produce dog bone shaped samples with a gauge length measuring approximately 4 x 5.8 x 90 mm. The Instron Satec Systems Series 5590-HVL uni-axial frame press was used to compact the samples as above. The tensile specimens were then sintered in the tube furnace as described above. Sintered samples were tested for mechanical properties on an Instron tensile test bed equipped with flat clamping jaws. Samples were pulled at a rate of 0.01mm per second until failure. A digital extensometer

connected to a computer was used to collect strain data, which were combined with stress data from the test frame to plot stress/strain curves for each sample.

## **2.12 Microstructure Evaluation and Surface Layer Characterization**

### ***2.12.1 Optical Microscopy (OM)***

Optical micrographs were recorded using an Olympus model BH-2 optical microscope equipped with a Nikon digital camera. The samples were first mounted in transoptic mounting medium, then ground on SiC paper to a 600 grit finish. The samples were then polished using diamond suspensions of 5, 1 and 0.05  $\mu\text{m}$ . Further characterization involved notching and breaking the samples parallel to the direction of compaction.

### ***2.12.2 Scanning Electron Microscopy (SEM)***

A Hitachi S-4700 Field Emission Scanning Electron Microscope (FESEM) operating at 5 kV and a current of 10  $\mu\text{A}$  was used to study the microstructure and phases present in the resulting fracture surface of the samples.

### ***2.12.3 Energy Dispersive Spectroscopy (EDS)***

The FESEM equipped with an INCA EDS was used to determine which elements were present in the samples, and their approximate compositions. The EDS system was operating at 10kV and 10uA using a Si/Li detector.

#### **2.12.4 Transmission Electron Microscopy (TEM)**

TEM specimens were studied at CANMET in Ottawa, Ontario, using a Philips CM20 STEM equipped with an energy dispersive spectroscopy (EDS) apparatus. Various operating conditions were used to highlight different features.

#### **2.12.5 Focused Ion Beam (FIB) System**

Detailed microstructure examination was carried out using a Micrion-2500 FIB located at FIBICS Inc. in Ottawa, Ontario. A large FIB cut was made to allow subsurface microstructure examination. The structure shown by these means is the true structure of the material, as it has not been affected by mechanical polishing or exposure to atmosphere. Various operating conditions were used to highlight different features.

#### **2.12.6 X-ray Photoelectron Spectroscopy (XPS)**

The experiment was performed with a Multilab 2000 XPS system manufactured by Thermo VG Scientific located in the Physics department of Dalhousie. The XPS data were collected with a dual anode X-ray source using magnesium  $K\alpha$  irradiation with an energy of 1253.6 eV. Binding energies were measured using a hemispherical energy analyzer with a fixed pass energy of 50 eV that gives an energy resolution of approximately 1.1 eV. The spectra were collected over a 600  $\mu\text{m}$  in diameter sample area. The data were analyzed using an XPS data analysis software, Avantage, version 3.99

developed by Thermo VG Scientific. Fittings of the peaks were performed using Gaussian-Lorentzian product function and Shirley background subtraction algorithm.

Because the collection area of the XPS is much greater than the area of a single powder particle, the resulting spectra will always contain the contribution of some amount of the surface layer. Figure 1 shows an idealized diagram of the top view, as seen by the XPS, and also the cross sectional view of the sample as etching progresses. As seen in Figure 1a), in the un-etched condition the XPS spectra will reveal only the composition of the surface layer. Once etching begins, some of the magnesium core is exposed, but the XPS spectra are still dominated by the surface layer. In the final stage of etching, the largest portion of the magnesium core is exposed, but there is still a significant contribution from the surface layer. Etching of the samples was considered final when there was no appreciable change in the XPS spectra with further etching.

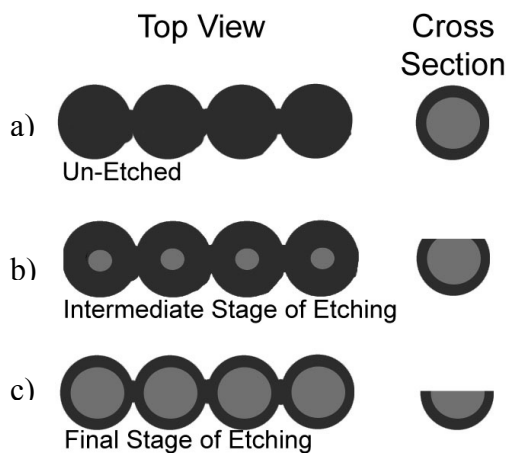


**Fig. 2.5. Geometry of samples during etching. Grey represents the pure magnesium at the particles core, and black represents the surface layer. The un-etched sample is shown in a), an intermediate stage of etching in b), and the final stage in c). Proportions are exaggerated for clarity.**

### **2.12.7 Differential Scanning Calorimetry (DSC)**

DSC tests were completed using a SDT – Q600 DSC manufactured by TA instruments. All specimens were heated at a rate of 10 °C/min under flowing nitrogen (100 ml/min). Standard alumina crucibles for the sample and reference were gold coated by sputtering. The gold coating is less likely to react with magnesium than alumina, as alumina would be reduced by magnesium metal and would destroy the sample and crucible.

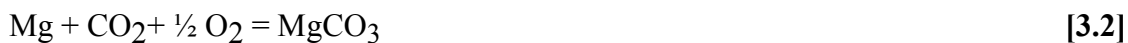
## CHAPTER 3 RESULTS AND DISCUSSION

All electronically collected results are given in Appendix 2 in an open source software format. Appendix 2 is placed in the inside back cover paper version of the thesis.

### 3.1 Fundamental Sintering Studies

#### 3.1.1 *FACTSage Calculations*

There are several possible reactions between magnesium and atmospheric gases that may form compounds found in the surface layer covering magnesium powders. Using FACTSage thermodynamic software, the plausible reactions are:



Of those compounds formed,  $\text{MgCO}_3$  and  $\text{Mg(OH)}_2$  have decomposition reactions that will occur spontaneously below the melting point of magnesium. FACTSage was utilized to estimate the decomposition point:



Reduction to elemental magnesium would be more beneficial, but is not possible below the melting point of magnesium. However, the disruption to the surface layer caused by the decomposition may well expose areas of magnesium below the layer, allowing for better diffusion between adjacent particles during sintering of P/M parts.

### **3.1.2 Metallothermic Reduction of Magnesium Oxide**

In the case of magnesium, the oxide is especially stable and the only option to disrupt the surface layer is the addition of a metal with a more stable oxide. Metals that have an oxide with a lower free energy than MgO and therefore have the ability to disrupt the surface oxide of magnesium are shown in Figure 3.1, which were calculated from tabulated data [32]. Additions of these metals will disrupt the cohesive MgO on the surface of the powder as the oxide of the other metal is formed, allowing unimpeded diffusion and increased interparticle bonding.

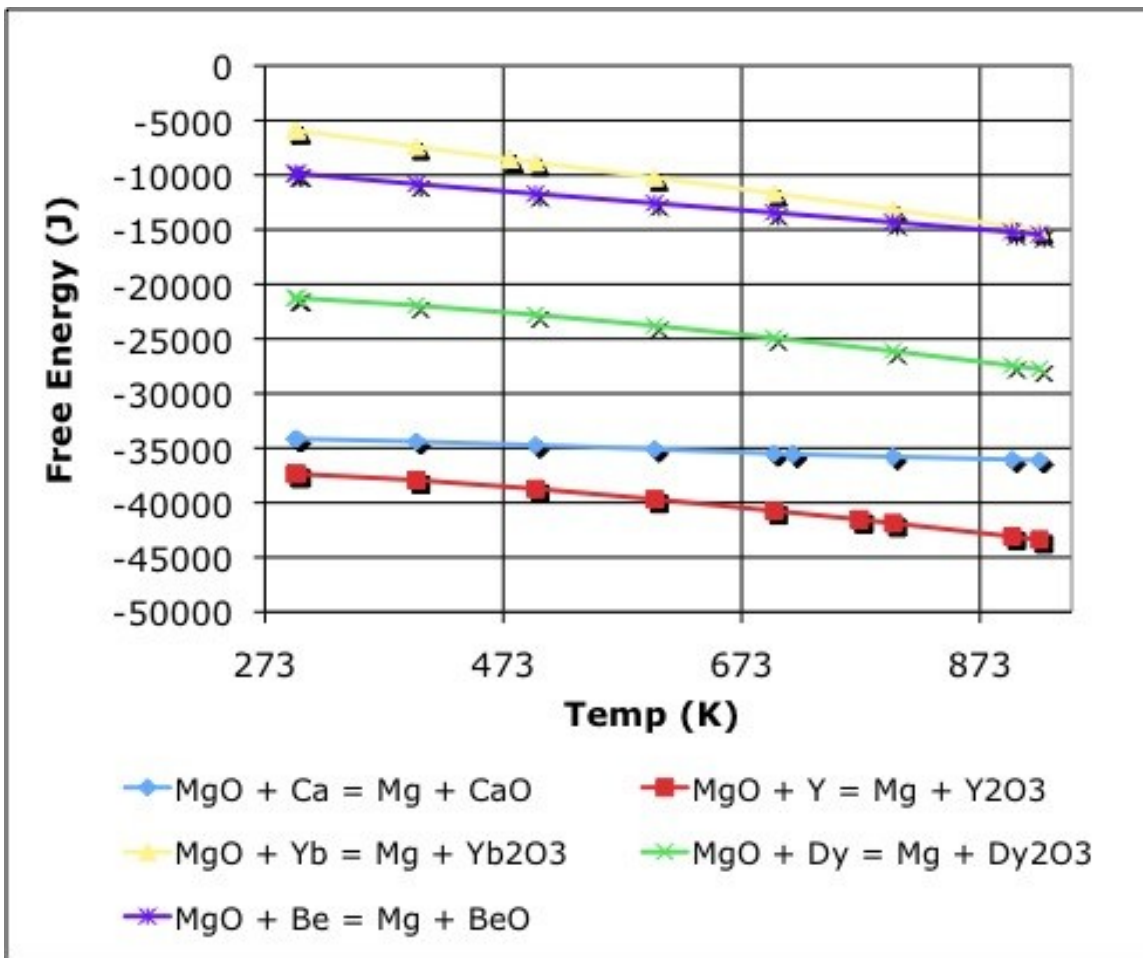
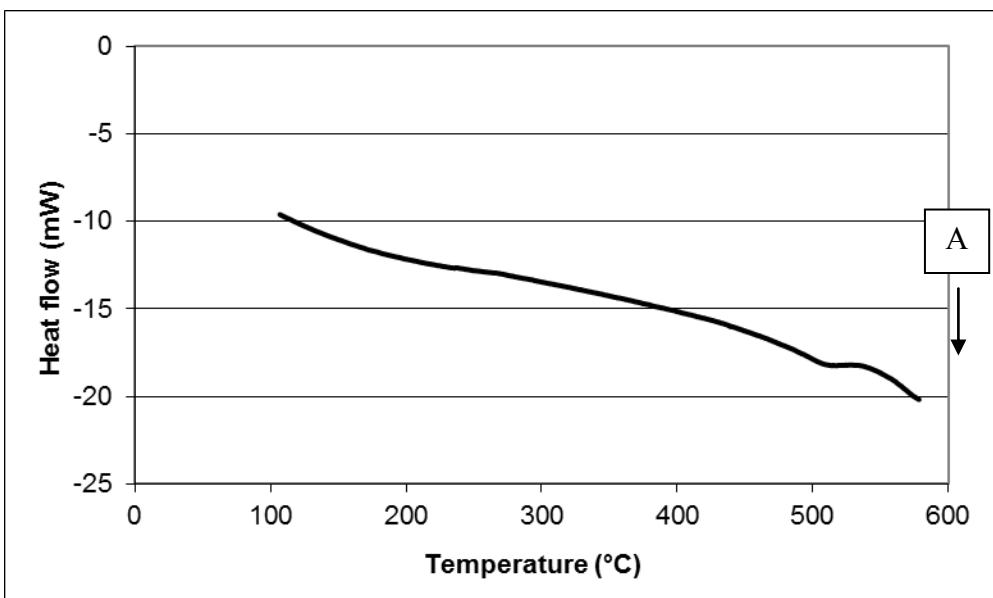


Figure 3.1 - Free energy - temperature diagram showing metals that may reduce MgO.

### 3.1.3 Differential Scanning Calorimetry (DSC)

DSC experiments were completed using gold plated alumina crucibles for the sample and reference. Gold plating was necessary to eliminate reactions between magnesium and alumina. Figure 3.2 shows the DSC trace of two empty gold plated crucibles used as a baseline for further experiments. No reactions are present until above 500 °C, where a small exothermic peak is found at (A).



**Figure 3.2 - DSC trace of two empty gold plated crucibles. Area (A) represents reactions between crucible and Au.**

### 3.1.3.1 Pure Magnesium

The DSC trace of pure magnesium powder is shown in Figure 3.3. Area (A) shows a small exothermic peak at 280 °C, which co-insides with the FACTSage estimated decomposition of  $\text{Mg}(\text{OH})_2$ . Area (B) shows an exothermic peak beginning at ~450 °C, below the estimated decomposition temperature of  $\text{MgCO}_3$ . It is possible some of the  $\text{MgCO}_3$  is in a hydrated form, which will begin decomposing at lower temperatures [32]. Area (C) at ~520 °C corresponds to the decomposition of the carbonate. After these decomposition reactions, the surface layer is disrupted enough that the nitrogen from the atmosphere can react with pure magnesium, forming  $\text{Mg}_3\text{N}_2$ , which is shown at (D).

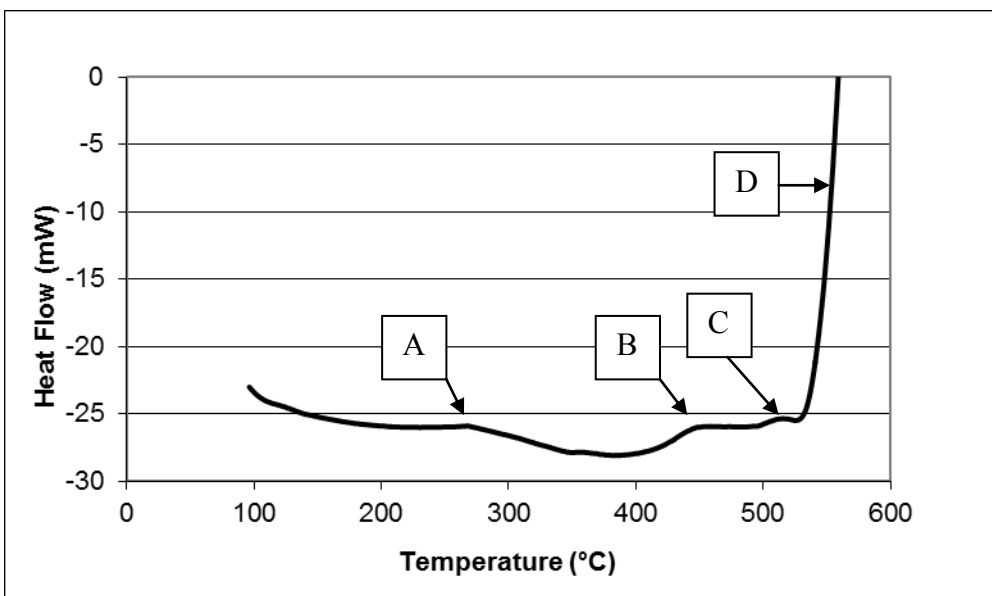


**Figure 3.3 – DSC trace of pure magnesium powder heated from ambient to 600°C at 10°C/min. Area (A) represents hydroxide decomposition, area (B) hydrated carbonate decomposition. Area (C) is carbonate decomposition and (D) is formation of  $\text{Mg}_3\text{N}_2$ .**

Figure 3.4 shows the change in mass of the pure magnesium sample as it is heated to 600 °C. A small weight loss is apparent beginning at 280 °C which corresponds to the loss of water vapour from the hydroxide decomposition. After the small initial loss, and the exposure of pure magnesium as the surface layer is disrupted, and the mass increases as magnesium nitride forms. Figure 3.4 is scaled to show the small mass loss at 280 °C and the total gain is not shown, but the maximum mass attained at 600 °C was 223 mg.

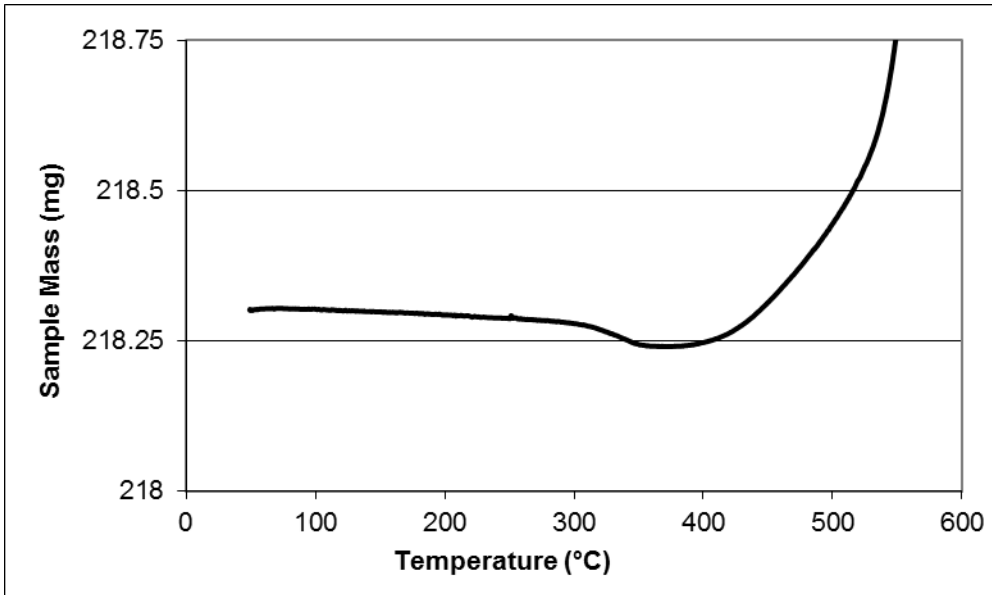


**Figure 3.4 - Mass change of pure magnesium sample while heating to 600°C.**

**Maximum mass was 223 mg at 600°C.**

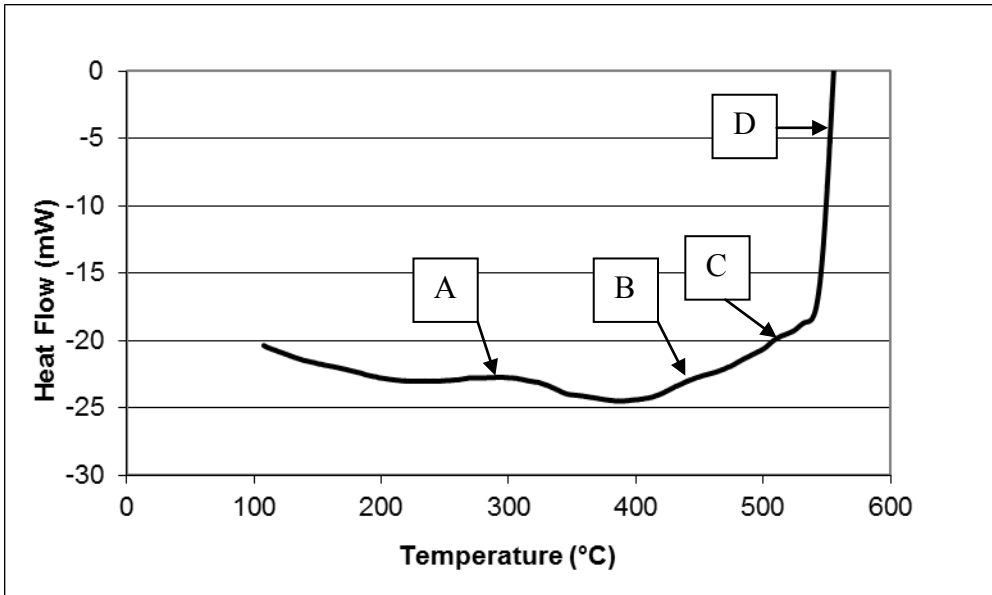
### 3.1.3.2 Magnesium + 1wt% Calcium

Figure 3.5 shows the DSC trace of magnesium with a 1wt% addition of calcium. The presence of calcium, which is a more reactive metal than magnesium, disrupts the magnesium surface layer through the following reactions:



In this case, not only does the reaction disrupt the cohesiveness of the surface layer, but the product is elemental magnesium. The total amount of impurity does stay the same as now calcium is taking the place of magnesium with the impurities. Since these reactions are spontaneous at any temperature, they are controlled by kinetics and more difficult to estimate.

Area (A) at  $\sim 280$  °C indicates the hydroxide decomposition, but the peak is extended compared to the pure magnesium samples. This may be the conversion of  $\text{Mg}(\text{OH})_2$  to  $\text{Ca}(\text{OH})_2$ . The decomposition reaction for calcium hydroxide is possible below the melting temperature, but at a relatively high temperature of  $516^\circ\text{C}$ . Area (A) may also include the possible magnesium to calcium carbonate reaction at roughly  $310^\circ\text{C}$ . Area (B) corresponds to the lowest melting Mg-Ca eutectic at  $445^\circ\text{C}$ , but the endothermic melting may be masked by the exothermic decomposition of the hydrated carbonate. Beyond that temperature, there is another Mg-Ca eutectic at  $516^\circ\text{C}$  and also the carbonate decomposition is possible. The larger exothermic heat flow at area (D) again indicates the nitride formation. Figure 3.6 shows the mass change while heating, and the result is similar to the pure magnesium case. The maximum mass attained is less however, at 217 mg. This may be due to liquid phases shielding the pure magnesium from contact with the nitrogen atmosphere.



**Figure 3.5 - DSC trace of magnesium with 1wt% calcium heated from ambient to 600 °C at 10 °C/min. Area (A) represents hydroxide decomposition, area (B) hydrated carbonate decomposition. Area (C) is the carbonate decomposition and area (D) is formation of  $Mg_3N_2$ .**

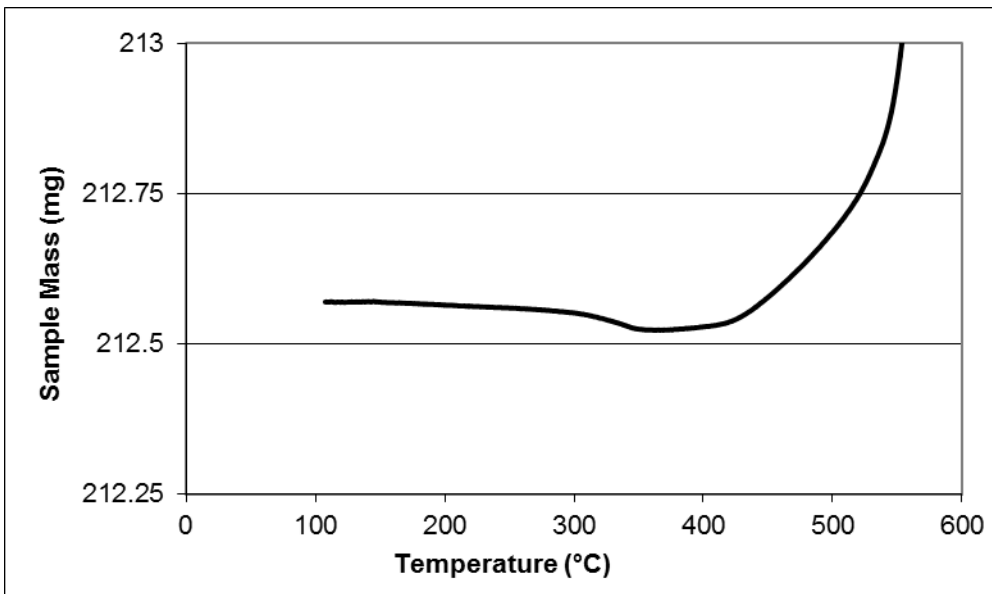
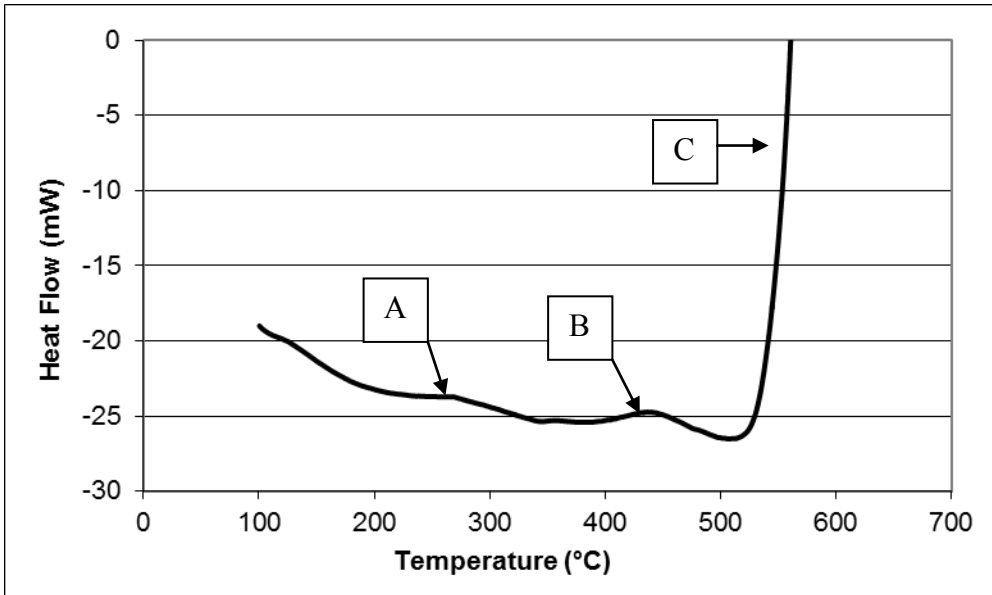


**Figure 3.6 - Mass change of Mg-1wt% Ca sample while heating to 600°C. Maximum mass was 217 mg at 600°C.**

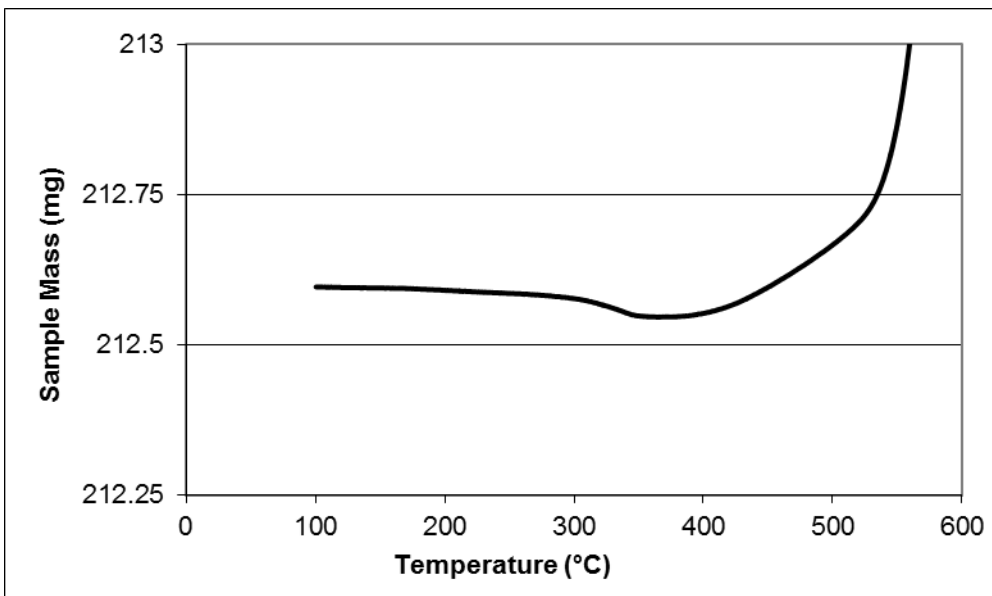
### 3.1.3.3 Magnesium + 2wt% Yttrium

Figure 3.7 shows the DSC trace of a mixture of pure magnesium with 2wt% yttrium. The Mg-O<sub>2</sub>-H<sub>2</sub>O-CO<sub>2</sub>-Y system is different from the calcium system because yttrium is more reactive than calcium, and also it has the ability to decompose only the oxide of magnesium, but not the hydroxide or carbonate. Yttrium also forms a nitride that is more stable than magnesium nitride.

Examining Figure 3.7 there are the same peaks at area (A) and (B) representing the decomposition of the hydroxide and hydrated carbonate, respectively, which are found in the pure magnesium and Mg-1wt% Ca cases. Because the nitride of yttrium is more stable than that of magnesium, the peak at (C) begins at a lower temperature and masks the decomposition of the carbonate. Figure 3.8 shows the change in mass on heating, and is similar to the pure magnesium and Mg-1wt% Ca case with the exception of the nitride formation beginning at a lower temperature. The maximum mass gained was also higher than previous samples, at 226 mg, indicating more mass was gained due to the formation of YN along with Mg<sub>3</sub>N<sub>2</sub>.



**Figure 3.7 - DSC trace of magnesium with 2wt% yttrium heated from ambient to 600°C at 10°C/min. Area (A) represents hydroxide decomposition, area (B) hydrated carbonate decomposition. Area (C) is the formation of YN.**



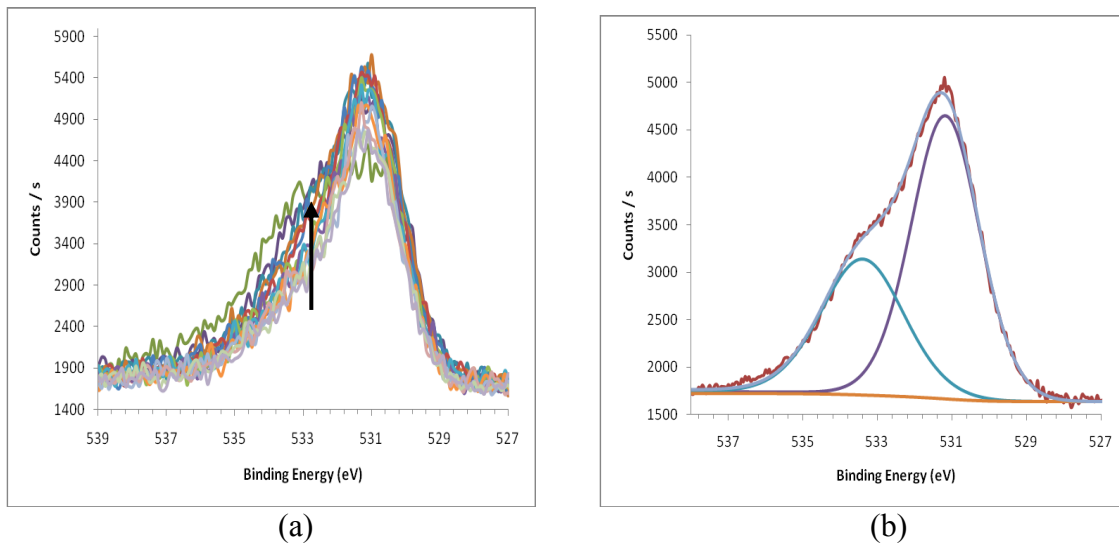
**Figure 3.8 - Mass change of Mg-2Y sample while heating to 600°C. Maximum mass was 226 mg at 600°C.**

### 3.1.4 Surface Layer Characterization

#### 3.1.4.1 X-ray Photoelectron Spectroscopy (XPS)

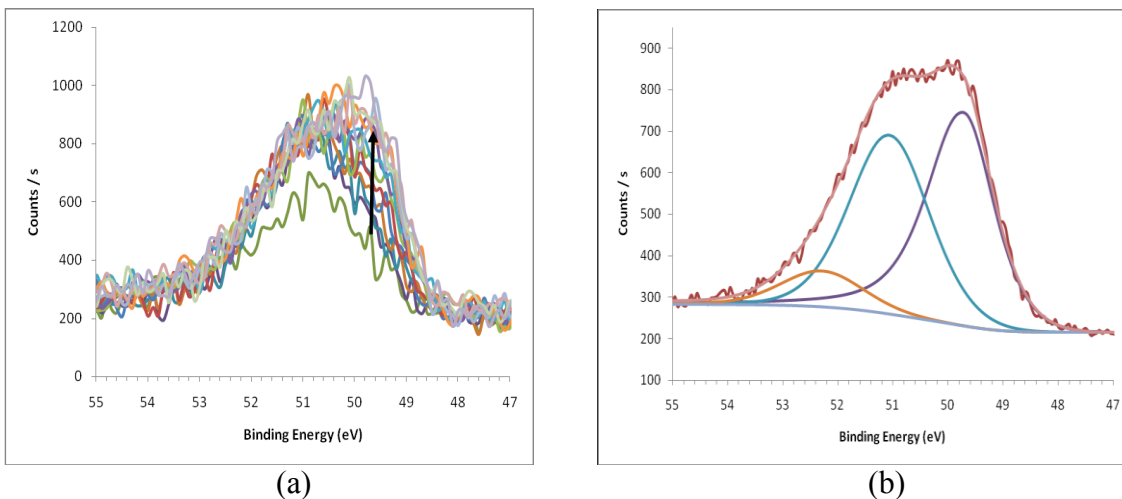
##### 3.1.4.1.1 Green (Unsintered) Magnesium

Figure 3.9a shows the spectra of O 1s peak of the sample Mg green while the etching was performed. As etching progresses O 1s peak showed a developing shoulder-like feature around 533.2 eV. Also both the developing peak and the peak already formed around 531.1 eV grew larger as the etching depth increased, and finally reached a shape that did not change as etching time progressed further. Figure 3.9b shows the high resolution spectra of O 1s peak of sample Mg green. Deconvolution of the spectra using two peaks gave a reasonable fitting. One is located at 531.1 eV and the other one is located at 533.2 eV. The peak located around 531.3 eV can be assigned as MgO peak, and the peak located about 533.3 eV can be assigned as MgCO<sub>3</sub> or Mg(OH)<sub>2</sub> peaks [33-35].



**Figure 3.9 - The XPS spectra of O 1s peak of Mg green sample : (a) etching, (b) high resolution**

Mg 2p spectra of sample magnesium green are shown in Figure 3.10a. The Mg 2p peak of the sample showed an increase in peak size and a broadening in shape as etching time progressed. It can be seen that the spectra show the tips of two peaks and asymmetry on the higher binding energy side. By taking into account these considerations one could decompose the spectrum with three peaks to obtain a reasonable fitting, and it gives the following binding energy values for the spectrum: 49.7 eV, 51.1 eV, and 52.3 eV. The peak of 49.7 eV can be labeled as magnesium [33-35], the peak of 51.1 eV can be labeled as MgO and/or Mg(OH)<sub>2</sub> and the peak of 52.3 can be labeled as MgCO<sub>3</sub> peaks. The development of the peak during etching indicates the outer portion of the surface layer consists of MgCO<sub>3</sub>, Mg(OH)<sub>2</sub> and MgO and as etching continues through the layer and into the core of the powder particle, the composition is primarily magnesium with some MgO. The MgO found at this stage is likely due to the geometry of the sample, as outlined in Fig. 2.5, and not due to any appreciable amount of MgO contamination in the core of the powder itself.



**Figure 3.10 - The XPS spectra of Mg 2p peak of Mg green sample : (a) etching, (b) high resolution**

The Mg green sample showed a strong C 1s peak and this peak is also increased as a function of etching time until reaching the maturity level. Figure 3.11 shows high resolution spectrum of the C 1s peak. It is clear that the peak is showing a broadening on the higher binding energy side. Using two peaks to deconvolute the spectrum gave a reasonable fitting of 284.8 eV and 286.7 eV, corresponding to  $\text{MgCO}_3$  and a small amount of some other complex hydrate, possibly  $\text{MgCO}_3 \cdot (\text{H}_2\text{O})_3$ , respectively. The presence of hydrates of the hydroxides and carbonates will slow any decomposition reactions as the water of hydration must be evaporated first.

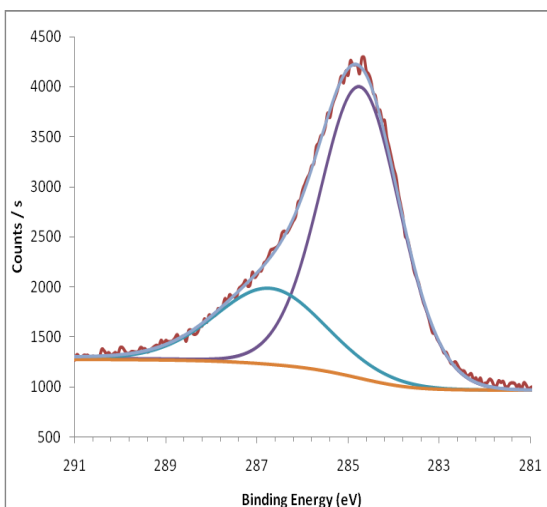


**Figure 3.11 - The high resolution spectra of C 1s peak of sample Mg green after etching.**

#### *3.1.4.1.2 Sintered Magnesium*

Figure 3.12 shows how the O 1s peak of sintered magnesium behaves as a function of etching. Figure 3.12a is part of the etching during which appearance and growth of a peak around 531.3 eV becomes clear and the existing peak at about 533.3 eV shows growth. Figure 3.12b is the spectrum of subsequent etching of the same O 1s peak, during this etching time the spectrum showed decrease on the peak located around 533.3 eV and increase around 531.3 eV. Further etching of O1s peak did not yield any change in the shape of the spectra. The peak located at 531.1 eV can be labeled as MgO peak and the peak of 533.2 eV can be labeled as MgCO<sub>3</sub> and/or Mg(OH)<sub>2</sub> peak. This sample showed C 1s peak before the etching is performed. After the etching C 1s peak was almost gone. It suggests that the peak is more likely due to Mg(OH)<sub>2</sub>. Figure 3.12b

implies that as etching proceeds the data are collected more from the bulk and the  $\text{Mg}(\text{OH})_2$  portion of the sample gets smaller gradually.

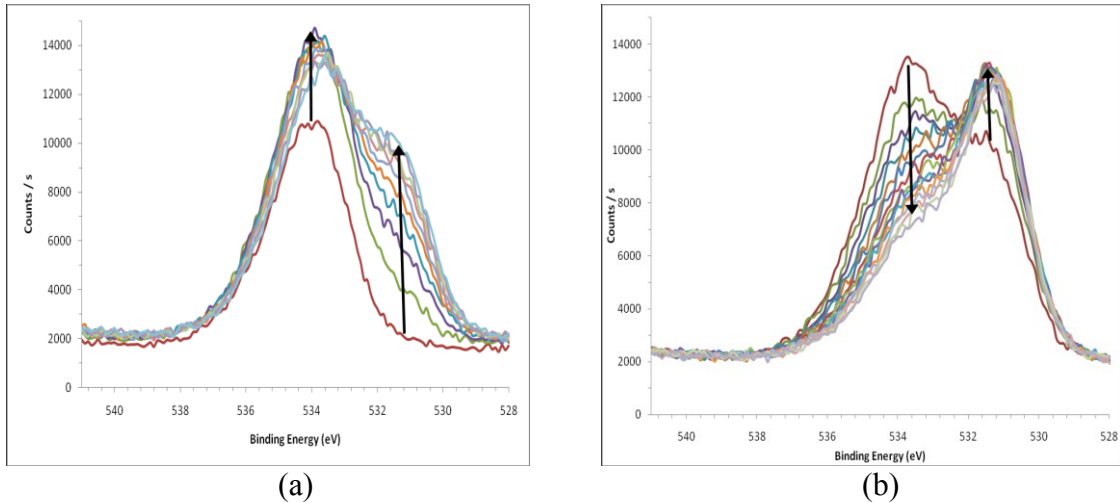


**Figure 3.12 - The XPS spectra of O 1s peak of the Mg-sintered sample as a function of etching: (a) both peaks are getting bigger (b) subsequent continuation of etching showing decrease on higher binding energy peak.**

The high resolution spectrum of O 1s of Mg-sintered sample after etching is shown in Figure 3.13. It is possible to deconvolute the spectrum by the placement of two peaks located at 531.3 eV and 533.3 eV. MgO would contribute to 531.3 eV peak and  $\text{Mg}(\text{OH})_2$  would contribute to the 533.3 eV peak.

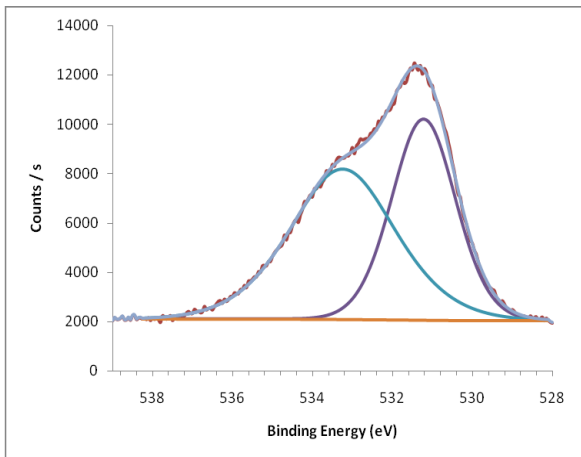


**Figure 3.13 - The high resolution spectra of O 1s peak of sample Mg sintered.**

Initial and following etching of Mg 2p peak of Mg-sintered sample is shown in Figure 3.14. Initially the peak showed one noticeable peak about 52 eV and as the etching continued it showed change in size and shape. It is clear in the subsequent etching spectrum of Mg 2p in Figure 3.10b, that there is an appearance of a shoulder on the lower binding energy side located at about 50 eV.

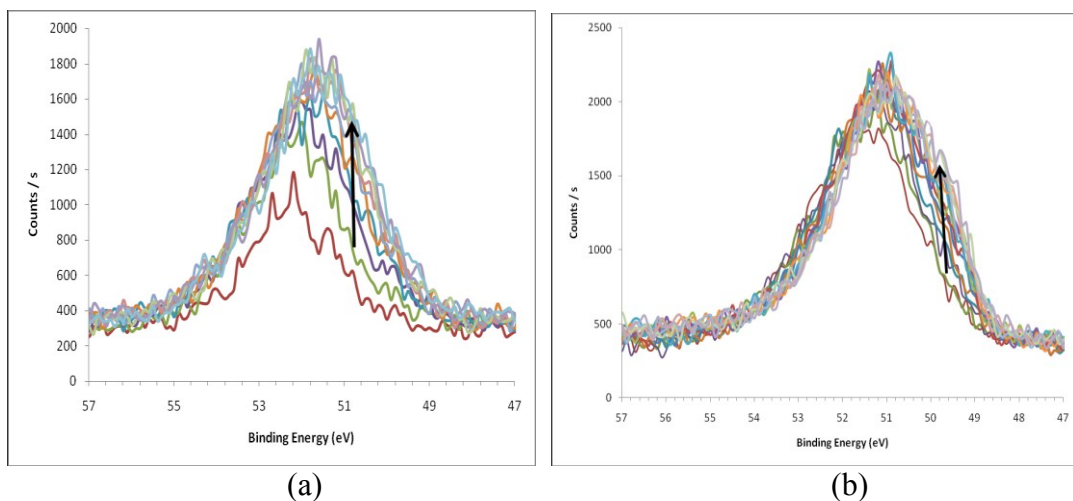


**Figure 3.14 - (a) The XPS spectra of Mg 2p peak of the Mg-sintered sample as a function of etching, (b) subsequent continuation of the etching.**

The after etching high resolution spectrum of Mg 2p of the Mg sintered sample with two peaks gave a reasonable fitting, as shown in Figure 3.15. The fitting peaks are located at 50.0 eV and 51.3 eV. The peak around 50.0 eV can be assigned as magnesium. The peak about 51.3 eV could be from MgO, Mg(OH)<sub>2</sub>, MgCO<sub>3</sub> or a combination of any of these compounds. Figure 3.15 shows that the peak of 51.3 eV is much bigger than that of 50.0 eV. The Mg sintered sample shows a very small peak of C, that suggests a contribution to the peak of 51.3 eV would be mostly from MgO or Mg(OH)<sub>2</sub>.

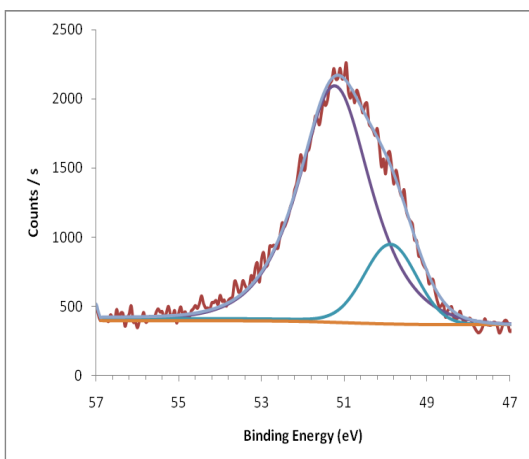


**Figure 3.15 - The high resolution spectrum of Mg 2p peak of sintered Mg.**

#### *3.1.4.1.3 Comparison of Green and Sintered Samples*

For comparison purposes, after etching O 1s peaks of Mg green and Mg sintered are shown together in Figure 3.16 in normalized scale. The deconvolution of these spectra were shown in Figures 3.9 and 3.13 and the corresponding binding energies are tabulated in Table 3.1.

The Mg 2p peak of sample Mg green and sample Mg sintered are shown together in Figure 3.17 for comparison. Deconvolution of these spectra are shown in Figure 3.10 for Mg green and in Figure 3.15 for Mg sintered, and the binding energy values of fitting peaks of Mg green and Mg sintered samples are tabulated in Table 3.2.

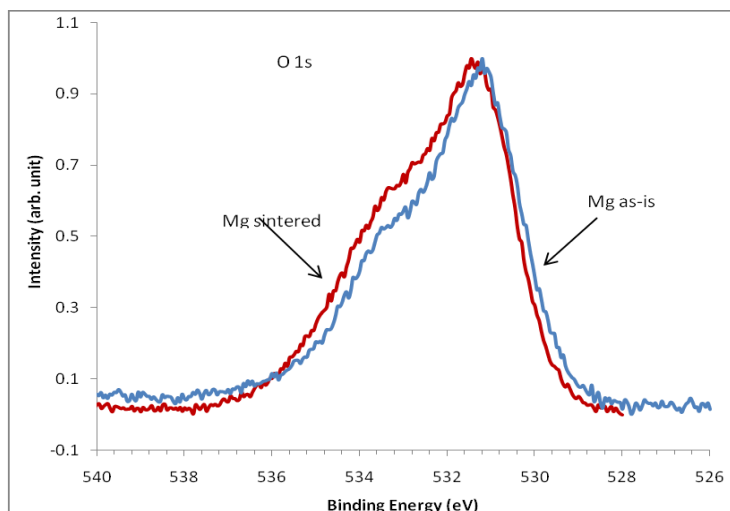


**Figure 3.16 - O 1s peak comparison of Mg green and Mg sintered samples after etching.**

**Table 3.1 - The binding energies of fitting peaks for O 1s peaks of sample Mg green and Mg sintered.**

Sample Name	Peak	Compound
Mg green	531.1	MgO
	533.2	Mg(OH) <sub>2</sub>
Mg sintered	531.3	MgO
	533.3	Mg(OH) <sub>2</sub> and/or MgCO <sub>3</sub>

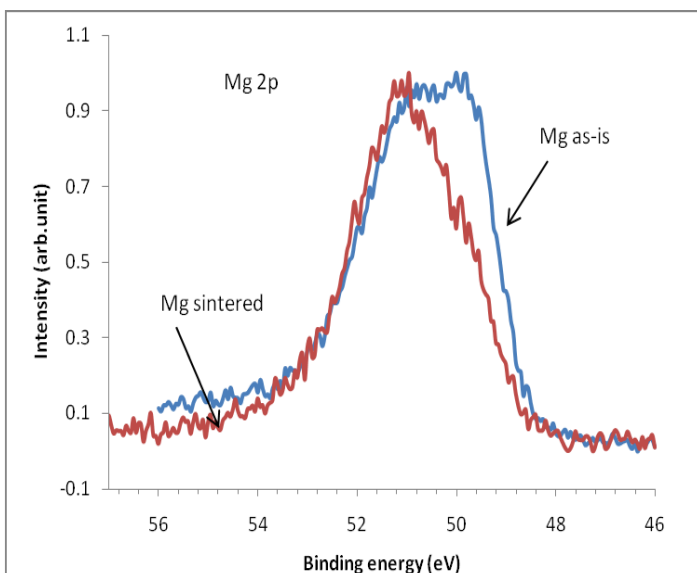


**Figure 3.17 - Comparison of Mg 2p peaks of Mg green and Mg-sintered samples after etching.**

**Table 3.2 - The binding energies for Mg 2p peaks of fitting peaks of sample Mg green and Mg sintered.**

Sample Name	Fit Peaks (eV)	Compound
Mg green	49.7	Mg
	51.1	MgO, Mg(OH) <sub>2</sub>
	52.3	MgCO <sub>3</sub>
Mg sintered	50.0	Mg
	51.3	MgO, Mg(OH) <sub>2</sub>

To compare, the Mg 2p spectra of Mg green and Mg sintered samples are shown in Figure 3.18 at normalized scale. It can be seen that the MgO peak of the sample Mg sintered is considerably bigger than the magnesium peak. It suggests that more oxidation occurred for the Mg sintered sample compared to Mg green sample. At the sintering temperature of 600°C, both Mg(OH)<sub>2</sub> and MgCO<sub>3</sub> will decompose into MgO and gases, which explains the increase in MgO from the green to the sintered sample. The high resolution spectra of Mg green yielded a peak at 52.3 eV, see Figure 3.11, and assigned as 2p peak of MgCO<sub>3</sub>. This assertion can be supported due to the existence of C 1s peak even after etching of the Mg green sample. The normalized survey spectra of the both samples are shown in Figure 3.18 in normalized scale. The spectrum of Mg green sample has been shifted upward to make the comparison clearer. The fact that Mg sintered sample has much more smaller C 1s peak suggests that keeping the sample at 600°C during the sintering process helped removing C atoms from the Mg sample. It is understandable because MgCO<sub>3</sub> bonding can be broken by thermal energy above 520°C, as shown in Section 3.1.1. The decrease in Mg(OH)<sub>2</sub> is more difficult to confirm because XPS is not able to resolve hydrogen [35], but the decomposition temperature of only 280°C suggests a similar mechanism to MgCO<sub>3</sub>.

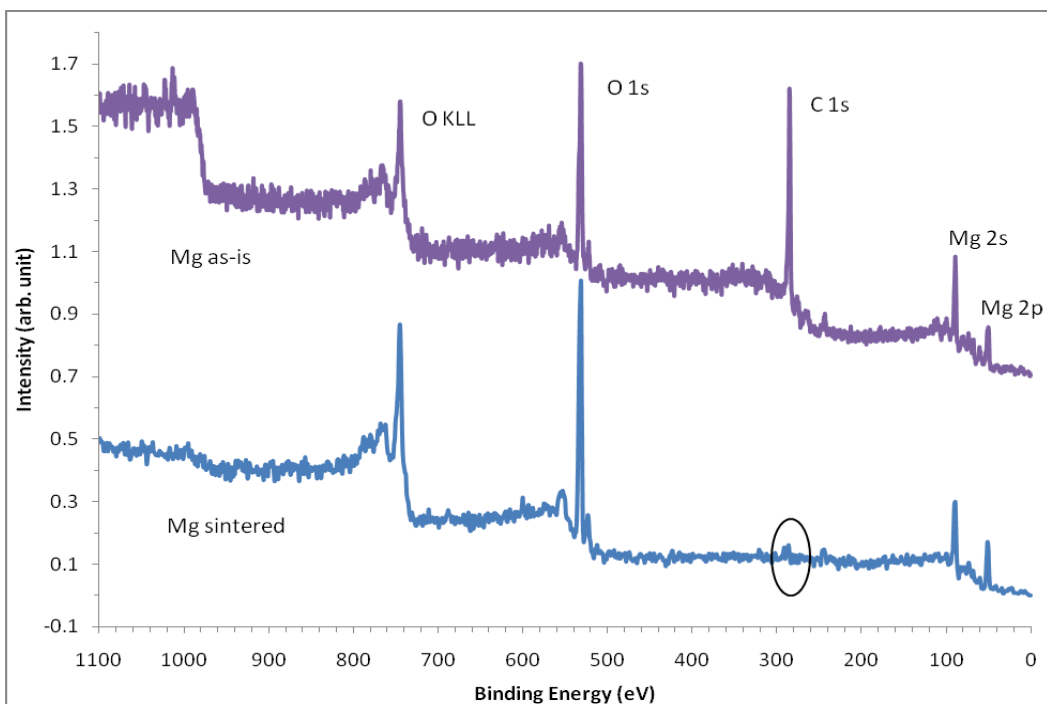


**Figure 3.18 - Comparison of survey spectra of Mg green and Mg sintered samples after etching.**

Despite the large area of investigation of XPS, which includes both native magnesium and the surface layer, the technique was able to determine for the first time the presence of carbon as well as oxygen in the surface layer. Furthermore, although hydrogen cannot be resolved itself with XPS, it was shown with good agreement that the compounds present must contain hydrogen. All previous work has been based on the assumption that the layer was comprised of only oxides. This new finding allows for new avenues of surface layer disruption to be explored.

However, since XPS had reached its limitations a new technique was needed to allow the investigation of the layer alone. This would allow for more accurate

compositional analysis as well as direct measurement of the thickness of the layer. FIB-TEM was chosen for this work and it was applied for the first time in this area of study.

#### 3.1.4.2 Scanning Electron Microscopy (SEM)

SEM was used in conjunction with EDS to determine the composition of various features in a sample of magnesium alloy containing 1wt% calcium. Figure 3.19 shows the high magnification image and EDS spectra from three areas of interest. The first area, (A), is the matrix magnesium, shown to be pure magnesium in spectrum (A). The grain boundaries (B) are primarily magnesium with calcium present as well as oxygen. The EDS is not able to accurately determine compounds, but these areas could be  $Mg_2Ca$  intermetallics and  $MgO - CaO$ , or a complex oxide of both magnesium and calcium. The discrete particles found at (C) contain a large amount of oxygen and are likely formed by the reaction between  $MgO$  and calcium.

Figure 3.20 shows the EDS maps of the elements magnesium, oxygen and calcium. Oxygen is concentrated at the discrete particles, which are magnesium deficient. Calcium has diffused equally throughout the matrix, and is also present in the discrete particles. This points to the discrete particles being  $CaO$ .

Backscattered electron image shows that cell boundaries appear lighter. Substrate contains pure magnesium as indicated in spectrum (A), correspond to location (A) in the SEM image. The bright cell boundaries are mostly calcium-rich phase as identified at

location (B). Large clusters of particles location (C) appear to contain large amount of oxygen.

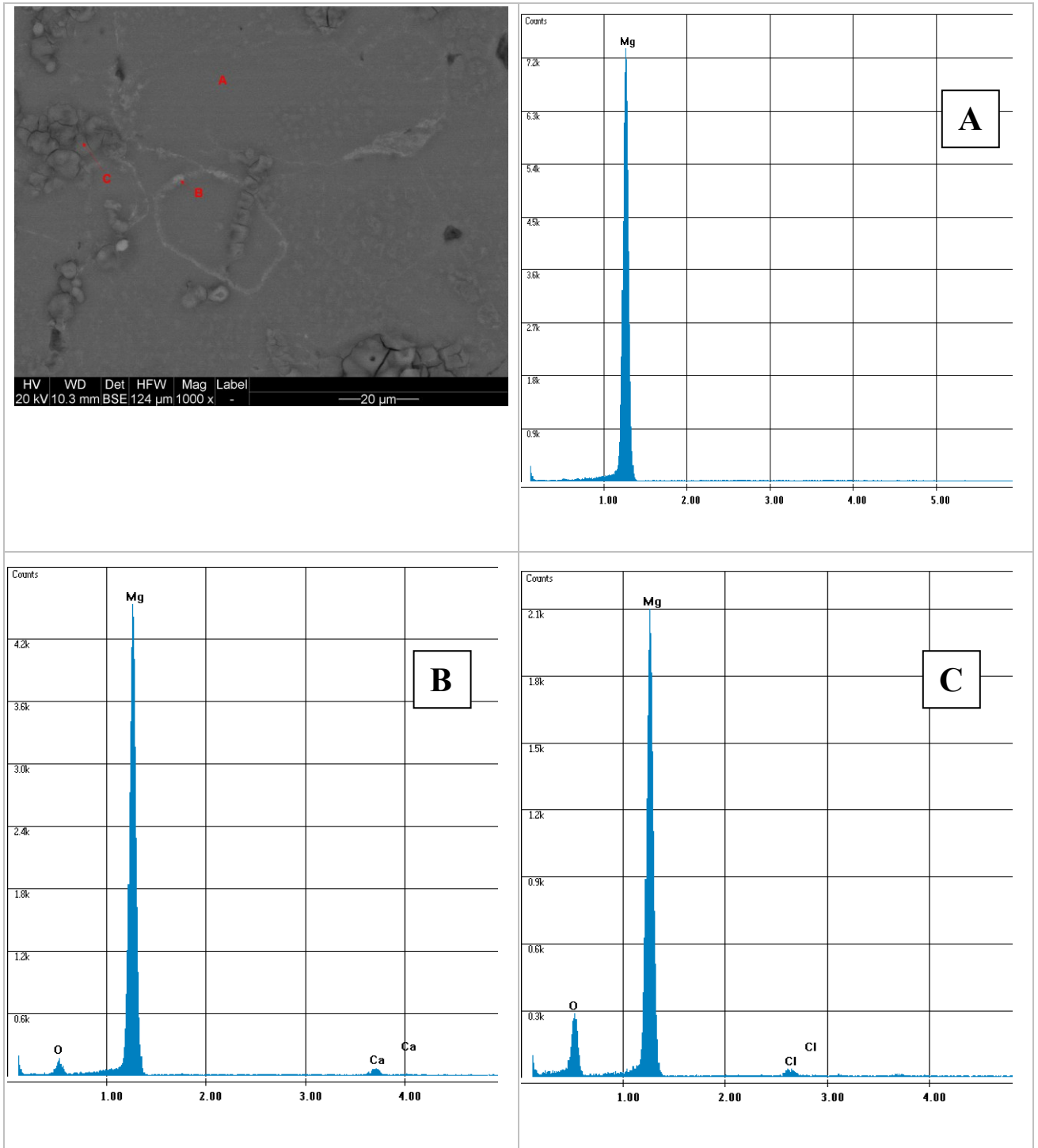
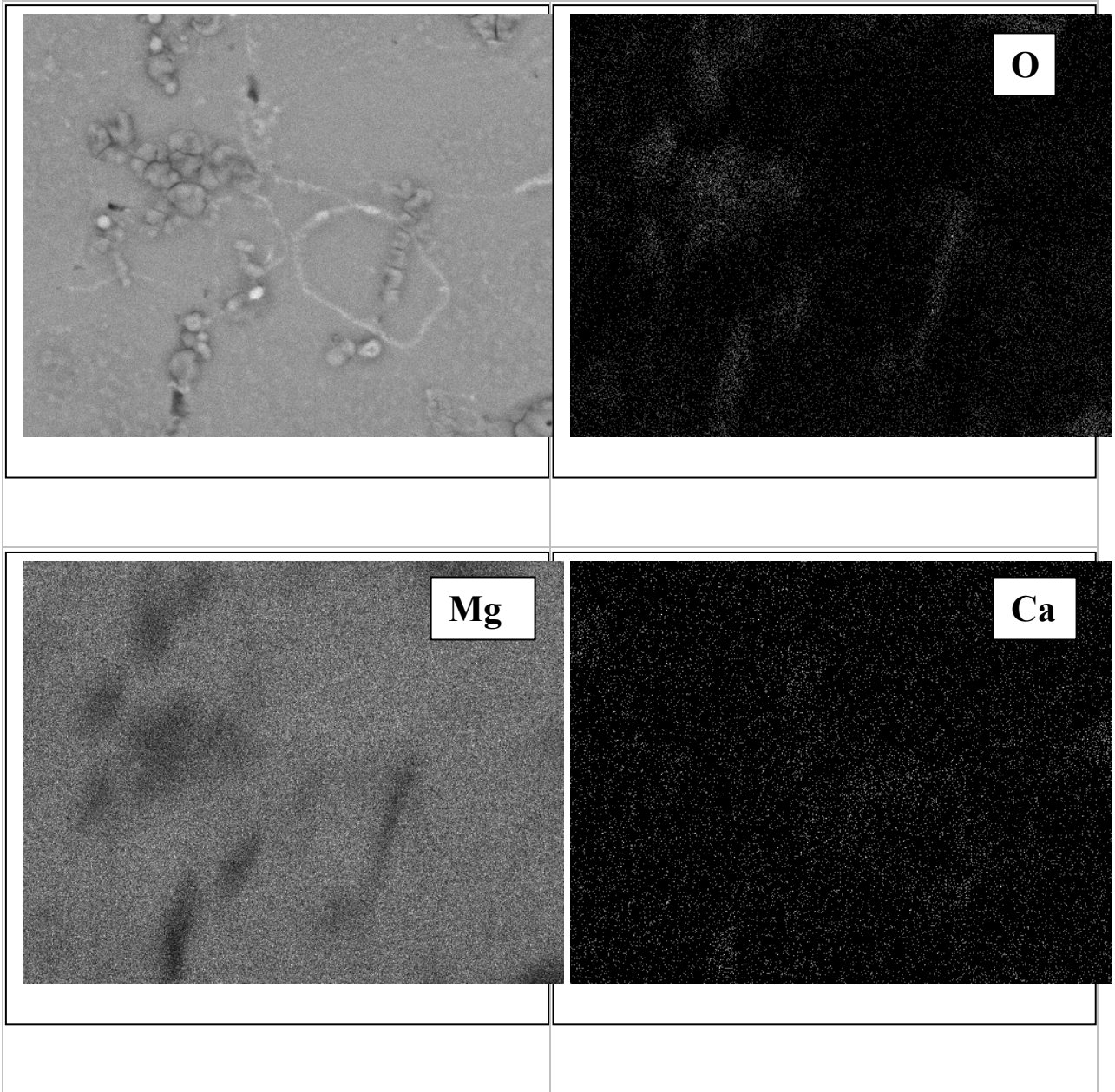


Figure 3.19 - SEM image and EDS spectra taken from Mg-1%Ca sample.



**Figure 3.20 - Secondary electron SEM image and corresponding EDS maps showing distribution of Mg, O and Ca.**

### 3.1.4.3 Focused Ion Beam (FIB)

The FIB was used both to prepare thin film samples for TEM analysis and to capture high resolution images itself, and preliminary results from this study have been published [24]. Imaging with the FIB has the benefit of in-situ cross sectioning, not requiring any external polishing of the sample which may disrupt the true surface or transfer to other imaging equipment allowing surface contamination.

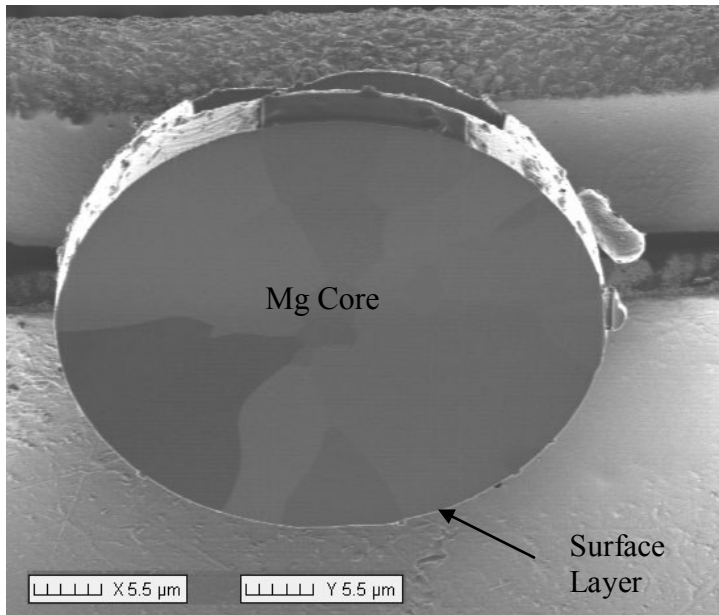


**Fig. 3.21. Focused ion beam image of the cross section of a single Mg powder particle. Note the surface layer (thin white layer) enveloping the Mg core.**

Figure 3.21 shows a focused ion beam micrograph of the cross section of a single magnesium powder particle. At the center of the particle is the polycrystalline magnesium core, and the particle is surrounded by a thin surface layer. It can be seen that

the surface layer is of a constant thickness around the circumference of the particle. Visual measurement of the layer gives a thickness of ~10nm.

Figure 3.22 is a sintered magnesium alloy containing 1wt% calcium. The cross section shown was prepared by removing a wedge shaped trench in front of the section. The thick layer at the surface is deposited tungsten used to protect the underlying surface layer during milling. The microstructure shows good sintering with excellent interparticle bonding and no evidence of the previous boundaries between the original powder particles. The grain boundaries feature a high concentration of calcium, possibly in the form of the intermetallic  $Mg_2Ca$ . Porosity is present at intersections of multiple grains, and may also be caused by the site occupied previously by a calcium particle.

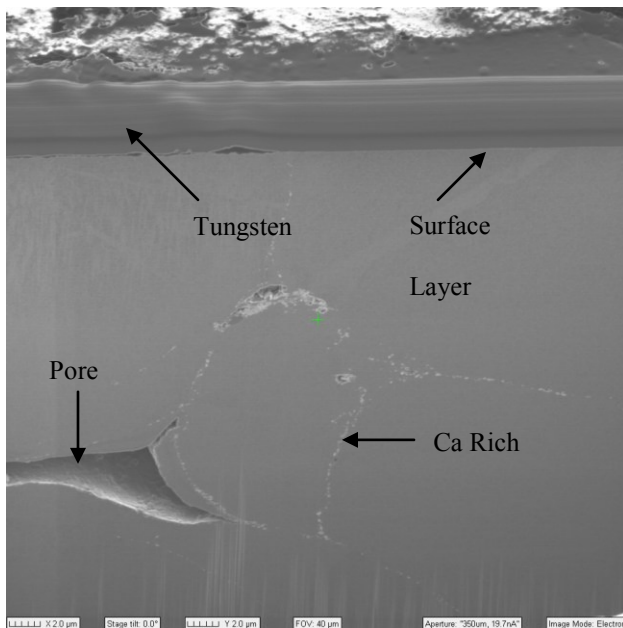


**Figure 3.22 – Mg with 1 wt% Ca. Surface layer has been protected with deposited tungsten. Light areas at grain boundaries are Ca rich.**

#### 3.1.4.4 Transmission Electron Microscopy (TEM)

Thin foils of pure magnesium powder were examined in the TEM to visually determine the thickness of the surface layer formed on powders exposed to atmosphere for various lengths of time. Table 3.3 shows the thickness of the as received powder, and of samples after 24 and 72 hour exposure. The surface layer of magnesium, which is comprised of the oxide, hydroxide and carbonate of magnesium, is not stable and the thickness increases with increased exposure time. Therefore it is important to limit open air processing and work under controlled atmosphere as much as possible.

**Table 3.3 - Thickness of surface layer formed on pure Mg particle due to exposure to atmosphere for various times.**

	As Received	24 hour	72 hour
Thickness (nm)	14.6	30.3	85.3

A TEM micrograph of the as received magnesium powder is shown in Figure 3.23. The samples were coated with gold to prevent charging and coated with tungsten to protect the surface layer from beam damage during FIB milling. The surface layer shows as a lighter colour. Table 3.4 shows the change of composition of the layer, by EDS line scan, starting in the coating then extending through the layer and into the bulk of the particle. The gold coating is constrained to the exterior portion of the layer, but there is some tungsten contamination extending through to the bulk. Carbon, in the form of

MgCO<sub>3</sub> is found only on the exterior of the layer and oxygen in the form MgO is found primarily on the interior of the layer. These results coincide with the data found with XPS.

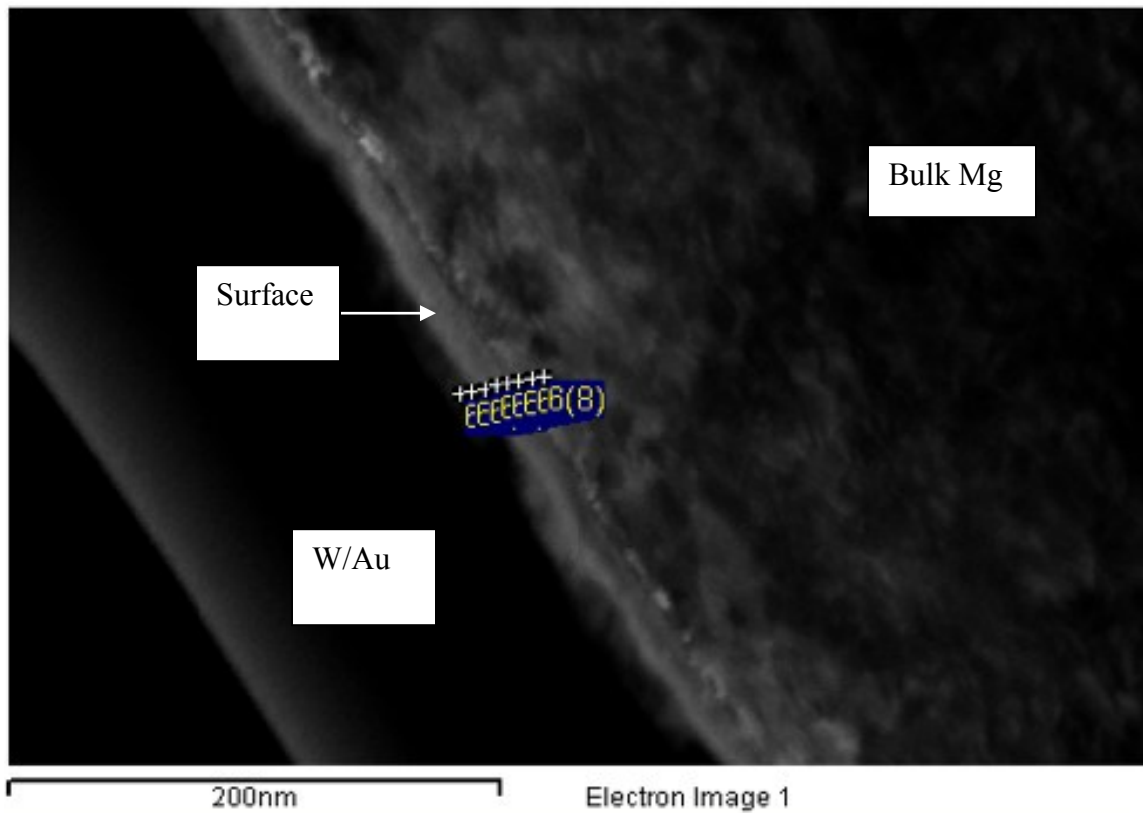


**Figure 3.23 - TEM micrograph of the as received Mg powder showing the surface layer formed on a single particle. The bulk of the powder particle is right of the layer, and the protective coatings to the left.**

Due to limited availability of the FIB-TEM instrumentation because of the relocation of CANMET laboratories from Ottawa to Hamilton the detailed research will

continue in a few months. However, valuable information was already obtained regarding the sintering fundamentals of magnesium powders and is included in the present thesis.

**Table 3.4 - Composition of the Mg surface layer on the as received powder shown in Figure 3.23. Spectrum 1 begins beyond the layer and 8 ends in the bulk of the particle.**

Spectrum	C	O	Mg	W	Au
1	19.51	0.00	2.75	54.73	23.01
2	30.34	6.92	3.39	46.15	13.20
3	39.62	19.70	8.07	21.95	10.65
4	20.72	33.02	21.36	18.89	6.01
5	0.00	28.25	57.99	13.76	0.00
6	0.00	16.21	80.46	3.33	0.00
7	0.00	0.00	96.46	3.54	0.00
8	0.00	5.11	93.12	1.77	0.00

## 3.2 Practical Sintering Strategies

### 3.2.1 *Ground vs. Atomized Magnesium Powder*

#### 3.2.1.1 Uniaxially Pressed Ground Magnesium Powder

The supplied ground pure magnesium powder is shown in Figure 3.24, and its chemical composition is shown in Appendix 1.

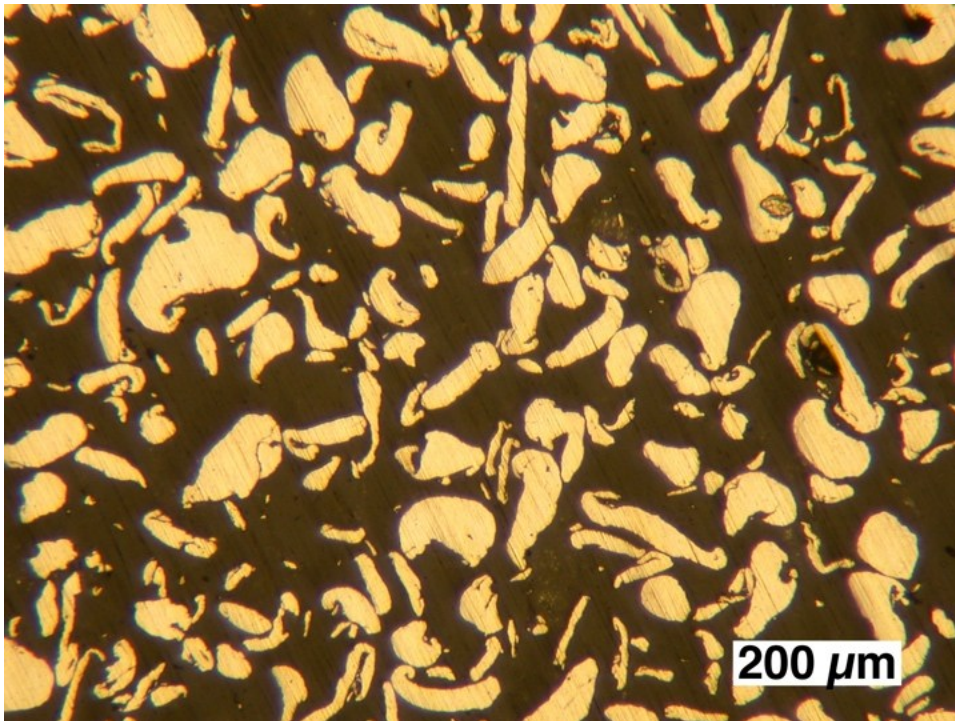


**Figure 3.24 - Optical micrograph of as received ground pure magnesium powder, where the grey phase is magnesium and the black phase is the mounting material.**

As one of the objectives of the present investigation is to compare the effect of the powder size on the sintering process, the magnesium powder was sieved in a glove box

into four categories and the laser analyzer was used to determine the size. Figure 3.25 shows the powder size distribution for two categories of the ground magnesium powders, namely 38-45  $\mu\text{m}$  and 45-53  $\mu\text{m}$ , respectively. It can be seen that for both categories the median diameter, the  $D_{50}$ , is outside the grain size ranges as it was determined by the sieving process. This is due to the fact that the ground powder was not spherical but oval in shape.

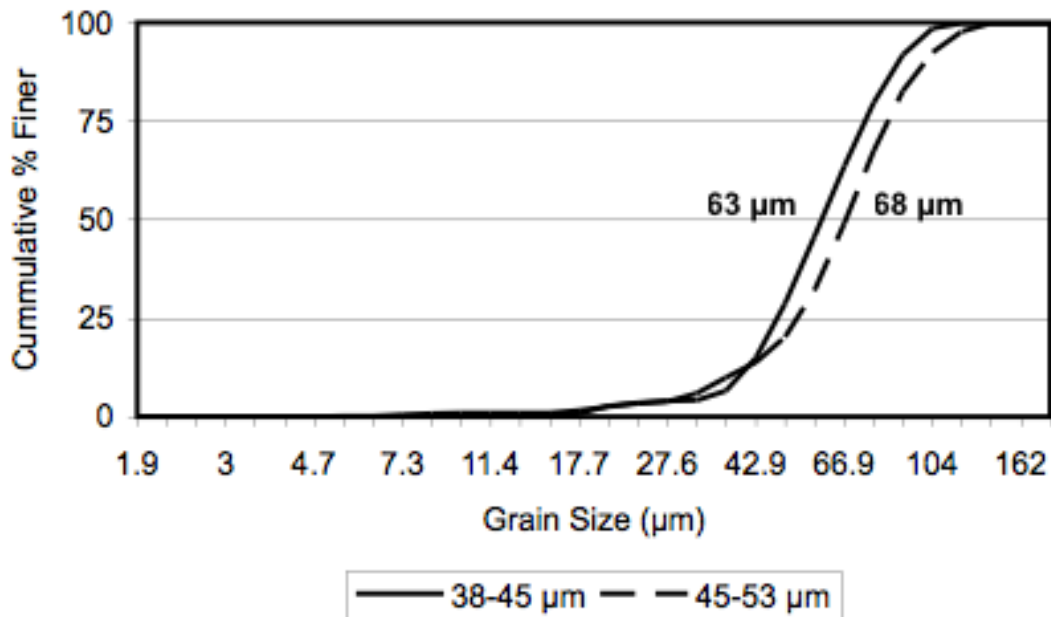


**Figure 3.25 - Particle size distribution for ground magnesium powder categories 38-45  $\mu\text{m}$  and 45-53  $\mu\text{m}$ .**

Ground elemental magnesium powders were consolidated at increasing pressures on the uniaxial press, and the resulting green densities are plotted in Figure 3.26. The density increases sharply up to 300 MPa, at which point increasing compacting pressure

gains little increase in density. For the purpose of studying sintering behaviour in pure magnesium, 500 MPa was chosen to maximize green density and break as much of the surface layer as possible.

Ground magnesium powder was separated into four size categories, and samples were pressed and sintered at 500 °C for 30 minutes. Optimal sintering conditions were estimated from previous work [27]. Due to non-spherical shape of the magnesium particles the size classification categories were not completely separable. The density of the samples was measured before and after sintering, and is shown as a percentage of theoretical in Figure 3.27. The smallest size class (38-45 $\mu$ m) showed the greatest change in density through sintering, and the highest sintered density and lowest change was seen in the largest size category (63-75 $\mu$ m). However, all results are within 2% and therefore the effect of powder size is minimal.

The development of interparticle bonds during sintering leads to the formation of pores between adjacent particles. As sintering continues and interparticle bonds grow, so do these pores. In some cases the density increases during sintering as the volume of the part decreases as pores are eliminated. As Figure 3.27 shows, the density has been reduced from the green state. The samples also show limited change in dimensions after sintering. Therefore the pores formed as interparticle bonds grow are not eliminated and cause a decrease in density of the sintered samples.

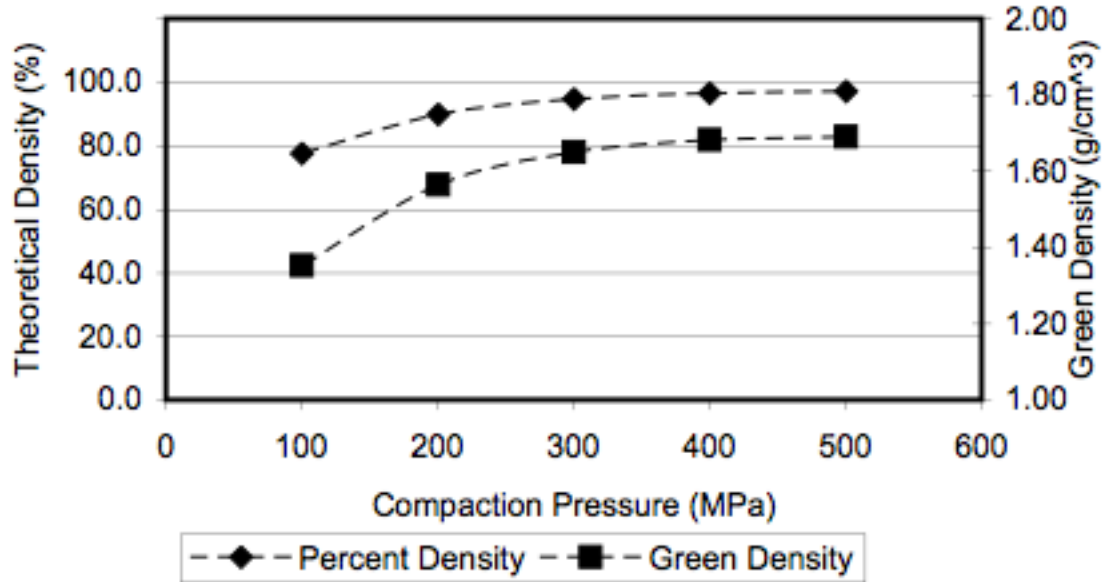


Figure 3.26 - Compaction curve of Uniaxially Die Compacted ground magnesium powder. Symbol size represents approximate error.

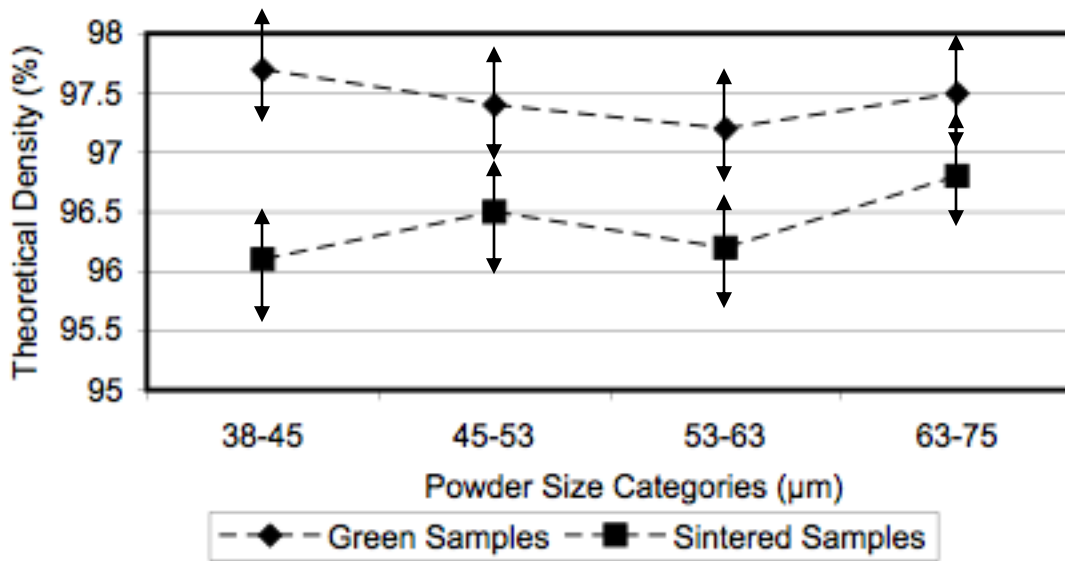
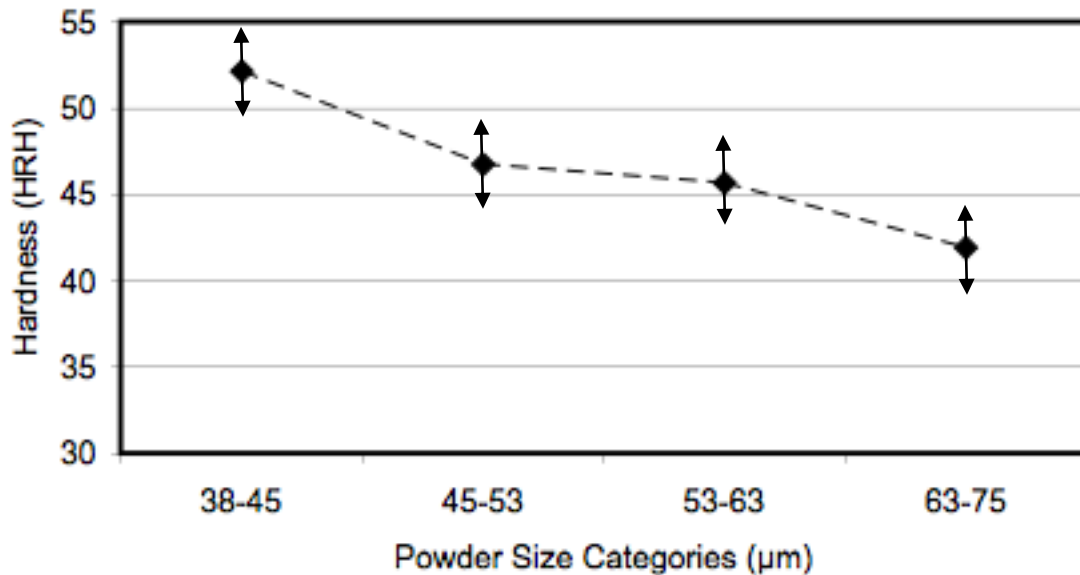


Figure 3.27 - Percent theoretical density of Uniaxially Die Compacted ground magnesium for green samples and samples sintered at 500 °C for 30 minutes.

The hardness of the sintered samples was tested using the Rockwell H scale. The results are shown in Figure 3.28. A slight decrease in hardness is observed as the powder size category is increased. Since the density of each of the size categories is similar, it is unlikely that the increased hardness is related to an increase in the number of interparticle bonds formed and can be explained by grain size effects. As previously reported [13], there is a strong inverse relation between grain size and strength in the case of the magnesium HCP structure according to the Hall-Petch effect.



**Figure 3.28 - Hardness of sintered Uniaxially Die Compacted ground magnesium samples sintered at 500 °C for 30 minutes.**

Next, the effect of the sintering temperature was tested. The sintering temperature was increased to 600 °C while retaining the time and compaction pressure. The 38-45µm size class was compacted, sintered and tested the same way as the 500 °C samples. The

results are shown in Table 3.6. Both the hardness and density increased slightly with increased sintering temperature, which is attributed to further densification due to improved diffusion kinetics at higher temperatures.

**Table 3.5 - Comparison of the properties of Uniaxially Die Compacted ground magnesium powders at various sintering temperatures.**

Property	500 °C	600 °C
Theoretical Density (%)	95.4 ±1	96.0 ±1
Hardness (HRH)	52.2 ±3	53.9 ±3

Green samples and samples sintered at temperatures of 500 and 600 °C were also examined in the SEM. Fracture surfaces were prepared by notching and breaking the samples along the long axis, perpendicular to the compaction direction. The SEM images are shown in Figures 3.29, 3.30 and 3.31. The green sample shows highly deformed magnesium particles packed tightly. It can be seen in both images of sintered samples that interparticle bonds have formed, and pores have grown between particles. It is also possible that some pores are the voids formed from the areas once occupied by wax.

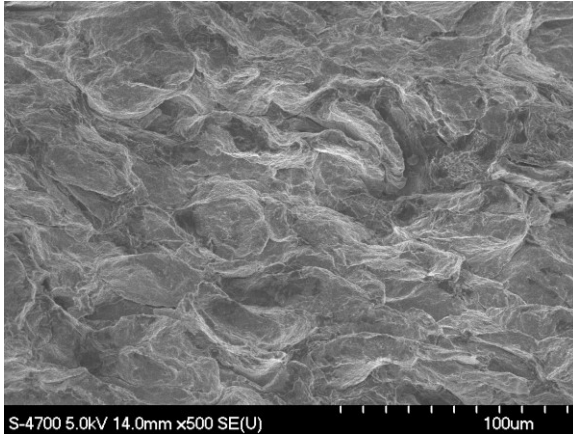


**Figure 3.29 - Micrograph of Uniaxially Die Compacted green ground magnesium.**

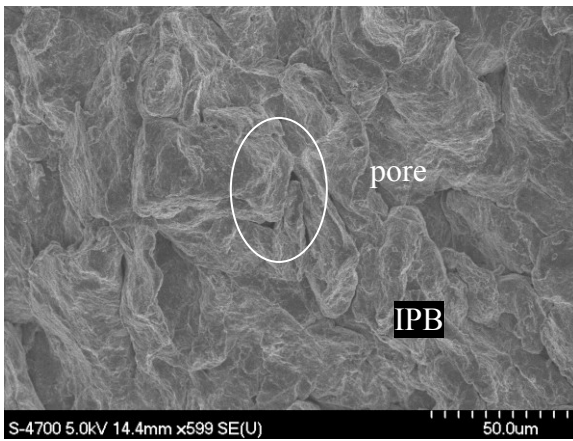


**Figure 3.30 - Micrograph of Uniaxially Die Compacted ground magnesium sintered at 500°C for 30 minutes, with pore and area of interparticle bonding highlighted.**

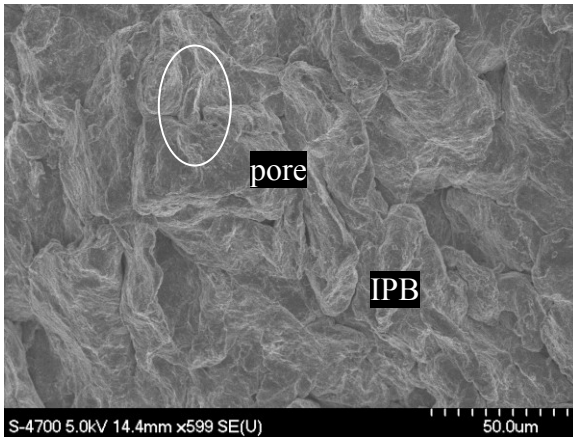


**Figure 3.31 - Micrograph of Uniaxially Die Compacted ground magnesium sintered at 600 °C for 30 minutes, with pore and area of interparticle bonding (IPB) highlighted.**

The effect of sintering time was studied on samples compacted at 500 MPa and sintered at 600 °C. Additional samples were sintered for 10 and 60 minutes, and the comparison of these to samples sintered for 30 minutes is shown in Figure 3.32. The density of the samples sintered for 10 and 60 minutes are similar, but the hardness has been reduced by roughly half that of the 30 minute samples. It appears that both the hardness and density pass through an optimum maximum at the sintering time of 30 minutes. Perhaps the lower sintering time does not allow the formation of sufficient interparticle bonds, and that excessive sintering time may lead to softening through internal grain growth in the original powder particle.

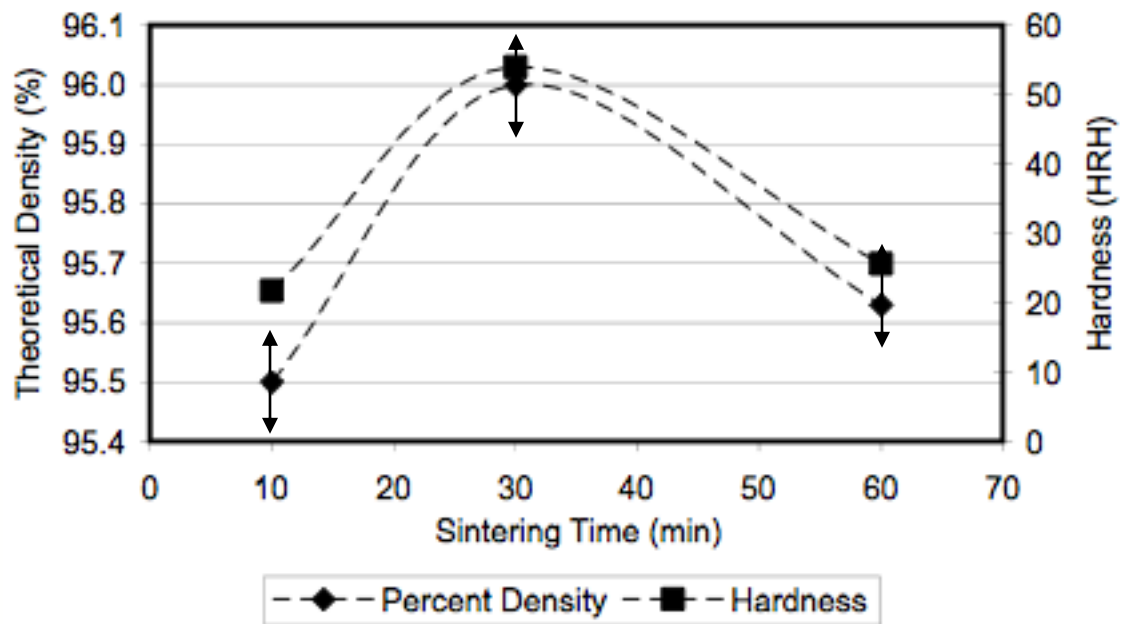


**Figure 3.32 - Effect of sintering time at 600 °C on density of Uniaxially Die Compacted ground magnesium samples compacted at 500 MPa. Symbol size represents approximate error for hardness.**

X-ray diffraction analysis was performed on the green samples and samples sintered at 600 °C to determine the presence of impurities, mainly in the form of oxides. In the resulting diffraction patterns, all peaks present are characteristic of pure magnesium, which indicates that the amount of impurities present, if any, is below 5%, the approximate resolution of the equipment.

### 3.2.1.2 Cold Isostatically Pressed (CIP) Ground Magnesium Powder

To compare with the samples compacted at 500 MPa in the uniaxial press, samples were also compacted in a cold isostatic press at the maximum pressing capacity

of the available equipment, which is 25 ksi (173 MPa). The density of the samples was measured in the same way as the UDC samples and is reported in Figure 3.33. In the case of the larger particle size category, 63-75  $\mu\text{m}$ , the density is slightly increased after sintering, but is lower than that measured in the UDC samples. The 38-45  $\mu\text{m}$  size category shows behaviour like the UDC samples, with a slight loss in density. Compared to the UDC results, the CIP samples have a lower density due to the reduced compaction pressure (173 MPa vs. 500 MPa). However, considering that the compaction pressure is greatly reduced and that the effect on density is small, the performance of CIP is comparable to UDC. Also, because of the absence of wax in the CIP samples, the change in density before and after sintering is reduced. As with the UDC samples, the size of starting powder particle has little effect on the resulting density.

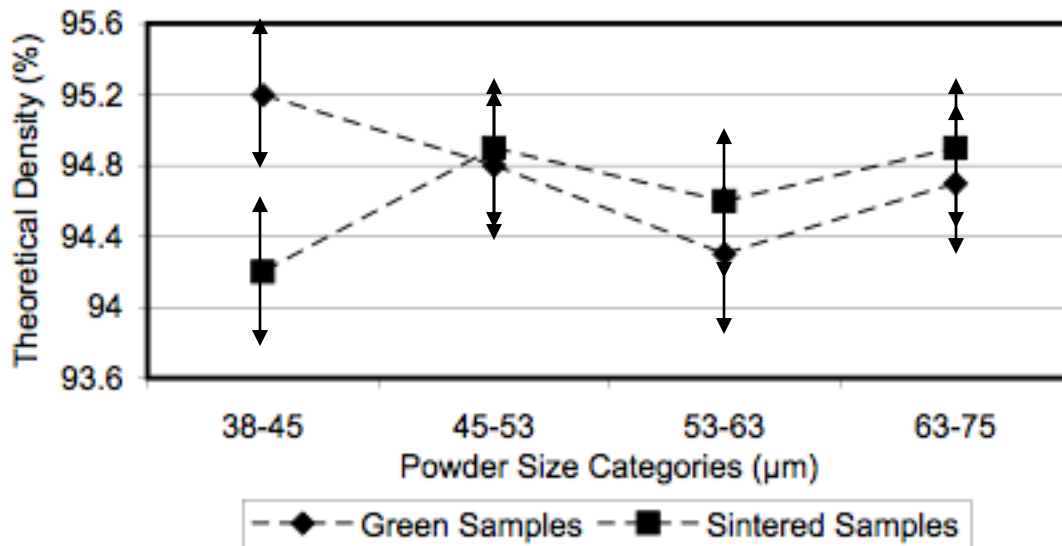


**Figure 3.33 - Percent theoretical density of CIP ground magnesium samples as a function of powder size. Sintering was performed at 600 °C for 30 minutes.**

Hardness measurements of the CIP samples are shown in Figure 3.34. Again, the 38-45  $\mu\text{m}$  size category has the highest hardness, due to the grain size effect and not increased interparticle bonding. However, in all size categories aside from the largest, the hardness has increased from the UDC samples. This result is most likely due to an increased in interparticle bonds formed during sintering. The multi-directional compaction nature of CIP may lead to increased disruption of the surface layer covering each particle, which allows increased interparticle bonds and faster diffusion between particles.

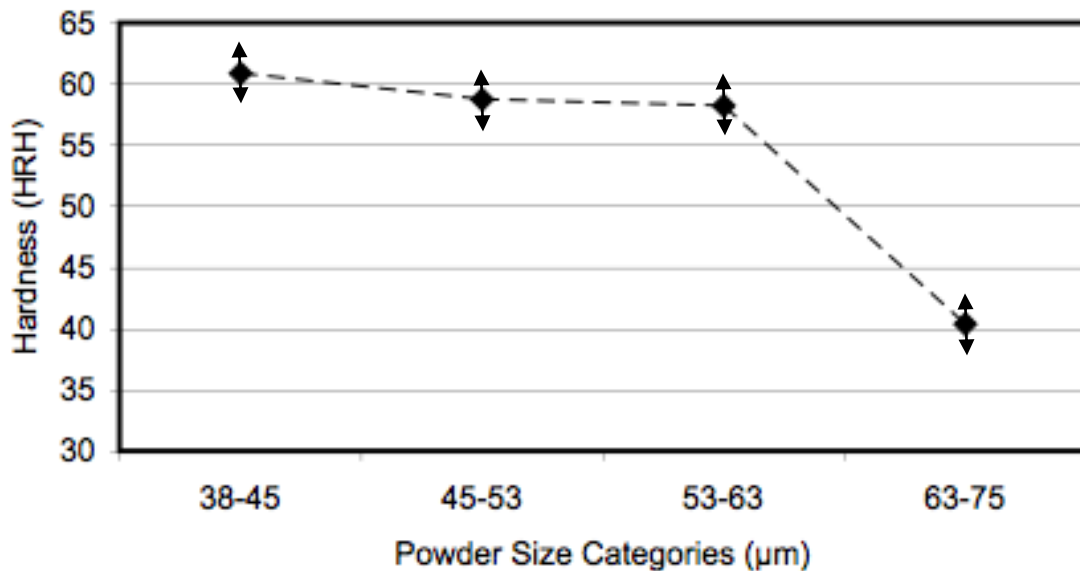


**Figure 3.34 - Hardness of sintered CIP ground magnesium samples as a function of powder size. Sintering was performed at 600  $^{\circ}\text{C}$  for 30 minutes.**

The 38-45  $\mu\text{m}$  size category was chosen for further study, and the effect of sintering time on the density and hardness of the ground powder CIP samples is shown in

Figure 3.35. The density decreases by a small amount as duration increases due to pore growth. Similarly to the UDC samples, the hardness is low at 10 and 60 minutes due to insufficient bonding and annealing of the powder, respectively.

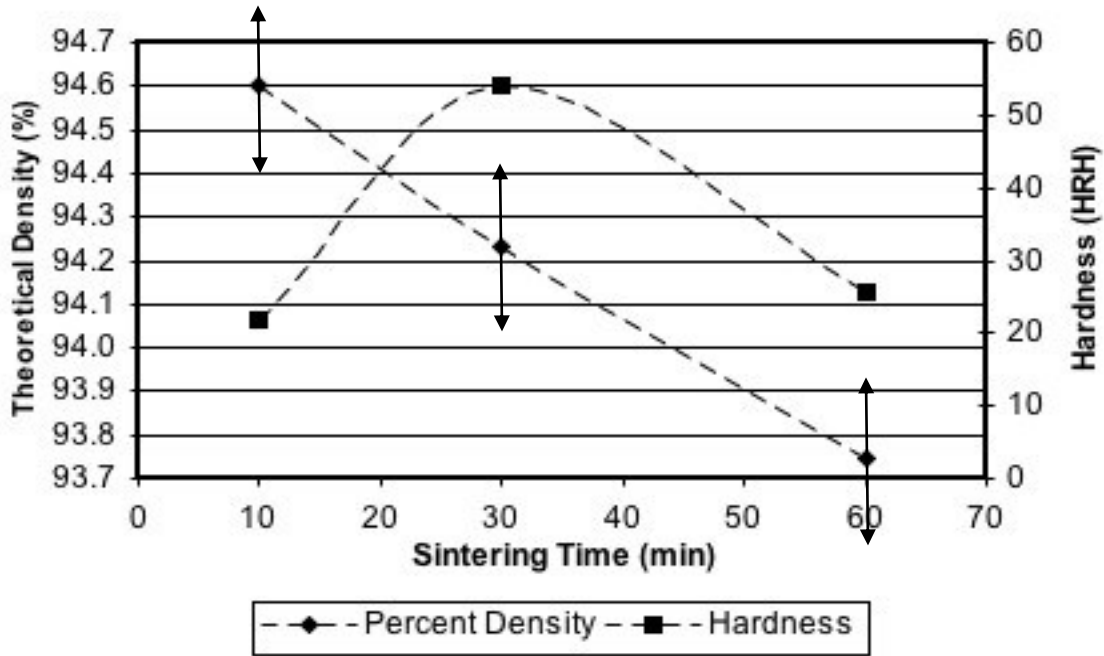


**Figure 3.35 - Effect of sintering time on Cold Isostatically Pressed ground magnesium samples on density and hardness. Sintering was performed at 600 °C. Symbol size represents approximate error for hardness.**

Figure 3.36 shows the results of decreasing the sintering temperature to 500 °C and 400 °C while sintering for 30 minutes. Again, hardness is maximized at the intermediate value, representing a balance between the extent of interparticle bonding and annealing of the powder. The density is high at low sintering temperature because pore growth is low, drops at 500 °C as pore growth is outpacing interparticle bonding and

raises again at 600 °C once densification due to bonding begins to counter pore growth. Microstructural evidence is presented in the following section.

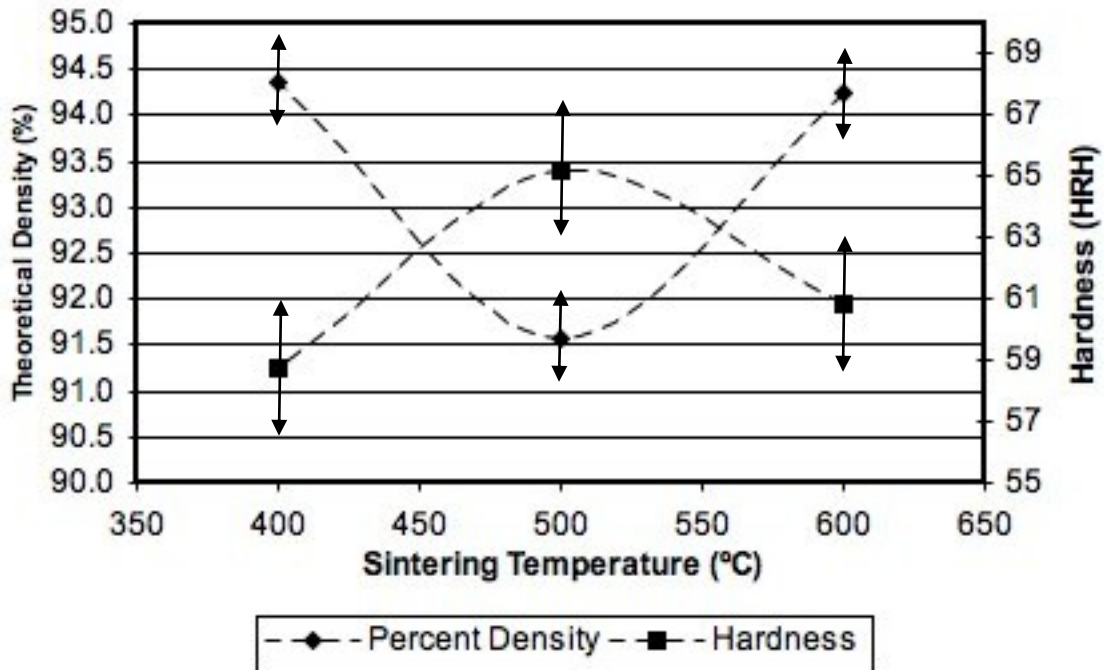


**Figure 3.36 - Effect of sintering temperature of Cold Isostatically Pressed ground magnesium samples on density and hardness. Sintering time was 30 minutes.**

### 3.2.1.3 Cold Isostatically Pressed (CIP) Atomized Magnesium Powder

The supplied atomized pure magnesium powder is shown in Figure 3.37, and chemical composition data is included in Appendix 1.

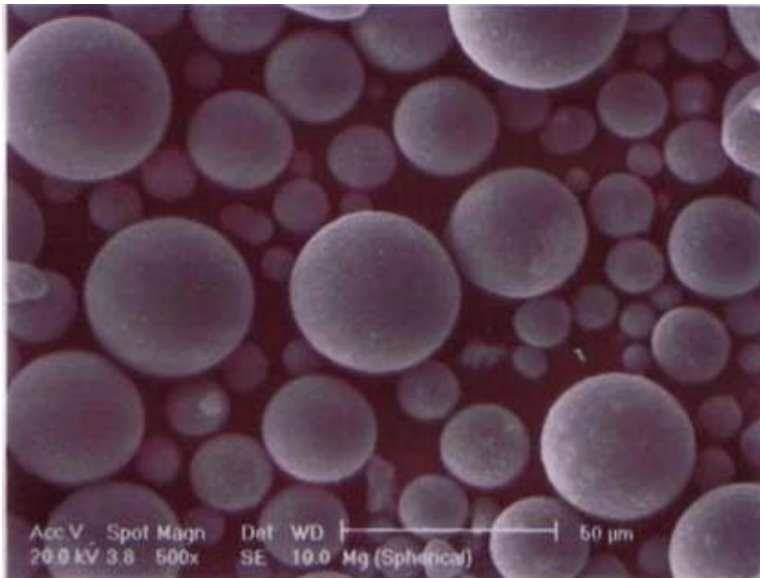


**Figure 3.37 - SEM micrograph of as received atomized pure magnesium powder.**

Because it was found that a small powder size provided superior properties due to grain size effects, the atomized powder was ordered in a small size fraction from the supplier to eliminate any exposure to oxygen during sieving.

Atomized CIP samples were first sintered for 30 minutes at 500 °C and 600 °C to determine the effect of temperature. The samples sintered at 500 °C were poorly sintered, and were found to be too friable for testing. The extent of interparticle bonding at the lower temperature appears to be insufficient to form strong bonds, and the sample was easily cracked when subjected to a hardness test. Therefore the 500 °C temperature was abandoned and the effect of sintering time at 600 °C was studied.

To further explore the effect of long sintering temperatures, atomized CIP samples were sintered for 90 and 120 minutes, as well as 10, 30 and 60 minutes studied

previously for the ground powder. The resulting theoretical density and HRH hardness is shown in Figure 3.38. The density and hardness at the 10 minute duration is similar to the properties of the green compact, as only a small amount of interparticle bonding has taken place. During the first stages of sintering, pores are growing at a rate faster than bonds are forming, and the density decreases slightly.

Because atomization involves no physical working, the powder has less internal strain compared to the ground powder. However, stress is induced during compaction, which gives the 10 minute duration sample a higher hardness than the 30 minute duration because the compaction strain has been relieved but interparticle bonding has not matched pore growth.

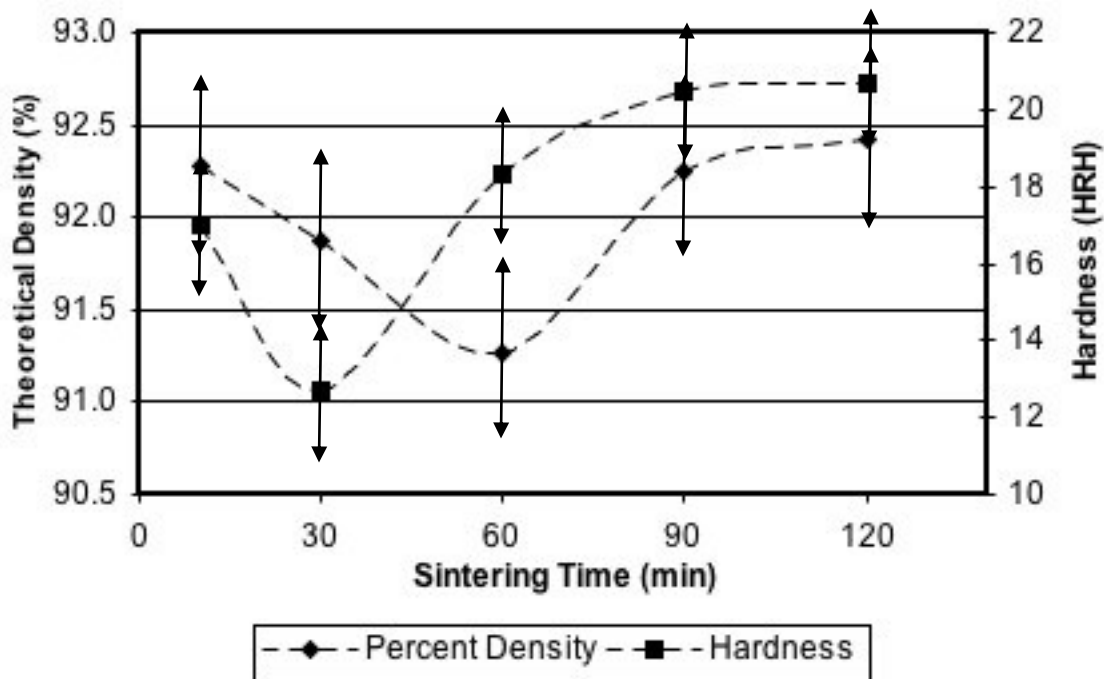


**Figure 3.38 - Effect of sintering time on Cold Isostatically Pressed atomized magnesium samples on density and hardness. Sintering was performed at 600 °C.**

At 60 minutes, the extent of interparticle bonding is beginning to counter the density loss due to pore growth, and hardness is increasing. Beyond 60 minutes, hardness and density are both increased as bonding outpaces pore growth. It can be seen however, that the samples prepared with atomized powder are roughly half the hardness of the similar ground powder samples. It is hypothesized that the mechanical interlocking of the ground powder contributes to the hardness.

#### 3.2.1.4 Uniaxially Pressed Atomized Magnesium Powder

It was found that the pure atomized powder could not be pressed uniaxially, as the compacts would crack and split (delaminate) perpendicular to the compaction direction upon ejecting from the die. Green strength is very low, possibly due to the spherical shape of the powder, and the sharp stress relief as the part is ejected from the die was enough to fracture the weak bonds between particles formed during compaction. Previous samples prepared with the CIP were viable because of the multi-directional compaction and the more gradual stress relief as pressure was bled from the chamber. To allow testing of the atomized powder with UDC, ground powder was mixed with the atomized to provide sufficient mechanical interlocking. It was found that a minimum of 20 % ground powder was needed to produce viable samples.

#### **3.2.2 Extended Sintering Time**

In light of the previous results of this study, atomized magnesium samples containing 20% ground powder were compacted at 500 MPa and sintered at 600 °C. A sintering time of 40 minutes was chosen to attempt to balance pore growth, bonding and

annealing of the ground powder portion. Because of the favourable properties with increasing sintering time found with CIP compaction of 100% atomized powder, samples were also sintered for 360 minutes. The resulting properties are found in Table 3.8, and optical microstructures are shown in Figures 3.39 and 3.40.

**Table 3.6 - Comparison of the properties of Uniaxially Die Compacted atomized magnesium powders compacted at 500 MPa and sintered at 600 °C for various sintering times.**

	40 minutes	360 minutes	Cast [1]
Theoretical			
Density (%)	95.1 ±1	94.8 ±1	99%
Hardness (HRH)	47.8 ±3	65.5 ±3	70
UTS (MPa)	25 ±5	72 ±5	90
Elongation (%)	0.1 ±.01	1.5 ±0.1	2-6

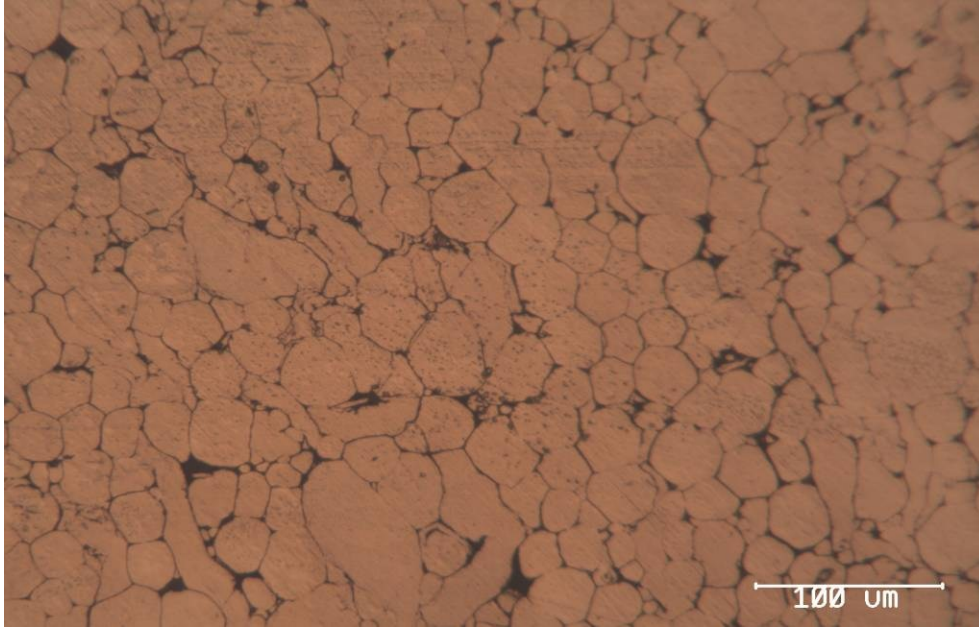


**Figure 3.39 - Optical microstructure of atomized UDC sample sintered at 600 °C for 40 minutes.**

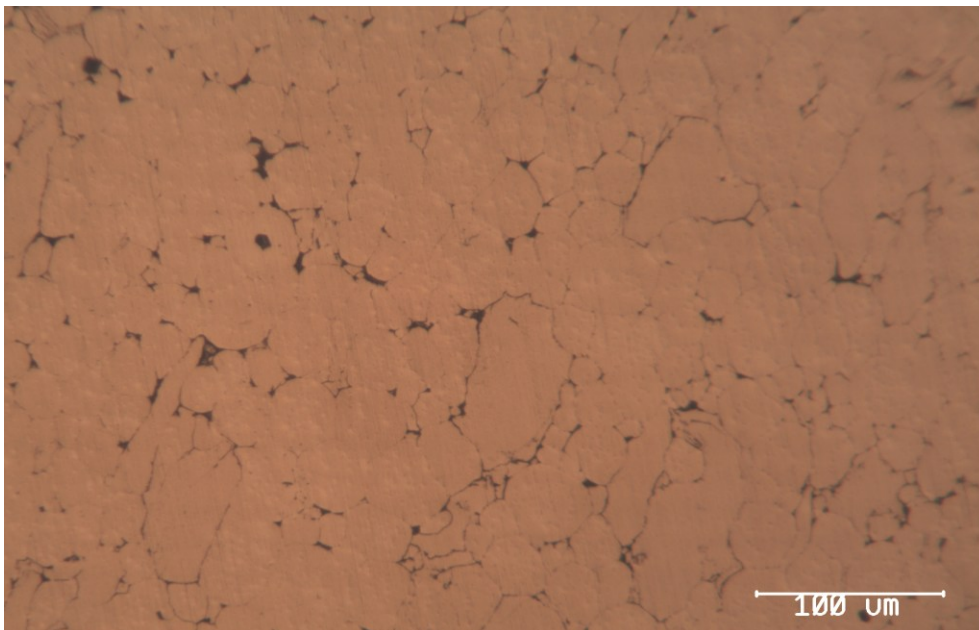


**Figure 3.40 - Optical microstructure of atomized UDC sample sintered at 600 °C for 360 minutes.**

The density of the samples, as well as the visible porosity in the micrographs, is very similar. However, the difference in the extent of interparticle bonding from the 40 minutes to the 360 minutes sintering time sample is clearly shown in Figures 3.39 and 3.40, respectively, as can be seen by the disappearance of some of the original powder's grain boundaries. This change is reflected in the hardness, ultimate tensile strength and elongation of the sample, where the 360 minute sintered sample is superior in each aspect. While superior, the mechanical properties are still not comparable to that of cast pure magnesium due to the presence of porosity.

At both sintering temperatures density is similar, so pore growth has halted by 40 minutes. Beyond that duration, the increase in properties can be explained by the quality of interparticle bonds. By extending the time of sintering the bonds that have formed in the cracks through the surface layer in adjacent particles expand, increasing the strength of the bonds. It is also possible that the length of sintering time allows metal to diffuse through the surface layer and forming new bonds not associated with cracks from compaction. However, further densification is not occurring because pores are not being eliminated.

### **3.2.3 Alloying Additions**

#### 3.2.3.1 Strengthening

##### *3.2.3.1.1 Aluminum and Zinc*

Aluminum and zinc are both soluble in magnesium and are known to strengthen through solid solution. Table 3.7 shows the results of samples containing 8% aluminum,

1% zinc and a combination of both aluminum and zinc compared to pure magnesium. The addition of aluminum and zinc provide increased density and hardness, but result in a swelling of the sample. The combination of the two alloying elements gives the best properties. Swelling is minimal at below 1%, and likely caused by the formation of eutectic liquids that are absorbed by the matrix magnesium.

**Table 3.7 - Properties of Mg samples alloyed with Al and Zn. Compacted 500MPa, sintered 600°C for 40min.**

	<b>Density (g/cc)</b>	<b>Hardness (Rockwell H)</b>	<b>Max Dimensional Change (%)</b>
Mg	1.41 ±0.1	47.8 ±5	-0.6 ±0.2
Mg-8Al	1.73 ±0.1	86.7 ±3	0.9 ±0.2
Mg-1Zn	1.69 ±0.1	64.4 ±5	0.2 ±0.2
Mg-8Al-1Zn	1.74 ±0.1	88.1 ±4	0.9 ±0.2

### 3.2.3.2 Liquid Forming

#### 3.2.3.2.1 Tin

Tin was chosen as a liquid phase forming alloying addition because of its low melting temperature. Figure 3.41 shows the resulting microstructure. The tin addition of 5% is beyond the solubility of tin in magnesium, and the dark areas are tin rich liquid phase that has frozen after sintering. Sintering appears more complete compared to unalloyed magnesium samples, which is proven by the increased density and hardness as

seen in Table 3.8. The tin addition also causes slight swelling in the samples due to the absorption of tin to its maximum solubility.

**Table 3.8 - Properties of Mg alloyed with 5% Sn. Compacted 500MPa, sintered 600°C for 40min.**

	<b>Density (g/cc)</b>	<b>Hardness (Rockwell H)</b>	<b>Max Dimensional Change (%)</b>
Mg	1.41 ±0.1	47.8 ±5	-0.6 ±0.2
Mg-5Sn	1.74 ±0.1	60.5 ±4	0.6 ±0.2

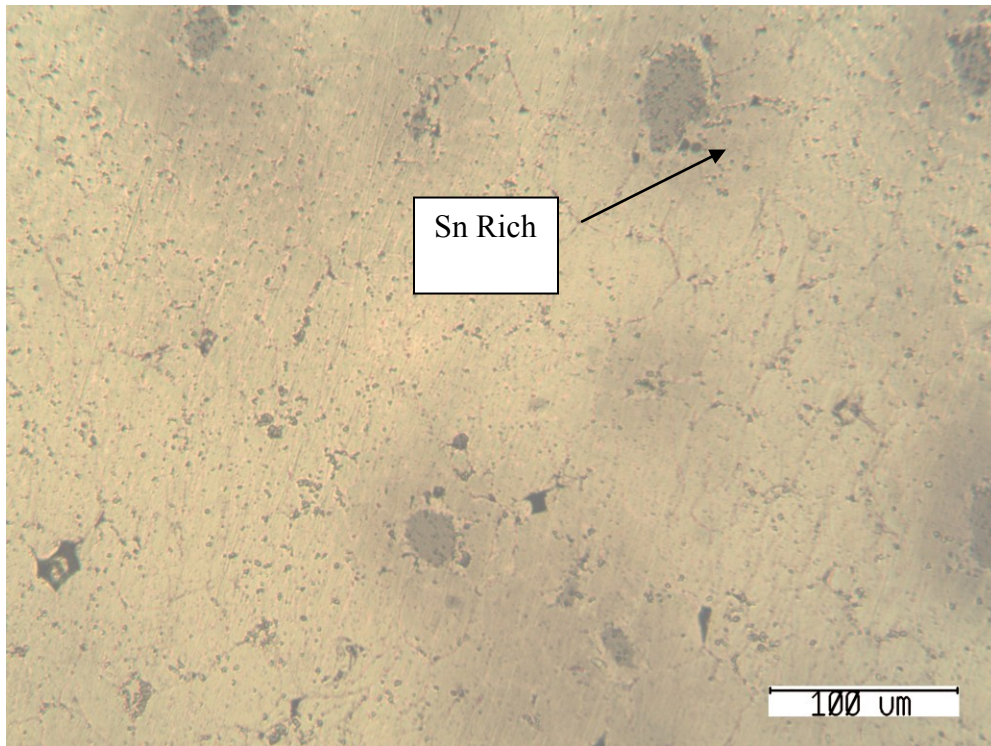


**Figure 3.41 - Pure Mg alloyed with 5% Sn. Compacted 500MPa, sintered 600°C for 40min.**

### 3.2.3.3 Surface Layer Disrupting

#### 3.2.3.3.1 *Calcium*

Samples were prepared for CIP compaction with pure magnesium atomized powder, with a single granule of calcium at one end. Following sintering, the end of the samples which contained the granule of calcium had noticeably slumped, indicating a large amount of liquid had formed. In the Mg/Ca binary phase diagram, eutectics form at 445°C on the calcium rich side, and at 517°C on the Magnesium rich side. One or both eutectics formed during sintering, as the sintering temperature was 600°C, leading to the calcium rich end of the samples losing the ability to hold its own weight, and resulted in the slumping.

The samples were cut in half along the long axis, and polished. Even with the naked eye, several different regions were visible, as shown in 42. In the region directly surrounding where the granule of calcium had been placed was the liquid that had caused the slumping. No evidence of the original calcium granule was present in most samples. A pore roughly the size of the granule remained in some samples where the granule had been enveloped with Mg powder.

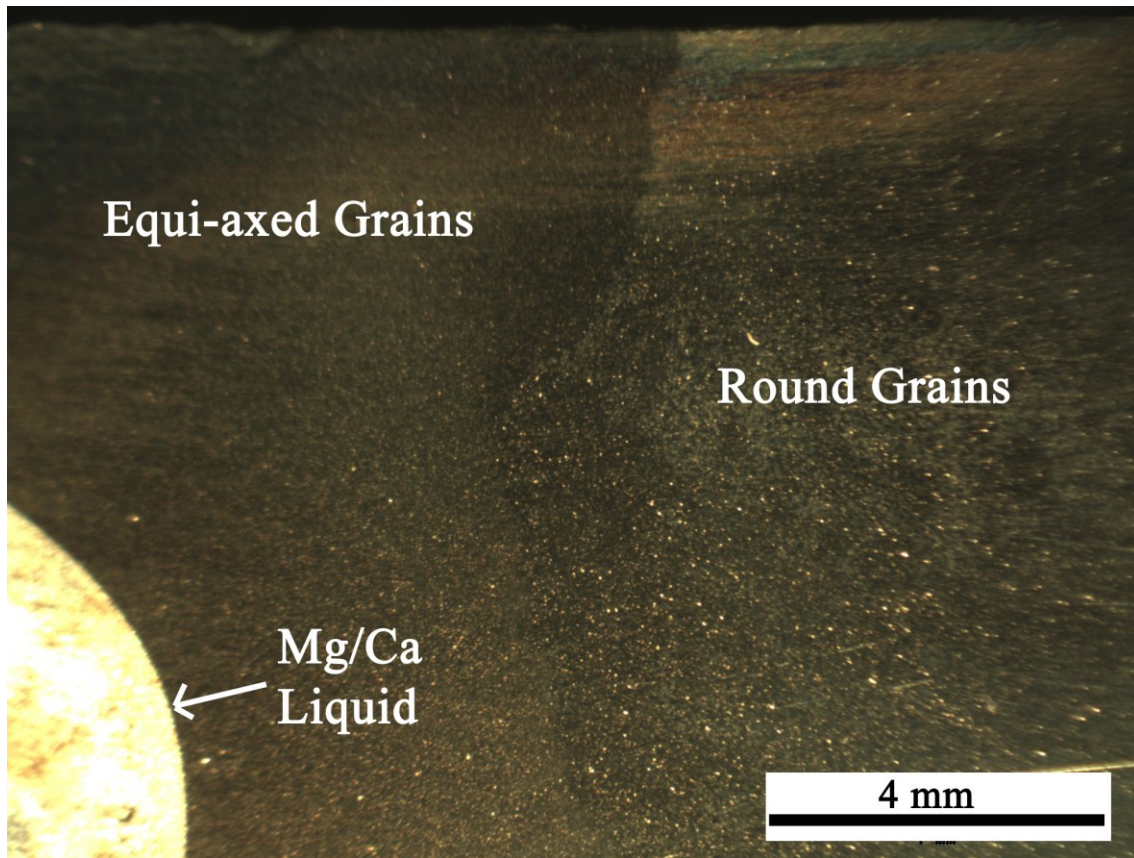


**Figure 3.42 – An optical microscopy macrograph showing the eutectic liquid, equi-axed and rounded grain section of the sample. Calcium rich area at left.**

The liquid region was examined with an optical microscope, and the microstructure is shown in Figure 3.43. The light areas are magnesium powders that have been rounded by the eutectic reaction, forming the dark liquid surrounding them. The liquid has frozen in the typical lamellar eutectic structure.

Beside the liquid region in Figure 3.42 is a darker region. Figure 3.44 shows the boundary between the liquid region and the next, which is composed of equi-axed magnesium grains. In this region, diffusion between original magnesium particles was

rapid, and necks have formed between contacts with adjacent particles. The original spherical morphology has completely disappeared in favour of the low energy equi-axed arrangement. Evidence of the eutectic liquid frozen at the grain boundaries and in what had been pores between particles prior to sintering can also be seen. This would indicate that the liquid had been drawn from the calcium rich end of the sample by capillary action. The liquid readily wet the magnesium particles, and reacted with the surface layer, disrupting it, and allowing rapid diffusion through the liquid. It appears in this case that calcium is acting as both a layer reducing additive and a liquid phase forming additive.

The next region visible in Figure 3.42 is slightly lighter in colour than the equi-axed grain region. Figure 3.45 shows the transition between the equi-axed region, and this new region where the magnesium particles more closely resemble their original spherical shape. This would indicate that sintering was largely unsuccessful, as strong bonds between particles have not formed. There is still evidence of frozen eutectic liquid at the grain boundaries, but it is possible the length of time it took to be drawn to this region was long, and sufficient time to assist in sintering was not available. It can also be seen that there is porosity present that has not been filled with liquid. This region of the samples is very similar to samples composed of pure magnesium, with no additions.

Figure 3.45 also shows the amount of necking taking place at the end of the equi-axed region is less than in Figure 3.44. This would indicate that there is a gradient of density from the calcium rich end of the sample, attributed to how much time was required for the liquid to reach that area of the sample.

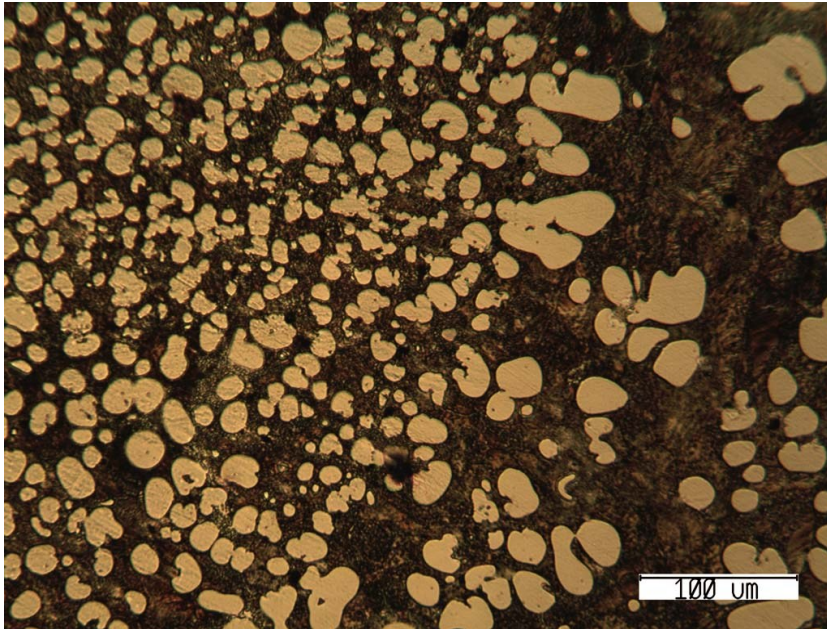


**Figure 3.43 - An optical microscopy micrograph showing the eutectic liquid region. Dark areas are eutectic liquid, and light areas are Mg.**

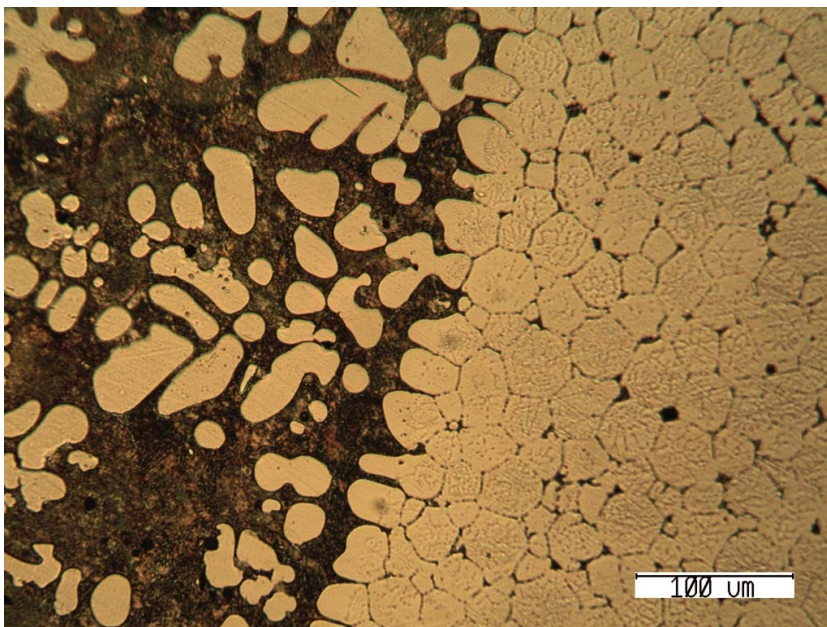


**Figure 3.44 - An optical microscopy micrograph of the boundary between the eutectic liquid and the equiaxed regions. Calcium rich area at left.**

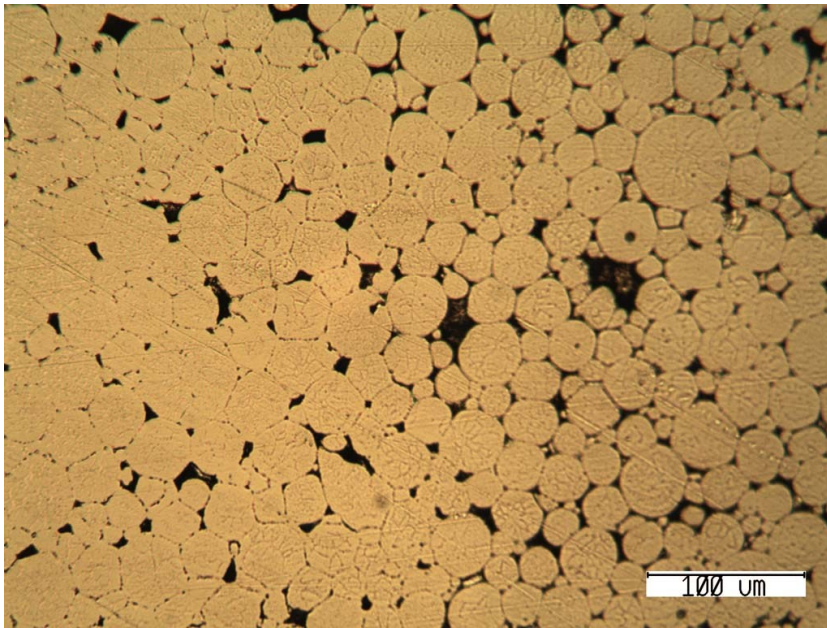


**Figure 3.45 - An optical microscopy micrograph of the transition area between equiaxed and rounded grain regions. Calcium rich area at left.**

To determine the approximate composition of the different regions, and the phases contained in each, electron dispersive spectroscopy (EDS) was performed. The results are shown in Table 3.9. All areas contained some amount of carbon and oxygen, which are the two primary impurities found in the base powder, and also the major constituents of the surface layer (in the form of carbonate and oxide).

**Table 3.9 - Composition of regions of interest, determined by EDS. Reported as weight percent.**

	<b>C</b>	<b>O</b>	<b>Mg</b>	<b>Ca</b>
Mg/Ca liquid	7	7	73	13
Equi-axed grain	2	3	94	1
Equi-axed grain boundary	2	6	78	14
Rounded grain	4	4	92	0
Rounded pore	18	34	47	1

The liquid region has a composition close to that of the eutectic on the magnesium rich side of the phase diagram (16%). The remaining unreacted magnesium particles contained in this region will make the overall amount of magnesium in this area greater than the eutectic composition.

Inside the equi-axed grain region, the grains of magnesium show approximately 1% calcium in solution, which is close to the maximum solubility of calcium in magnesium according to the phase diagram (1.35%). At the grain boundaries in this region, a composition much closer to the actual eutectic is found. The presence of the carbon and oxygen are the likely reason it is not the exact eutectic composition.

Once the rounded grain region is reached, no calcium is found in solution with the magnesium grain, indicating no calcium has reached this region, or it has not been

present long enough to go into solution. It can also be seen that the carbon and oxygen levels are higher in this region. Without the calcium present to disrupt the layer, the layer remains over the magnesium particle and is a barrier to diffusion. The result is much poorer interparticle bonding in this region.

Inside the rounded grain region, a much larger amount of porosity is present, and it is either partially filled with liquid, or not filled at all. The composition of the bottom of a pore in this region shows a very small amount of calcium present, but large amounts of carbon and oxygen from the surface layers of the surrounding magnesium particles.

The polished cross sections of the samples were also tested for hardness. A hardness profile was created by testing at specific intervals along the length of the samples, starting at the end where the calcium granule had been. Table 3.10 shows the results, with the distance from the calcium rich end as well as in which region the test point was.

**Table 3.10 – Apparent Hardness of regions of interest measured with Rockwell H scale. Negative values indicate a lower scale should be chosen, but results are included only to show reduced hardness in the rounded grain region.**

	<b>Distance from Ca rich end (mm)</b>	<b>HRH</b>
Mg/Ca	2	75.4 ±2
liquid	4	75.9 ±2
Equi-axed grains	6	73.4 ±2
	8	70.0 ±2
	10	61.9 ±2
Rounded	15	-15 ±10
	20	-20 ±10
	40	-55 ±10

At the calcium rich end of the sample, the hardness was high at 75 HRH. The second test point at 4mm was very similar, but may be that the placement of the Ca granule was not exactly at the end of the sample. This is also supported by Figure 3.43, where the very end of the sample at the left contains a smaller amount of the eutectic liquid than at the right, and also less than at the left of Figure 3.44 just before the equi-axed region.

In the equi-axed region, the hardness at the point closest to the liquid region is almost as high as the liquid region, indicating very good sintering at this point. As the distance from the calcium rich end increases, the hardness is reduced. This is also

supported in Figure 3.45, were it was seen that the extent of interparticle bonding at the end of the equi-axed region was reduced, and the amount of porosity increased.

Once the rounded grain region of the sample is reached, there is a dramatic reduction in hardness. While the numerical result of a negative test value in a hardness experiment is largely meaningless, the trend shows that the calcium has some small effect closer to the calcium rich end, but as the distance is increased, the effect becomes much less. However, the sudden change from 60 HRH to a result of less than zero shows that there is a threshold amount of calcium required to assist sintering, and once it is past, any amount less will have very little effect.

#### 3.2.3.3.2 *Yttrium*

Yttrium was chosen as an alloying addition for its ability to disrupt the oxide layer of magnesium, its solubility in magnesium and because it will contribute to the liquid phase during sintering. A 2wt% addition will theoretically provide enough yttrium to reduce the MgO present and leave an excess to assist in liquid formation. Table 3.13 shows the resulting properties of the Mg-8Al alloy with and without yttrium. From the table, it can be seen that both alloys swelled during sintering, resulting in a decrease in density. The swelling was due to the formation of the liquid phase, which forced adjacent grains apart as capillary action draws the liquid between them. The swelling was slightly higher in the alloy with yttrium, primarily because of the greater amount of liquid formed.

The decrease in density can be attributed to the pores left behind as the particles of aluminum, or aluminum and yttrium, react to form the liquid and leave a pore where the particle had been. Again, the effect is more pronounced in the alloy with the yttrium addition, because of the larger liquid fraction. The apparent hardness was also lower in the yttrium containing alloy, likely due to the lower density.

Figures 3.46 (a) and (b) show the sintered microstructure of the Mg-8Al and Mg-8Al-2Y, respectively. Both contain a large number of small pores, which are the typical PM residual porosity resulting from gaps between adjacent particles. The larger pores are those that were previous aluminum particles in (a), and previous aluminum and yttrium particles in (b). It can be seen that the size of these pores are larger in the case of (b) because of the larger liquid fraction, and resulting in a lower sintered density. Un-reacted yttrium particles can also be seen in (b), which are due to yttrium own highly stable surface layer which impedes the eutectic reaction and subsequent liquid formation.

**Table 3.11 - Effect of 2 wt% Y addition on Mg-8Al alloy. Densities reported as % of theoretical.**

	<b>Green Density (%)</b>	<b>Sintered Density (%)</b>	<b>Hardness (Rockwell)</b>	<b>Max Dimensional Change (%)</b>
Mg-8Al (Ar)	93 ±1	90 ±1	82 H ±2	5 ±0.5
Mg-8Al-2Y (Ar)	93 ±1	84 ±1	66 H ±3	6 ±0.5

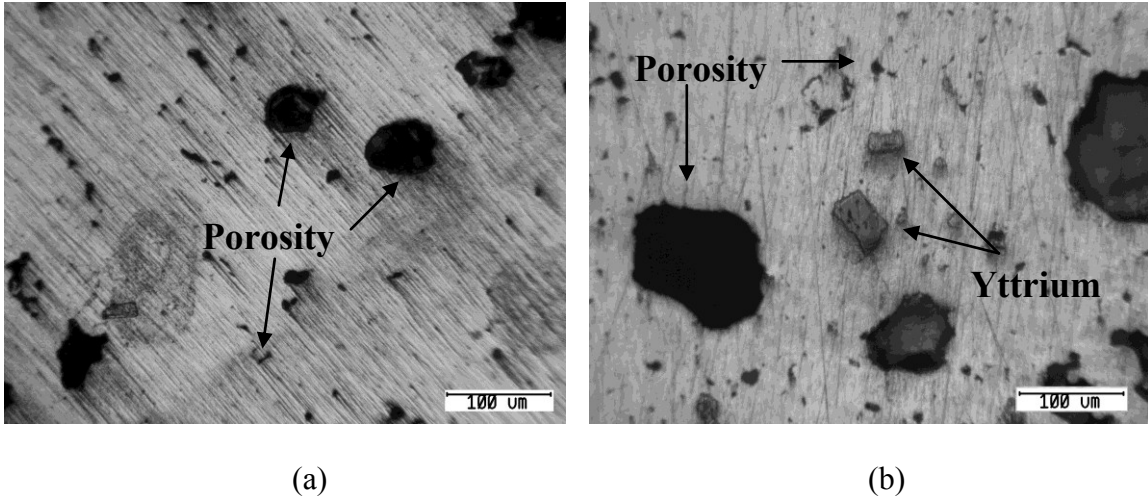


**Figure 3.46 – Comparison of the microstructure of (a) Mg-8Al and (b) Mg-8Al-2Y sintered in argon. Note the porosity present in (a) and (b), and the un-reacted yttrium in (b).**

### **3.2.4 Sintering Atmosphere**

The effect of sintering select alloys in argon and nitrogen was tested. Table 3.14 shows the results of sintering the Mg-8Al and Mg-8Al-2Y alloys in argon and nitrogen. The effect was the same on both alloys; in the nitrogen atmosphere the amount of swelling reduced, the density was increased and the apparent hardness increased. The nitrogen atmosphere resulted in dramatically improved properties, where it not only stopped the reduction of density, but improved upon it compared to the green state. This indicates the residual porosity from previous aluminum and yttrium particles were indeed filled, and also some of the typical PM porosity present between adjacent particles was also reduced.

Looking to Figure 3.47 (a) and (b), it can be seen that the amount of large porosity from previous particles was greatly reduced from that shown in Figure 3.46(a) and eliminated in Figure 3.47(b). The small typical PM porosity is also was reduced in Figure 3.47(a) and greatly reduced in Figure 3.47(b), as compared to Figure 3.46(a) and (b). It is theorized that nitrogen gas trapped in pores reacts to form nitrides. This reduces the pressure inside pores and allows the pores to be filled through densification. There was no longer un-reacted yttrium present in the samples, but now areas where the eutectic Mg-Al-Y liquid has formed and frozen after cooling are present, as shown in Figure 3.47(b). The nitrogen atmosphere has allowed greater interaction between the yttrium and magnesium/aluminum matrix through the formation of nitrides, which allow improved wetting and migration of the liquid phase.

**Table 3.12 - Effect of sintering atmosphere on Mg-8Al alloy, and Mg-8Al-2Y alloy.**

**Densities reported as % of theoretical.**

	<b>Green Density (%)</b>	<b>Sintered Density (%)</b>	<b>Hardness (Rockwell)</b>	<b>Max Dimensional Change (%)</b>
Mg-8Al (Ar)	93 ±1	90 ±1	82 H ±2	5 ±0.5
Mg-8Al (N <sub>2</sub> )	92 ±1	95 ±1	87 H ±2	1 ±0.1
Mg-8Al-2Y (Ar)	93 ±1	84 ±1	66 H ±2	5 ±0.5
Mg-8Al-2Y (N <sub>2</sub> )	94 ±1	95 ±1	81 H ±2	2 ±0.1

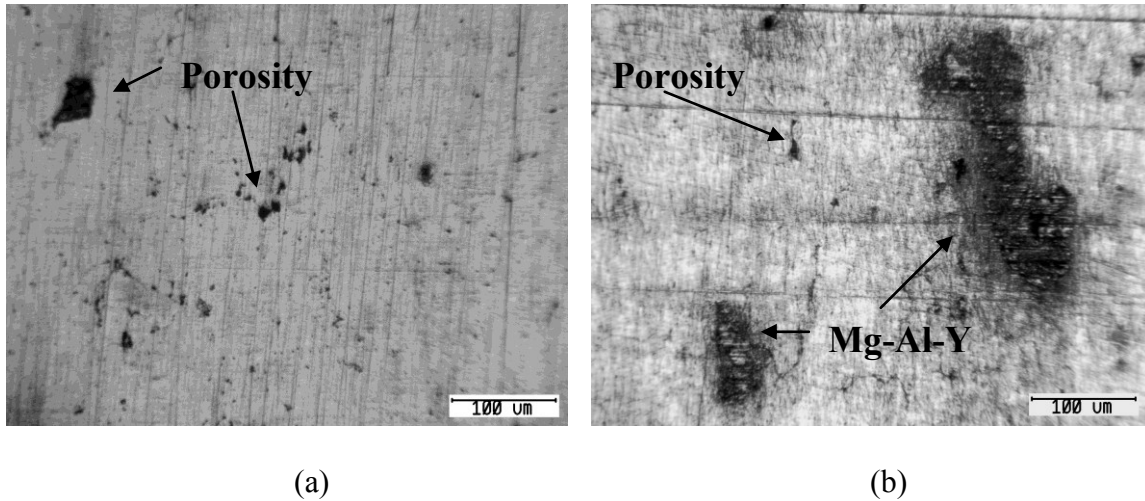


**Figure 3.47 - Comparison of the microstructure of (a) Mg-8Al and (b) Mg-8Al-2Y sintered in nitrogen. Note the porosity present in both (a) and (b), and the frozen eutectic liquid in (b).**

### **3.2.5 Cold and Hot Working**

Hot rolling was chosen to assess the benefit of increasing the density of the Mg-8Al and Mg-8Al-2Y compacts sintered in both Ar and N<sub>2</sub> to near-theoretical density. Test samples were heated to 350 °C and rolled in 0.127 mm increments until the first signs of cracking were apparent. Subsequent samples followed the same procedure up to 0.254 mm of cracking of the test sample. The results of hot rolling are shown in Table 3.15. The Mg-8Al compacts sintered in argon proved ductile enough to allow a 52% reduction in cross section, with a 4% increase in density to 94%. In the case of the Mg-8Al compact sintered in nitrogen, the samples were too friable to roll, and all cracked and broke with very little reduction. It would appear that the nitride formed was brittle. This nitride

would be found in pores and along grain boundaries, which would lead to opportunistic crack initiation sites and intergranular propagation.

In the case of the Mg-8Al-2Y compacts sintered in Ar, there was a large increase in density, from 84 to 93%, due to a reduction in cross section of 41%. The yttrium containing compacts sintered in nitrogen were successfully hot rolled, attaining a near-theoretical density of 99% from 95%, which was accomplished in less reduction (26%) than the Ar sintered compacts. The addition of 2 wt% yttrium leads to the formation of yttrium nitride, which is more stable than yttrium oxide, and decreases the brittleness that made the Mg-8Al alloy too friable to allow rolling.

The effect of increasing the density was most apparent in hardness, where it had increased by a large factor in all samples successfully rolled, climbing an entire scale in the Rockwell test from H to E. While there are no wrought magnesium alloys with exact compositions, a similar alloy, AZ91 (Mg-9Al-1Zn), has a hardness of 75 HRE.

**Table 3.13 - Effect of hot work on Mg-8Al alloy sintered in Ar and N<sub>2</sub>, and with addition of 2 wt% Y. Sample Mg-8Al (N<sub>2</sub>) proved too friable to roll, and cracked after a small amount of reduction. Densities reported as % of theoretical.**

	<b>Reduction (%)</b>	<b>Final Density (%)</b>	<b>Density Increase (%)</b>	<b>Hardness (Rockwell)</b>
Mg-8Al (Ar)	52 ±5	94 ±1	4	84 E ±2
Mg-8Al (N <sub>2</sub> )	NA	NA	NA	NA
Mg-8Al-2Y (Ar)	41 ±5	93 ±1	9	85 E ±2
Mg-8Al-2Y (N <sub>2</sub> )	26 ±3	99 ±1	4	81E ±2

## CHAPTER 4 CONCLUSIONS

Calculations completed using the FACTSage software estimated that the decomposition points of magnesium hydroxide and magnesium carbonate present in the surface layer, 280 °C and 520 °C, respectively, are below possible common sintering temperatures. Thermodynamic calculations also indicate there are a number of metals that have an oxide more stable than MgO, and could be used to reduce MgO during sintering.

Experimentation using the differential scanning calorimeter gave an indication that the hypothesized decomposition reactions did indeed occur around the temperatures estimated by FACTSage in pure magnesium samples. Samples containing 1 wt% calcium showed additional reactions that should further disrupt the surface layer during sintering. Samples containing 2 wt% yttrium did not show any reaction, indicating it may hinder sintering.

X-ray photoelectron microscopy was utilized to identify the composition of the surface layer on green and sintered pure magnesium samples. The presence of oxides, carbonates and hydroxides was shown in green samples. Carbonates and hydroxides of magnesium were concentrated at the surface of the layer, followed by a majority of oxides, then pure magnesium. After sintering the samples contained only magnesium and magnesium oxide, indicating that the decomposition reactions of the hydroxide and carbonate had taken place.

Scanning electron microscopy and energy dispersive spectroscopy were used to determine the behaviour of calcium in a sintered sample. It was found that calcium diffuses throughout the magnesium matrix, with higher concentrations at the grain boundaries. Oxides are found mainly as discrete particles in the form of CaO, indicating that the MgO in the surface layer had been reduced allowing unimpeded sintering.

The focused ion beam system was utilized to prepare samples for TEM analysis, and also for imaging. FIB allows for stress free machining, which is critical for protection of the fragile surface layer. Also, microstructures shown on FIB prepared samples show a true, unaffected representation of the sample.

Transmission electron microscopy utilized FIB prepared samples of pure magnesium particles to measure the thickness of the surface layer. Samples were either tested as-received or exposed to atmosphere for 24 or 72 hours. The layer thickness was found to increase with increasing exposure time. EDS also showed the composition of the layer, which comprised of magnesium, carbon and oxygen, with carbon concentrated at the outer layer, oxygen at the inner layer and magnesium at the core of the particle. This coincides with the XPS results.

In terms of practical sintering of magnesium P/M parts, it was found that magnesium powder produced by atomization is superior to powder produced by grinding. The main advantage of the atomized powder is the much lower oxygen content. Compaction by cold isostatic pressing was found to produce better properties at

comparable pressures to uni-axially compacted samples. Increased sintering time and temperature also improved properties of the atomized CIP samples. Extended sintering times of 6 hours lead to further improvement.

Alloying additions of aluminum and zinc were found to increase density and hardness in magnesium P/M samples due to liquid phases and solid solution strengthening. Tin additions form a liquid phase that allows for improved density and hardness due to improved diffusion.

Calcium was shown to diffuse readily through the magnesium matrix and greatly improve density and hardness due to reduction of MgO and disruption of the surface layer found on magnesium particles. It was also found that yttrium forms a very stable surface layer, and reacted sparingly with the surrounding magnesium. Properties were improved with yttrium additions.

It was found that changing the sintering atmosphere from argon to nitrogen produced samples with improved properties. Yttrium additions, which were shown to be detrimental when sintered under argon showed a marked improvement under nitrogen. This is attributed to increased wetting of liquids on nitrides that form in the semi-reactive nitrogen atmosphere.

Cold and hot working of sintered magnesium P/M samples lead to large increases in density and especially hardness. Cold working of the samples collapses porosity and

breaks and remaining intact surface layer, and improved interparticle bonding is realized. This effect is increased with hot working, where increased temperatures lead to recrystallization and further bonding.

#### **4.1 Contribution to Original Thought**

The fundamental sintering studies of magnesium lead to an improved understanding of the main barriers to successful sintering, and resulted in a number of innovations for practical sintering. Thermodynamic calculations showed the possibility of compounds other than oxides in the surface layer of magnesium, and how their decomposition may affect the integrity of the layer. Possible alloying additions were also identified that could reduce the remaining magnesium oxide. Differential scanning calorimetry was utilized to identify decomposition reactions and metallothermic reduction.

The x-ray photoelectron spectroscope was utilized for the first known time to analyze the surface layer of powder metallurgy parts. This study confirmed the presence of carbonates and hydroxides in the surface layer, as well as their decomposition during sintering. A complimentary study utilized, for the first known time, the focused ion beam to isolate and image the surface layer of a magnesium powder particle. Further work with FIB prepared samples in the transmission electron microscope lead to measurements of the thickness of the layer and confirmed its composition.

FIB was also used to image a calcium containing magnesium sample. The stress-free sectioning only possible with the FIB lead to images of the true structure of the part, which shows a much more well sintered structure than was previously thought with examining mechanically polished samples.

The effect of calcium additions on magnesium sintering was shown using the scanning electron microscope and energy dispersive spectroscopy mapping showed the high mobility of calcium in magnesium and its ability to reduce MgO.

The effects of sintering in a semi-inert nitrogen atmosphere were tested for the first known time with magnesium P/M. It was theorized that nitrides formed are more readily wet than the oxides present when sintered in argon, and the flow of liquid phases is improved. This leads to improved density and hardness in nitrogen sintered samples, and allows yttrium, which has little effect in argon, to reduce MgO and further improve sinterability.

## **4.2 Recommendations for Future Work**

Magnesium powder metallurgy is still in its infancy, and the current work is a systematic study to identify the main barriers to sintering pure magnesium. The analysis techniques utilized with pure magnesium can be extended to P/M magnesium alloys to understand their effect on sintering mechanics.

Some practical sintering strategies based on the findings of the fundamental study were presented, but many avenues have many more possible solutions. Calcium and yttrium have been identified as alloying additions that reduce MgO as well as form beneficial liquid phases. Further work can center on finding the best amount of addition, compaction method and sintering variables. Other alloying additions that work in concert with Ca and Y for additional liquid formation, strengthening and corrosion resistance need to be identified.

## REFERENCES

1. Avedesian, M.M., Baker, H., Editors, "ASM specialty handbook, magnesium and magnesium alloys", ASM International, Materials Park, OH, 1999.
2. Kipouros, G.J., Sadoway, D.R., "The Chemistry and Electrochemistry of Magnesium Production", Advances in Molten Salt Chemistry, Vol. 6, Ed. Mamantov, G., Mamantov, C.B. and Braunstein, J., Elsevier, Amsterdam, 127-209, 1987.
3. German, R.M., "Powder Metallurgy and Particulate Materials Processing", Metal Powder Industries Federation, MPIF, Princeton, New Jersey, U.S.A, 2005.
4. NEDO, under the Synergy Ceramics Project of the ISTF program promoted by AIST, MITI, "Micro-scale Simulation of Solid State Sintering", Nagoya, Japan, 2002.
5. NEDO, under the Synergy Ceramics Project of the ISTF program promoted by AIST, MITI, "Micro-scale Simulation of Liquid Phase Sintering", Nagoya, Japan, 2002.
6. Schaffer, G.B., Hall, B.J, Bonner, S.J., Huo, S.H., Sercombe, T.B., "Affect of atmosphere and pore filling in the sintering of aluminum", Acta Materialia, Vol. 54, 131-138, 2006.
7. P. Burke, C. Petit, V. Vuaroqueaux, G.J. Kipouros, "The Effect of Processing Sintering Parameters and Post – sintering Operations in the Production of Magnesium Powder Metallurgy Parts", COM 2010, Aerospace Materials and Manufacturing: Advances in Materials, Processes and Repair Technologies, 225-234, 2010.
8. Munir, Z. A., "Surface oxides and sintering of metals", Powder Metallurgy, Div. Materials Science Engineering, Univ. California, Davis, CA, USA., 1981.
9. Estrin, Y., Gottstien, G., Shivindlerman, L.S., "Thermodynamic effects of the kinetics of vacancy-generating processes", Acta Metallurgica, Vol. 47, No. 13, 3541-3549, 1999.
10. Shallenberger, J.R.; Cole, D.A.; Novak, S.W.; Moore, R.L.; Edgell, M.J.; Smith, S.P.; Hitzman, C.J.; Kirchhoff, J.F.; Principe, E.; Biswas, S.; Bleiler, R.J.; Nieveen, W.; Jones, K.; , "Oxide thickness determination by XPS, AES, SIMS, RBS and TEM," Ion Implantation Technology Proceedings, 1998 International Conference on , vol.1, no., pp.79-82 vol.1, 1999.

11. H. Störmer, E. Ivers-Tiffée, C. Schnitter, D. Gerthsen, “Microstructure and dielectric properties of nanoscale oxide layers on sintered capacitor-grade niobium and V-doped niobium powder compacts”, *International Journal of Materials Research* 97, 794-801, 2006.
12. Brown, M., Gallagher, P., *Handbook of Thermal Analysis and Calorimetry*, Volume 5, 2008.
13. Friedrich, Horst E., Mordike, Barry L. “Magnesium Technology - Metallurgy, Design Data, Applications”, Springer - Verlag., 2006.
14. D.J. Loyd, “Particle Reinforced Aluminum and Magnesium Matrix Composites”, *International Materials Review*, 39, 1-23, 1994.
15. W. Xie, Y. Lui, D.S. Li, J. Zhang, Z.W. Zhang, J. Bi, “Influence of sintering routes to the mechanical properties of magnesium alloy and its composites produced by PM technique”, *J. of Alloys and Compounds*, 431, 2007, 162–166.
16. K. Kubota, M. Mabuchi, K. Higashi, “Review Processing and mechanical properties of fine-grained magnesium alloys”, *J. of Materials Science.*, Vol. 34, 1999, 2255-2262.
17. Y. Kawamura, A. Inoue, “Development of high strength magnesium alloys by rapid solidification”, *Materials Science Forum*, Vol. 419-422, 2003, 709-714.
18. C.J. Bettles, M.H. Moss, R. Lapovok, “A Mg-Al-Nd alloy produced via a powder metallurgical route”, *Materials Science and Engineering: A*, Volume 515, Issues 1-2, 25 July 2009, 26-31.
19. Y. Li, Y. Chen, H. Cui, B. Xiong, J. Zhang, “Microstructure and mechanical properties of spray-formed AZ91 magnesium alloy”, *Materials Characterization*, Volume 60, Issue 3, March 2009, 240-245.
20. H.T. Son, J.M. Hong, I.H. Oh, J.S. Lee, T.S. Kim, K. Maruyama, “Microstructure and mechanical properties of Mg-Zn-Y alloys fabricated by rapid solidification and spark plasma sintering processes”, *Solid state phenomena: B*, 2007, vol. 124-126 (2), 1517-1520.
21. J. Umeda, K. Kondoh, H. Imai, “Friction and wear behavior of sintered magnesium composite reinforced with CNT-Mg<sub>2</sub>Si/MgO”, *Materials Science and Engineering: A*, Volume 504, Issues 1-2, 25 March 2009, 157-162.
22. Wolff, M., Ebel, T., Dhams, M., “Sintering of Magnesium”, *Advanced Engineering Materials*, Vol. 12, No. 9, 829-836, 2010.

23. P. Burke, D. Fancelli, G. J. Kipouros, "Investigation of the Sintering Fundamentals of Magnesium Powders", COM 2007, Light Metals in Transport Applications, Ed. M.O. Pekguleryuz, 2007, 183-195.
24. P. Burke, D. Fancelli, V. Laverdiere, G. J. Kipouros, "Sintering Fundamentals of Magnesium Powders", Can. Metall. Q., 48, (2), 123-132 (2009).
25. J. Li, G.J. Kipouros, P. Burke and C. Bibby, "Investigation of surface film Formed on Fine Mg Particles", Microscopy & Microanalysis, VA, USA, July 26-30 (2009).
26. P. Burke, G.J. Kipouros, "Powder Metallurgy of Magnesium: Is it Feasible?", Ed. Sean R. Agnew, Magnesium Technology 2010, TMS 2010, Seattle, 2010, 115-120.
27. P. Burke, G.J. Kipouros, "Magnesium Powder Metallurgy AZ31 Alloy Using Commercially Available Powders", High Temperature Materials and Processes, 2010.
28. P. Burke, C. Petite, S. Yakoubi, G.J. Kipouros, "Thermal Effects of Calcium and Yttrium Additions on the Sintering of Magnesium Powder", Ed. Sean R. Agnew, Magnesium Technology 2011, TMS 2011, San Deigo, 2011.
29. Lumley, R. N., Sercombe, T. B., Schaffer, G. B. "Surface oxide and the role of magnesium during the sintering of aluminum", Metallurgical and Materials Transactions A, 30 2, 1999, 457-463.
30. Metal Powders Industries Federation, "Standard Test Methods for Metal Powders and Powder Metallurgy Products", 1999 Edition.
31. W.F. Caley, B. Paton, D.P. Bishop, G.J. Kipouros, "On Enhancing the Interfacial Chemistry of a Simulated AA2014-SiC<sub>p</sub> Composite Material", J. Materials Science, 38, 5, 2003, 1755-1765.
32. K. K. Kelly, Contribution to the data on theoretical metallurgy, No. 12, Bulletin 584, Bureau of Mines, Pg. 110-117, 1960.
33. V. Fournier, P. Marcus, I. Olefjord, "Oxidation of magnesium", Surface and Interface Analysis, 34, 2002, 494-497.
34. H.B. Yao, Y. Li, and A.T.S. Wee, "An XPS investigation of the oxidation/corrosion of melt-spun Mg", Applied Surface Science, 158, 2000, 112-119.

35. "Characterisation of the surface chemistry of magnetism exposed to the ambient atmosphere", Catalin Fotea, James Callaway, and Morgan R. Alexander, *Surface and Interface Analysis*, 38, 2006, 1363-1371.

## APPENDIX 1

### CHEMICAL COMPOSITION OF MATERIALS

Table A.1 shows the chemical composition of the base powders as supplied by Eckart Granules.

**Table A.1 - Chemical composition of base powders, as reported by the manufacturer.**

Element	Weight Percent			
	Ground Magnesium	Aluminum	Zinc	Tin
Mg	98.6			
Al		99.5		
Zn			99.8	
Sn				99.3
O	1.32	0.05-0.5	0.2 max	0.4 max
Other	0.08	0-0.45		0.3

Calcium and yttrium granules were provided by Acros Organics and have a purity of 99% and 99.5% respectively. Remaining impurities are mainly oxygen.

The atomized magnesium powder from Tangshan Weihao Magnesium Powder Co. had a composition, as supplied by the manufacturer, as shown in Table A.2.

**Table A.2 – Chemical composition of atomized pure magnesium powder.**

---

Magnesium	> 98 %
Iron	0.05 %
Aluminum	0.01 %
Silicon	0.03 %
Oxygen	0.08 %
Other	0.01 %

---

The wax lubricant used, stearic acid, is a saturated fatty acid that comes from many animal and vegetable fats and oils. It is a waxy solid, and its chemical formula is  $\text{CH}_3(\text{CH}_2)_{16}\text{COOH}$ . It has a softening temperature of  $45^\circ\text{C}$ , melting temperature of  $55^\circ\text{C}$  and a theoretical density of  $0.85 \text{ g/cm}^3$  [3].